DERIVING M DWARF ELEMENTAL ABUNDANCES

A SPECTROSCOPIC FRAMEWORK FOR DERIVING ELEMENTAL ABUNDANCES OF M DWARFS

By NICOLE GROMEK, B.Sc.

A Thesis Submitted to the School of Graduate Studies in Partial Fulfillment of the Requirements for the Degree Master of Science

McMaster University

MASTER OF SCIENCE (2024)

Hamilton, Ontario, Canada (Physics and Astronomy)

TITLE:	A Spectroscopic Framework for Deriving Elemental Abundances of M Dwarfs
AUTHOR:	Nicole Gromek B.Sc. (Physical and Chemical Sciences), University of Toronto Mississauga, Mississauga, Canada
SUPERVISOR:	Dr. Ryan Cloutier
NUMBER OF PAGES:	xvi, 143

Lay Abstract

Understanding what planets are made of helps us learn how they form. Since planets and their stars are created from the same materials, we can study a star's composition to learn more about the planets that orbit it. Measuring the abundances of planet-forming elements like magnesium, silicon, and iron is routinely performed for Sun-like stars, but the task proves to be much more difficult for smaller, cooler stars like M dwarfs. M dwarfs are very common and host most of the super-Earths within the Milky Way that could potentially support life, so studying them is crucial. My Master's thesis focuses on developing a method to accurately measure the elemental abundances in M dwarfs using high-resolution spectra taken at infrared wavelengths where M dwarfs emit most of their light. My work is helping to improve our understanding of the composition and formation pathways of exoplanets around M dwarfs.

Abstract

Measuring accurate stellar abundances of planet-forming elements is critical to our understanding of exoplanet compositions and their formation processes. While these values can be reliably derived from optical spectra for FGK-type stars, the recovery of accurate abundances for M dwarfs is complicated due to persistent discrepancies between models and observed spectra, such as blended absorption features and broad molecular bands that obscure the continuum. These lingering uncertainties in M dwarf chemical compositions inhibit our ability to accurately model the interiors and atmospheres of exoplanets around M dwarfs. To address this issue, we have built a custom framework to extract elemental abundances from the spectra of cool stars via the spectral synthesis method. We showcase our methodology as well as the derived elemental abundances for a pair of cool stars. SPIRou, with its high spectral resolution and broad near-IR wavelength range, is the ideal instrument to help mitigate the difficulties present in the recovery of M dwarf elemental abundances. By combining the capabilities of SPIRou with our framework, we are well equipped to ensure the accuracy of derived elemental abundances in M dwarfs. Our results will ultimately be applied to planet-hosting M dwarfs in order to place strong constraints on the planets' refractory and volatile abundances, both of which are important diagnostics of planetary formation histories and interior compositions.

Take pride in how far you've come

Have faith in how far you'll go

- Michael Josephson

Acknowledgements

First and foremost, I'd like to thank Dr. Ryan Cloutier, one of the best supervisors and mentors I could ever ask for. These past two years have been a learning experience for us both. Your patience, support, and guidance have been essential in helping me reach this milestone. Thank you for believing in me, and even though I might stress you out from time to time, I hope I make you proud. I would also like to thank the members of my committee, Dr. Doug Welch and Dr. Ralph Pudritz, whose insight and constructive feedback were invaluable in improving this thesis.

To Erik, Daniel, Alex, Ceara, Edan: your friendship means the world to me. Thank you for joining me on this journey, for all the boba trips, and for keeping me sane by sending me memes. To Padraic, my safe haven in the chaotic world of academia, thank you for the joy and peace of mind you bring to my life. To my research group: Drew, Bennett, Raven, and Ares, thank you for fueling my Pokemon addiction, for helping me derail our group meetings when I need a break, and for lending a helping hand when I need one.

To all the friends I've had the pleasure of making at McMaster, thank you for being such a supportive and fun community. Whether it be squash, parties, softball, D&D, or just saying hi in the lunchroom, you give me the strength to keep going. To those of you who have helped me on my path, I'm afraid I can't recount each and every one of your names here or else this thesis would be 10 times longer. Just know that you have my eternal gratitude.

To my parents, your steadfast love and support have been the foundation of everything I've accomplished. I would not be where I am today without you. Finally, to the little girl who picked up a book about Mars and dreamed of studying the stars & their planets ever since then, you made it. It took years of hard work, a lot of sleepless nights, and a never-ending curiosity, but you finally made it.

Table of Contents

List of Figures

List of Tables

Notation, Definitions, and Abbreviations

Notation

T_{eff}	Effective Temperature (K)
$\log g$	Surface Gravity (dex)
[M/H]	Metallicity (dex)
[X/H]	Elemental Abundance (dex)
[α/H]	Alpha Abundance (dex)
A(Q)	Absolute Abundance
$v \sin i$	Rotational Velocity (km/s)
R	Spectral Resolution
σ	Sigma
χ^2	Chi-square
$R_\oplus$	Earth Radius
$R_\odot$	Solar Radius

R_*	Stellar Radius
$M\oplus$	Earth Mass
$M\odot$	Solar Mass
M_*	Stellar Mass

Definitions

FGK star Sun-like stars with temperatures between 4000 K and 7500 K and masses ranging from 0.6 $\odot$ to 1.3$M\odot$.

M dwarf Stars that are cooler, smaller, and redder than FGK stars, with temperatures between 2500 K and 3900 K, and masses between 0.08 $M\odot$ and 0.6$M\odot$.

Exoplanet Planets that orbit stars other than the Sun.

Hot Jupiter Massive Jupiter-sized planets that orbit very closely to their host stars, resulting in high surface temperatures. These will typically have a radius above 6 $R\oplus$ and an orbital period of less than 10 days.

Super-Earth Planets with radii between 1.25 - 1.7 $R\oplus$ that are mostly composed of rock with iron cores, and oftentimes a thin or missing atmosphere.

Sub-Neptune Low-density planets with radii between 2 - 3 $R\oplus$ with cores consisting of ice and rocky materials underneath thick, volatile-rich atmospheres.

Habitable Zone The circumstellar orbital region where temperatures allow exoplanets to be able to sustain liquid water on their surfaces.

Refractories Chemical species with high sublimation temperatures, allowing them to resist phase changes at all but the hottest temperatures. These include iron and silicates.

Volatiles Chemical species with low sublimation temperatures, such as carbon, oxygen, or water.

YJHK Band The range of wavelengths between 0.97 and 2.41 µm in the near-infrared regime.

Abbreviations

APERO A PipelinE to Reduce Observations

APOGEE Apache Point Observatory Galactic Evolution Experiment

CCD Charge Coupled Device

CCF Cross Correlation Function

CFHT Canada France Hawaii Telescope

CMF Core Mass Fraction

EW Equivalent Width

GJ Gliese-Jahreiss Catalogue

HST Hubble Space Telescope

HZ Habitable Zone

IR InfraRed

JWST James Webb Space Telescope

LTE Local Thermodynamic Equilibrium

MARCS Model Atmospheres with a Radiative and Convective Scheme

MCMC Markov Chain Monte Carlo

NaN Not a Number

NASA National Aeronautics and Space Administration

nIR Near InfraRed

NLTE Non-Local Thermodynamic Equilibrium

RV Radial Velocity

SME Spectroscopy Made Easy

SNR Signal to Noise Ratio

SPIRou SPectropolarimètre InfraRouge

TESS Transiting Exoplanet Survey Satellite

VALD Vienna Atomic Line Database

XUV X-ray and UltraViolet radiation

Chapter 1

Introduction

A common saying in exoplanetary astronomy is "know thy star, know thy planet". Because planets and their host stars are formed from the same surrounding nebula, we can speculate that their primordial compositions will be intimately connected. This approach allows us to use the present-day stellar composition as a proxy for the planetary interiors, assuming that it has not been altered by stellar evolutionary effects or complex disk chemistry (Adibekyan et al., 2024; Sharma et al., 2024). Not only that, the properties of the host star will have a direct effect on the types of planets that form, as well as their surface conditions and habitability (Hinkel et al., 2024).

Exoplanet discovery missions like Kepler (Borucki et al., 2010) and the Transiting Exoplanet Survey Satellite (TESS; Ricker et al. 2015) have allowed astronomers to confirm the existence of over 5,700 exoplanets so far (NASA Exoplanet Archive). As the field moves forward, there will be a greater focus on detailed studies of individual planets and the role their host stars play in their development and habitability. There are several ways we can take advantage of this planet-star connection to inform our understanding of exoplanets, which we will explore in the following sections.

1.1 Breaking Interior Degeneracies

To understand the formation processes and accretion history of exoplanets, measurements of their interior composition are necessary. The interior composition of a planet influences whether it has certain characteristics needed to sustain life, such as a magnetic field or plate tectonics (Foley and Driscoll, 2016). For instance, the Earth's molten iron core generates the magnetic field which helps to shield us from the solar wind. The interior compositions of exoplanets are not directly observable and so, we must rely on a small set of physical parameters to constrain their bulk compositions. By using planetary mass and radius as two accessible observables, theoretical mass-radius curves can give us information about the interior structures of exoplanets through bulk density calculations (Brügger et al., 2018; Noack and Lasbleis, 2020; Seager et al., 2007; Sotin et al., 2007). However, measuring mass and radius alone can lead to large degeneracies in interior compositions of hydrogen, water, and metal, because different compositions can reproduce the same mass and radius (Dorn et al., 2019; Kossakowski et al., 2021; Rogers and Seager, 2010; Unterborn et al., 2023). Such a case was observed in the early days of exoplanet discovery with GJ 436 b (Butler et al., 2004). This Neptune-sized exoplanet was originally conjectured to have the same composition as Neptune due to their similarities in both mass and radius (Gillon et al., 2007; Torres et al., 2008). However, it was shown not long afterward that it could instead have a large iron core with an H/He envelope rather than being an icy ocean planet (Adams et al., 2008). A recent study by Schlichting and Young (2022) also showed that the mass-radius relation for super-Earths and sub-Neptunes can be significantly impacted by the presence of other light elements within iron-rich cores.

The example of GJ 436 b perfectly illustrates the necessity of using additional observables to constrain these models. For example, recent years have seen astronomers using the newly launched JWST to study the starlight passing through a planet's atmosphere in order to characterize its composition (Rustamkulov et al., 2023). Although emission spectroscopy can provide valuable insight into the presence and composition of a planet's atmosphere, one still needs the context of the star to provide a holistic picture of the planet's formation history and evolution. Furthermore, it is impossible to directly observe the interior structure of exoplanets. Even in the rare case of having a fully characterized atmosphere, degeneracies will remain in the interior composition of rocky planets. As such, it is necessary to use the more accessible composition from the stellar host to inform current interior structure models. Thus, inferring planet-forming elemental abundances from the host star is critical for breaking these degeneracies (Bond et al., 2010; Dorn et al., 2015; Hinkel et al., 2024; Melo et al., 2024). This technique has been used in previous studies where the measured relative stellar abundances were used to constrain bulk compositions of super-Earths and sub-Neptunes (Brugger et al., 2017; Dorn et al., 2017; Putirka and Rarick, 2019).

1.2 How Elemental Ratios can Inform Planet Formation

While the planet-star relationship is often simply assumed in the literature (Dorn et al., 2015), prior work has been done to cement this relationship. To summarise findings, while stellar elemental ratios may be modified by time-dependent processes like diffusion and gravitational settling in stellar interiors, they remain largely unchanged. In the Solar System, the refractory ratios of Fe, Mg and Si in the terrestrial exoplanets — save for Mercury — and CI-chondritic meteorites will correlate to the compositions derived from the Sun with some caveats (Lodders, 2019). This picture allows us to understand elemental abundances not just as current observations, but as probes of the planet's past evolution. The question to be asked now is: what do trends of specific elemental ratios in the star tell us about planet formation pathways and disk chemistry?

Compositions of both exoplanet interiors and atmospheres can provide key insight into a planet's formation pathway and migration history. These allow astronomers to constrain formation mechanisms through examination of the composition as a tracer of both accretion history and the dominant chemical processes. Determined by primordial composition and altered by formation processes, it is detecting the presence — or lack thereof — and ratios of key chemical species that can help constrain their formation, based on the theoretical elemental compositions from differing models. For instance, we know that planets formed in the same disk can be expected to have similar budgets of refractory elements as each other and the star (Thiabaud et al., 2015), but can vary greatly in volatile elements like C, N and O, whose sublimation temperatures are highly variable throughout the disk (Öberg and Bergin, 2016). The reason for this is that refractory elements require a much higher temperature to evaporate, meaning that their condensation fronts are much closer to the stars compared to volatiles (Helled et al., 2022; Wang et al., 2019). A few ratios play prominent roles in helping us answer this question and will be expanded upon in their own sections: the carbon-to-oxygen (C/O) ratio on behalf of the volatile elements to better understand the structure, atmospheres and migration histories, magnesium-to-silicon (Mg/Si) and magnesium-to-iron (Mg/Fe) on behalf of the refractory elements for the mineralogy of exoplanets, as well as the role of alpha abundance enhancement.

1.2.1 Volatile Abundance Ratios

By comparing the planetary and stellar volatile element ratios, particularly that of carbon-to-oxygen, we can gain crucial information about where planets originally formed and migrated within the protoplanetary disk (Turrini et al., 2021). This is because major molecules (i.e. H_2O or CO) will freeze out at different radii in the disk, known as "snow lines" (Öberg et al., 2011). During the later stages of formation, models show that a wide range of C/O ratios and metallicities can exist in planet atmospheres as a result of their migration and accretion across differing snow lines (Madhusudhan, 2019). Giant planets that form via core accretion and migrate through the disk will accrete oxygen-rich planetesimals, resulting in an envelope with a super-stellar metallicity and a sub-stellar C/O ratio (Madhusudhan et al., 2016; Öberg et al., 2011). Giant planets that form beyond the CO snow line that migrate inwards after the disk has dissipated will instead have carbon-rich atmospheres with sub-stellar metallicities and high C/O ratios (Öberg et al., 2011). Though nitrogen is comparatively more challenging to observe in disks and exoplanetary atmospheres, C/N ratios have also been shown to provide insight into planet formation processes (Cridland et al., 2017; Ohno and Fortney, 2023b). The radial distance at which the planet forms, in addition to its migration history, will set the level of enrichment of volatile elements in its atmosphere (Madhusudhan et al., 2014; Schneider and Bitsch, 2021). Atmospheric elemental ratios can be measured for sub-Neptune and hot Jupiters using transit spectroscopy techniques. The atmospheres of a few sub-Neptunes have recently been studied with JWST via transmission spectroscopy, revealing rich atmospheric chemistry including detections of H_2O, CH_4, CO_2, and even tentative biosignatures (Benneke et al., 2024; Madhusudhan et al., 2023; Mikal-Evans et al., 2023). While such observations provide information about planetary accretion history, they are only meaningful when placed in the larger context of the star.

1.2.2 Refractory Abundance Ratios

Refractory abundance ratios play a crucial role in studying planet formation (Chachan et al., 2023; Smith et al., 2024). Rocky planets are often assumed to be differentiated into two layers: an iron-rich core and a rocky silicate mantle. This means that abundance ratios of refractory elements like Mg, Si, and Fe can inform our constraints for interior modelling, as these elements will often dictate the core-to-mantle ratio (Delgado Mena et al., 2010; Santos et al., 2017a; Thiabaud et al., 2015). Most importantly, because they can only be evaporated at high temperatures, they are not strongly impacted by processes in the disk. As shown by the work in Thiabaud et al. (2015), this means that the refractory ratios in planets are then identical to those in the host stars. Specifically, Thiabaud et al. (2015) modelled the Fe/Si, Mg/Si, and C/O ratios in the protoplanetary disk throughout the formation of rocky and icy planets and found that it was specifically the Fe/Si and Mg/Si ratios that matched between star and planet. As an extension of this idea, because magnesium is less volatile than silicon, it is one of the best rock-building elements to compare with primordial compositions (Yakovlev et al., 2018). To help compare planetary and stellar compositions, we use the concept of a core mass fraction (CMF). Simply put, it is the proportion of a planet's total mass that is attributed to the core (Plotnykov and Valencia, 2020). Because planetary cores are often assumed to be predominantly iron, this concept is often tied together with that of an iron mass fraction, although the two are distinct because some iron can persist within the silicate mantle (Plotnykov and Valencia, 2020). For the star, one may extrapolate the equivalent of a planetary CMF based on the measured stellar abundances. The core in this case is not the stellar core; rather, it is the fraction of iron mass to the total mass of planetary-building elements (Brinkman et al., 2024b). This will enable a better comparison between planetary and stellar compositions, which represent the current and primordial compositions of the system.

There have been several attempts to test the relationship of stars to planets observationally on a broader scale using confirmed exoplanetary systems. A key study here is Plotnykov and Valencia (2020) which found a broader distribution of Fe/Si and Fe/Mg ratios in rocky exoplanets than stars on a population level. Adibekyan et al. (2021), also aiming to find a compositional link between the two using the iron mass fraction of both star and planet, analyzed 21 rocky exoplanets orbiting FGK stars using a stoichiometric model from Santos et al. (2017b). As shown in Figure 1.1, they found a correlation with a corresponding ratio greater than 4:1, meaning the iron mass fraction within planets was much higher - likely indicating further processes occurring within the disk. Schulze et al. (2021) investigated this using data from 11 systems orbiting FGK stars, and they found that all but one planet had abundance ratios that agreed to their host star within 1σ. Brinkman et al. (2024b) likewise found similar abundance ratios in 6 planets to their Sun-like host stars by using high-precision RVs and comparing the ratios of iron to rock-building species between the planet and star. While these studies restricted their samples to planets with small errors on their mass and radii, it is important to note that these measurements still have large uncertainties that can lead to discrepancies. Nevertheless, the compositional link between star and planet has repeatedly been shown to exist.

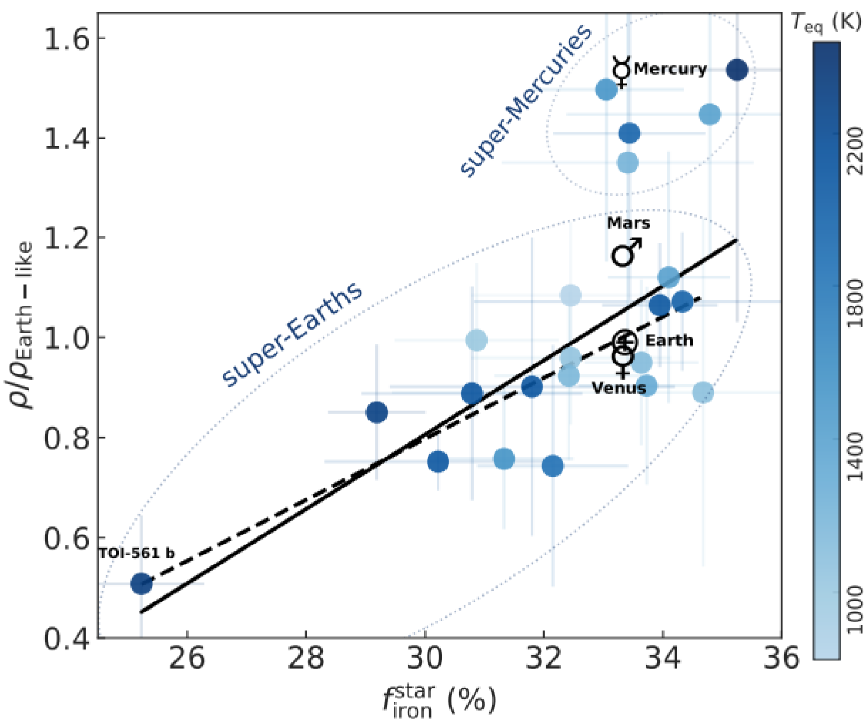

Figure 1.1: Figure from Adibekyan et al. (2021), where densities of rocky planets are shown as a function of iron mass fraction, normalised to that of an Earth-like composition. The iron mass fraction is based on the host star's elemental abundances. Solar System rocky planets are marked with black symbols, all using the Sun's iron fraction. The solid black line shows the correlation for the full sample, while the dashed line excludes five potential super-Mercuries.

From a theoretical perspective, Bond et al. (2010) simulated the formation and dynamics of terrestrial planets by combining circumstellar disk models and chemical equilibrium calculations, whilst carefully considering the chemical composition of the planets made. They found that their bulk elemental abundances matched previous studies of disk chemistry and that the refractory abundances in the system do not significantly change. However, it should be noted that Elser et al. (2012) also dynamically simulated planetesimal growth using different chemical disk models in an effort to reproduce both the bulk compositions of the inner solar system and the results of Bond et al. (2010). They instead found notable discrepancies, citing the model and dependence on assumed temperature along the disk as potential factors. In the broader context of core mass fractions and how they can inform planet formation pathways, one might consider three broad scenarios. The first is where the two CMF measures are consistent with each other, which is expected in the absence of any major evolutionary processes that would otherwise modify the planet's CMF. If the CMF of the planet is found to be higher than the stellar value, this may indicate a history of planetary collisions, where planetary embryos are preferentially stripped of their outer mantles, leaving behind iron-rich planets known as super-Mercuries (Mah and Bitsch, 2023; Marcus et al., 2009). These are named as such because Mercury is heavily enriched in iron, thought to be the result of giant impacts dominating the overall composition (Benz et al., 2007). Other planetary formation processes that could cause a higher-than-expected planetary CMF are mantle evaporation (Santerne et al., 2018) or tidal interactions (Price and Rogers, 2020). If we find such a case where the planetary CMF is lower than the stellar CMF, then this may be evidence for the existence of water sequestered beneath the surface, inflating the radius beyond what is expected of a purely rocky world (Luo et al., 2024). In summary, planetary formation processes such as giant impacts or water sequestration may significantly change the composition of terrestrial exoplanets, meaning that comparing primordial and current values can provide crucial context for the evolutionary history of the planetary system.

1.2.3 Alpha Elements

Alpha elements are the elements created by the alpha process in stellar nucleosynthesis — O, Ne, Mg, Si, S, Ar, Ca, and Ti. It was first observed by Aller and Greenstein (1960) and Wallerstein et al. (1963) that certain elements — Mg, Si, Ca, and Ti — were enhanced in observations of metal-poor stars. Fused in the cores of massive stars, these alpha elements are often released with Type II or Ib supernovae that then enrich the surrounding interstellar medium from which new stars and planetary systems are born (Tinsley, 1979). An overabundance of alpha elements in planetary hosts has been previously demonstrated by Haywood (2008), Adibekyan et al. (2012), and Sharma et al. (2024). While this may mean that they play a role in formation processes, more research needs to be done in this area.

1.3 Inferring Population Trends

While it is difficult to do studies on individual elemental abundances, by looking at previous studies done at the population level comparing the metallicity to observed exoplanet demographics, it is clear that the chemistry of the star impacts the types of planets that form around them (Bitsch and Battistini, 2020; Dorn et al., 2019; Madhusudhan et al., 2014; Mah and Bitsch, 2023). Metal-rich and more massive stars are more likely to host giant planets (Fischer and Valenti, 2005; Gonzalez, 1997; Johnson et al., 2010; Sozzetti et al., 2009). This is known as the giant planet-metallicity correlation (Johnson et al., 2010) and it is easily explained by the core accretion model of planet formation, wherein the availability of metals facilitated the rapid accumulation of massive solid cores that can trigger runaway gas accretion with the lifetime of the gaseous protoplanetary disk (Hubickyj et al., 2005; Ida and Lin, 2004; Pollack et al., 1996). The stellar metallicity determines the threshold for the formation of the planetary core mass needed to form giant planets. A more massive star will have a more massive protoplanetary disk (Mordasini et al., 2012; Tychoniec et al., 2018) and a more metal-rich protoplanetary disk will have more condensable solids (Alibert et al., 2011; Mulders, 2018). There is also theoretical evidence to suggest that planets around more massive stars accrete H/He atmospheres more efficiently (Lozovsky et al., 2021). Giant planets, especially Jupiter-mass planets, are much rarer around low-mass M dwarfs (Pass et al., 2023). This can again be explained in the core accretion model, as these smaller stars have less massive disks and longer dynamical timescales (Burn et al., 2021; Laughlin et al., 2004). The relative lack of gas and dust as well as the low surface density of an M dwarf's protoplanetary disk means the massive cores do not reach the necessary mass for runaway gas accretion before the disk dissipates (Cañas et al., 2022; Ida and Lin, 2004; Kennedy and Kenyon, 2008; Pollack et al., 1996). Despite the fact that gas giants rarely form around M dwarfs, a handful of hot Jupiters have been found to date, thanks to TESS (Cañas et al., 2022; Kanodia et al., 2023). While this is a small sample size, nearly all of these M dwarfs are early type and metal-rich (Gan et al., 2023; Kanodia et al., 2023), seemingly continuing the correlation of high metallicity and giant planet occurrence for lower mass stars.

Early observations of the field originally indicated that this planet-metallicity trend would continue to lower-mass planets, hinting that metal-rich stars would be favourable hosts (Bonfils et al., 2005; Rojas-Ayala et al., 2010; Schlaufman and Laughlin, 2010). However, once you get to a smaller regime of planet size (i.e. between Earth- and Neptune-sized planets), they no longer seem to preferentially orbit about metal-rich stars (Mulders, 2018). Multiple studies have shown that planet hosts have a wide range of metallicities and that there seems to be no preference in metallicity between planet hosts and non-planet hosts, but there is some conflicting information (Buchhave et al., 2012; Ghezzi et al., 2010; Mayor et al., 2011; Santos et al., 2011). Two separate studies in recent years have compared the iron mass fractions of planets using mass and radius and of host stars using refractory elemental abundance ratios. Liu and Ni (2023) found that the iron mass fraction for rocky planets is related to the relative abundance ratios of Fe, Mg, and Si in the host star and that iron content in those rocky planets is strongly correlated with host star metallicity. Brinkman et al. (2024a) likewise found fewer planets around metal-poor host stars and that there were very few iron-rich high density planets around metal-poor host stars in their sample. Attempting to use abundances of other elements as indicators of planet hosts has also brought up conflicting reports. Maldonado et al. (2020) did not find any correlation, but Sharma et al. (2024) noted enhanced abundances of Mg and Si in planet hosts relative to their comparison sample. In a similar vein, Melo et al. (2024) saw higher C/O ratios in their sample of exoplanet-hosting M dwarfs against M dwarfs with no planets.

In place of scaling with host star composition, smaller planets will instead occur more frequently around lower mass stars (Mulders, 2018). In fact, M dwarfs are the

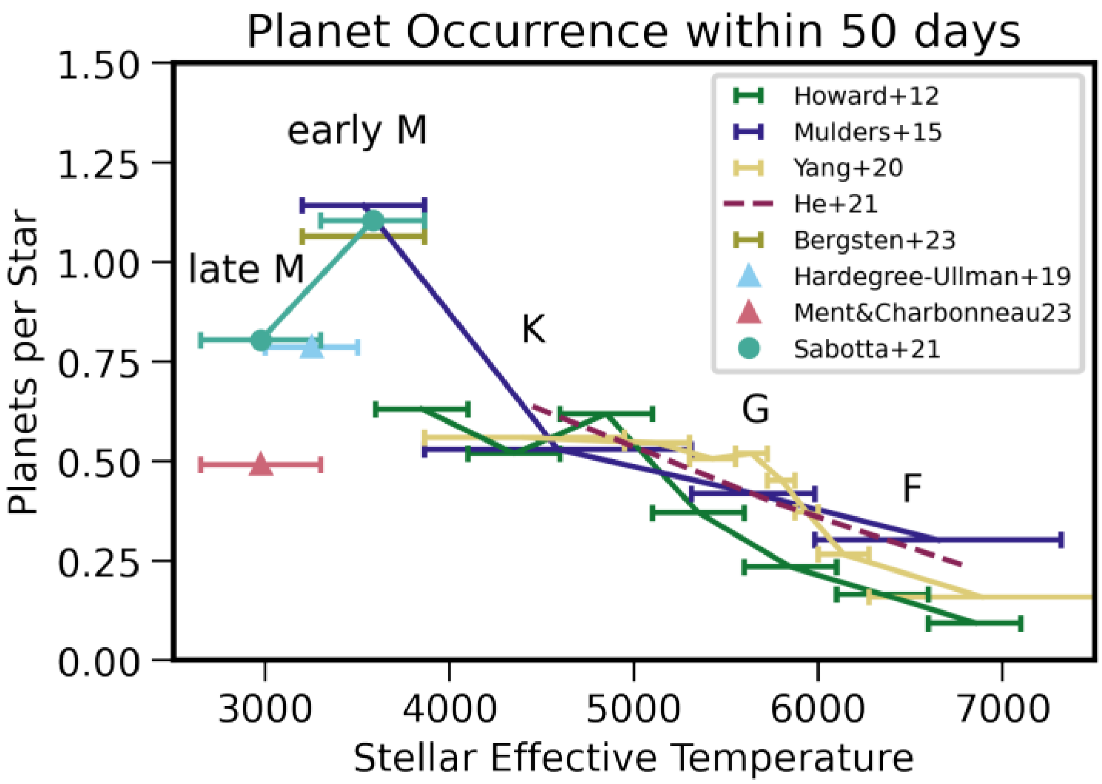

Figure 1.2: An overview of planet occurrence rates in the literature as a function of stellar effective temperature in Kelvin for planets between 1 - 4 $R_\oplus$ and P < 50 days, as shown in Mulders (2018).

most common hosts of super-Earths, which are potentially habitable planets similar to our own that may offer insight into the origins of life (Dressing and Charbonneau, 2013; Gaidos et al., 2016; Kopparapu et al., 2013). M dwarfs host a higher number of rocky planets than Sun-like stars do (Dressing and Charbonneau, 2015; Mulders et al., 2015). Mulders et al. (2015) used Kepler data and found that M dwarfs have up to 3.5 times more small planets (1.0 - 2.8 $R_\oplus$) than FGK stars but two times fewer planets larger than 2.8 $R_\oplus$. Dressing and Charbonneau (2015) performed an in-depth search for transiting planets using four years of Kepler data and estimated the occurrence rate of small planets with radii of 1 - 4 $R_\oplus$ and orbital periods below 200 days to be 2.5 $\pm$ 0.2 planets per M dwarf. These results were repeated and confirmed in studies by Hardegree-Ullman et al. (2019) and Hsu et al. (2020). It is important to keep in mind that the Kepler mission focused on Sun-like stars and so, their sample of M dwarf targets is an order of magnitude lower than FGK stars. This is also why the sample in Dressing and Charbonneau (2015) focused on early-to-mid M dwarfs with a median stellar radius of 0.47 $R_\odot$. What happens when we look to later type stars? Using more advanced instruments such as TESS, MAROON-X, SPIRou, and CARMENES, astronomers can observe fainter, later-type M dwarfs and any potential orbiting planets. Using data from TESS, Ment and Charbonneau (2023) found that sub-Neptunes (1.8 - 3 $R_\oplus$) are much less abundant around mid-to-late M dwarfs compared to earlier-type stars, while the occurrence rate of terrestrial planets is comparable across all M spectral types (Ment and Charbonneau, 2023). Moreover, rocky planets are much more common around mid-to-late M dwarfs than sub-Neptunes, outnumbering them 14 to 1 (Ment and Charbonneau, 2023).

It is clear that the planet occurrence rates change with the mass of the host star. Even within the M dwarf luminosity class between 0.08 - 0.6 $M_\odot$, the number of super-Earths and sub-Neptunes per star varies considerably. One of our primary goals is to test theories of planet formation, comparing theoretical frameworks to their observational counterparts. Do rocky planets preferentially form around M dwarfs or were there processes throughout the evolution of the system that did this? If so, which ones? It could be that a portion of these rocky planets were originally sub-Neptunes that were stripped of their atmospheres through processes such as XUV-driven photo-evaporation (Mordasini, 2020; Owen and Wu, 2013, 2017) or core-powered mass loss

(Ginzburg et al., 2018; Gupta and Schlichting, 2019, 2021). This is still very much an active field of research. If we wish to study super-Earths as habitable rocky worlds and learn about the formation of planets like Earth, characterizing M dwarfs is of the utmost importance. This includes developing a detailed understanding of the planet's interior composition and how that connects to the host M dwarf's composition.

1.4 M Dwarf Properties

M dwarfs, or red dwarfs, are the smallest and coolest type of star on the main sequence, typically having effective temperatures between 2500 K and 3900 K. Their masses range from 0.08 to 0.6 $M_{\odot}$ (Benedict et al., 2016). They are also the most common type of star, making up approximately 70 - 80% of the stellar population in the Milky Way and the local Universe (Henry et al., 2006; Reylé et al., 2021). As such, they represent one of the most common outcomes of the star formation process and understanding their chemistry is crucial to our understanding of stellar populations. Their lifespans are exceptionally long, due to their mostly convective interiors and low internal temperatures (Baraffe et al., 1998). This means that late-type M dwarfs can have main-sequence lifetimes of up to 10^{13} years – greater than the age of the universe itself (Laughlin et al., 1997). Because of both this and their ubiquity throughout the galaxy, they make for powerful tracers for the dynamical and chemical evolution of galaxies (Bochanski et al., 2010; Lépine and Gaidos, 2011; Lépine et al., 2013).

1.4.1 M Dwarfs as Tracers of Galactic Disk Chemistry

As previously stated, a key motivation to accurately study M dwarf chemistry is their use in galactic archaeology as chemical tracers of galactic evolution (Bochanski et al., 2007; Gizis et al., 2002; Reid et al., 1995, 1997; West et al., 2006). Stars from different galactic populations differ in their chemical composition and kinematics. One prominent example of this are the two components of the galactic disk: the thick disk and the thin disk. The thick disk formed first, forming an older, metal-poor population. To support this idea, the older stars originating in the thick-disk population will have lower metallicities and higher values of alpha-element abundances (Ness et al., 2019). Stars located along the Galactic plane will then form from the more metal-rich gas located there, allowing for more rapid star formation to occur. This causes the stellar population in the thin disk to be metal-rich and depleted in alpha elements. As such, one can easily use the chemistry of low-mass dwarfs to trace the spatial and kinematic properties of these thick and thin disks in both the Milky Way and other external galaxies (Bochanski et al., 2007).

1.4.2 M Dwarf Opportunity

M dwarfs are also useful in the context of better understanding exoplanets. Because M dwarfs have lower luminosities than Sun-like stars, the locations of their habitable zones are much closer to the star (see Figure 1.3). A habitable zone (HZ) in exoplanetary science is defined as the distance from the host star where the surface temperature allows for liquid water to be stable on the planet's surface. Because the HZ is closer to M dwarfs than it is to Sun-like stars, it becomes easier to detect planets in the HZ through their shorter orbital periods, increased likelihood and frequency of transits along the line of sight from Earth (Gaidos et al., 2007; Tarter et al., 2007). Approximately a third of these rocky M dwarf planets are located within the habitable zone (Shields et al., 2016). One of the most well-known examples is the TRAPPIST-1 system, a system with seven rocky planets orbiting an ultra-cool dwarf star. Three of these planets (TRAPPIST-1 e, f, and g) orbit within the HZ (Gillon et al., 2017). While certain barriers to habitability in M dwarf systems do exist — such as increased stellar activity, tidal locking of planets, and unlikely formation of asteroid belts — conditions still make them favourable candidates for observation (Childs et al., 2022).

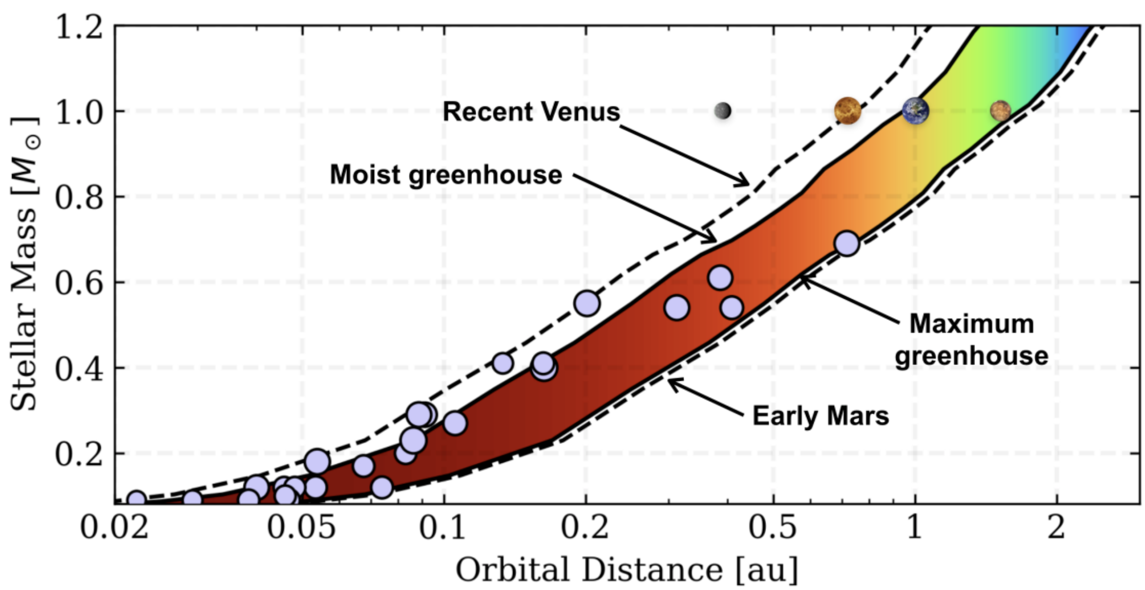

Figure 1.3: The estimated orbital distance limits of the habitable zone as a function of stellar mass using the models of Kopparapu et al. (2013), taken from Cloutier (2024).

To characterise planets and model their bulk densities, we need to obtain accurate measurements for masses and radii. However, doing so at the population level stretches our observing capabilities to the limit. It is for this reason that M dwarfs in particular have garnered attention for use in exoplanet studies. Astronomers determine planetary mass via the radial-velocity (RV) technique, measuring the gravitational influence on the star by the orbiting planet. They determine planetary radius via the transit method, where they measure the dip in the light curve of a star caused by a planet passing in front in our line of sight (Hinkel et al., 2024). In both these cases, a smaller star will cause a deeper transit in the lightcurve and a stronger radial-velocity signal, thus enabling access to small terrestrial planets that are often observationally out of reach around FGK dwarfs (Cadieux et al., 2022). This ability of M dwarfs to enable the discovery and characterization of planets and their parameters is known as the "M Dwarf Opportunity" (Charbonneau and Deming, 2007; Dressing and Charbonneau, 2015; Gaidos et al., 2007; Shields et al., 2016).

1.5 Spectroscopic Methods

How do we get information about abundances from stars? By using their spectra. We assume stars as blackbodies, which will emit radiation in a continuous spectrum whose peak wavelength depends solely on the star's temperature. This relationship is often shown using Wien's displacement law:

$$\lambda = \frac{b}{T} \tag{1.5.1}$$

where λ is the peak wavelength in metres, T is the absolute temperature in Kelvin and b is the constant of proportionality. These spectra measure the intensity of this light across the electromagnetic spectrum as a function of wavelength. However, we observe that these spectra are not perfectly smooth. They have dark bands at specific wavelengths, called spectral absorption lines. These lines are caused by radiation passing through the stellar atmosphere, getting absorbed by an atom or molecule and causing an electron to make the transition from a lower energy orbital to a higher orbital. Molecular absorption will also occur, caused by incident photons exciting rotational and vibrational modes of molecules. These absorption features are unique to each chemical species, acting as a chemical fingerprint to help us trace their presence. These lines contain a treasure trove of information about stellar composition, temperature, and motion via the Doppler shift.

Astronomers measure these spectra using specialised instruments called spectrographs. The working principle is that light is collected by a telescope and fed to the spectrograph, which disperses it into its constituent wavelengths using a dispersive element such as a prism or diffraction grating and records the incident spectrum on a detector, typically a charge coupled device (CCD). Several types of spectrographs are optimised for different purposes. For example, long-slit spectrographs are used for larger objects such as galaxies, and multiple-fibre optic spectrographs allow for several sources to be observed at once for large-scale surveys. When one wants to do high-resolution detailed spectral analysis on single sources, a popular choice in modern astronomy is an echelle spectrograph. The echelle spectrograph uses a high-density diffraction grating to disperse light into multiple echelle orders that then overlap, necessitating further separation with a cross-disperser. The benefit is a high spectral resolution over a wide wavelength range. An example of one such echelle spectrum is shown in Figure 1.4.

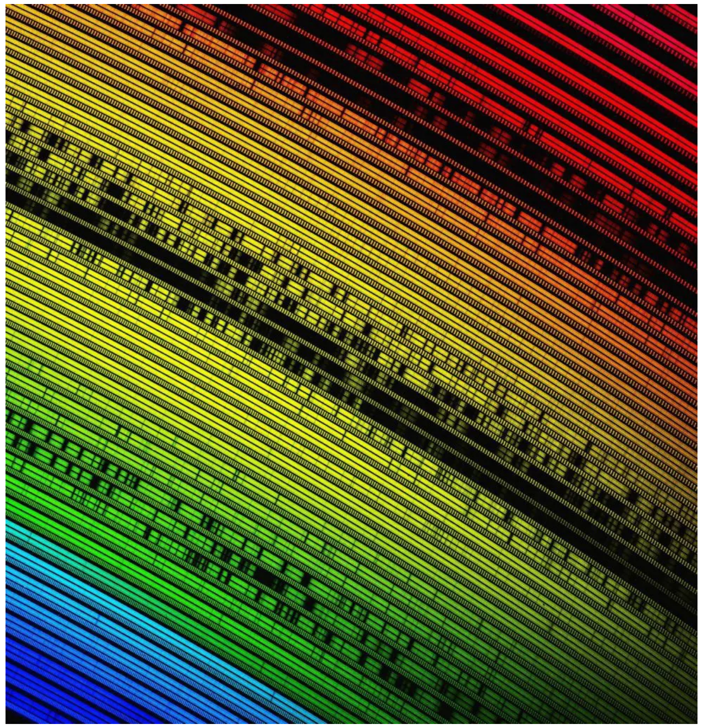

Figure 1.4: An image showing multiple bands representing different echelle orders in SPIRou. The light is initially dispersed to generate multiple orders spanning short wavelength ranges which are then separated by a cross-dispersing element. This results in wavelength varying along both the x and y directions, shown as a 2D spectrum. Each order will have three fibres: the science fibre, reference fibre, and the Fabry-Perot spectrum for wavelength calibration.

1.5.1 Abundance Notations

Stellar abundance measurements are often mathematically defined as a ratio between an element Q and hydrogen H, or how many atoms of element Q there are for every hydrogen atom. Here, the number of hydrogen atoms is kept constant at 10^{12}. The number of atoms of Q is denoted simply as q, and h is the number of hydrogen atoms. The absolute stellar abundance of Q, written as $A(Q)$, is simply

$$A(Q) = \log_{10}\left(\frac{q}{h} \times 10^{12}\right) = \log_{10}(q) + 12 = \log_{10}(q) + A(H) = \frac{Q}{H} \tag{1.5.2}$$

In the literature, this abundance ratio is often written relative to the corresponding ratio in the Sun (Hinkel et al., 2022). This is denoted by square brackets:

$$\left[\frac{Q}{H}\right] = A(Q_*) - A(Q_\odot) = log_{10}(q_*) + A(H) - log_{10}(q_\odot) - A(H) = log_{10}\left(\frac{q_*}{q_\odot}\right) \tag{1.5.3}$$

The two key methods to retrieve atmospheric parameters and elemental abundances from spectra are the equivalent widths method (EW) and the spectral synthesis method (Allende Prieto, 2016). In the following sections, we go over each in detail.

1.5.2 Equivalent Widths

The equivalent width (EW) of a spectral line is defined as the width of the spectral continuum that has the same area as the area of the absorption line below the continuum level, typically after a Gaussian profile is fit. Mathematically, this is defined as

$$EW = \int \left[1 - \frac{F(\lambda)}{F_o}\right] d\lambda \tag{1.5.4}$$

where $F(\lambda)$ is the observed flux at wavelength λ, and F_o is the flux of the continuum at the same wavelength. Having a larger EW means that you have a deeper absorption feature, where a larger fraction of photons is being absorbed at a certain wavelength in the photosphere. The measured EW is compared to a pre-tabulated curve of growth for a given spectral type that maps EW to an abundance. Alternatively, the measured EW can be compared to an EW computed through a radiative transfer code which will depend on both certain stellar parameters and the elemental abundance (Blanco-Cuaresma, 2019).

1.5.3 Spectral Synthesis

The general principle of the synthetic spectra method is that we compare observed data to theoretical spectra with known parameters that are either generated "on-the-fly" or interpolated using pre-computed grids and compare the difference using an optimization routine (Blanco-Cuaresma, 2019). How are these spectra synthesised? We first take a stellar atmosphere model which will dictate how the composition and thermodynamic variables vary with atmospheric depth. These are dependent on the temperature structure, density and opacity sources. The spectrum is then computed using a radiative transfer code. Radiative transfer is the physical process through which energy, as radiation, is transmitted through and interacts with its environment. It is based on the radiative transfer equation

$$\frac{dI_\nu}{ds} = -\alpha_\nu \times I_\nu + j_\nu \tag{1.5.5}$$

where I_ν is the specific intensity at frequency ν, s is the distance along line of sight, α_ν is the absorption coefficient at frequency ν, and j_ν is the emission coefficient at frequency ν. The code then solves this equation at every point of a grid of the parameter space. These parameters include the temperature, opacity, and composition distribution that is provided by the stellar atmosphere model. This calculates how the radiation is absorbed and scattered as it passes through the atmosphere and allows the program to generate a spectrum accordingly. The spectrum will include effects like Doppler broadening due to motion, pressure broadening, and thermal broadening of spectral lines. Stellar models will often assume local thermodynamic equilibrium (LTE) which simplifies these calculations significantly. This entails that sections of the star's interior on a small enough scale will be in a thermally isolated, steady-state condition. In simpler terms, the mean free path of photons is less than the scale over which thermodynamic properties change. However, in certain stellar atmospheres, like those in the coolest or most metal-poor stars (Amarsi et al., 2022; Blanco-Cuaresma, 2019), this assumption will break down. Thus, NLTE effects such as non-thermal excitation and ionisation need to be considered. While this often means calculations are more computationally expensive, they are important to avoid discrepancies between theory and reality (Hinkel et al., 2024).

1.6 Difficulties in M Dwarf Spectra

While there is no model that can perfectly replicate all stellar processes, some stars are more easily modelled than others. FGK star elemental abundances have historically been reliably measured at optical wavelengths, thanks to numerous distinct spectral features that match well with stellar atmosphere models and atomic linelists at the temperatures of these stars ($\geq$ 4000 K). Unfortunately, modelling M dwarf spectra is notoriously difficult, making it challenging to accurately determine elemental abundances values. Due to their cool temperatures, their spectra are plagued by broad molecular bands such as TiO and VO (Allard et al., 2000) that obscure the continuum flux level and make measuring abundances of other individual elements all the more challenging (Souto et al., 2022). These complex molecular features — including those of OH, CO, and H_2O — overlap with several atomic lines, which then affect abundances inferred from EWs when not properly accounted for. These molecular bands, alongside factors such as NLTE effects or deep convective zones in M dwarf interiors (Browning, 2008; Mullan and MacDonald, 2001), mean that M dwarf models will often fail to align with observational data (Jahandar et al., 2024). Even in areas relatively clear of molecular bands, dense forests of absorption features will often blend together if one observes at low resolutions. As a result, the origin of certain features in spectra will be unclear. They could be attributed to spectral noise, telluric contamination, uncertain sources of opacity or missing lines from incomplete linelists (Khata et al., 2020). M dwarfs are also inherently faint at optical wavelengths, peaking instead in the near-infrared wavelengths. This essentially cuts off access to lines in the optical regime (Souto et al., 2017), and further motivates the need to observe M dwarfs in the nIR. This phenomenon is shown in Figure 1.5, showcasing a relative lack of spectral lines at optical wavelengths for an M dwarf. Sometimes, the observed spectra are missing lines that we might expect to be there. The strength of spectral lines is temperature dependent. To illustrate this point, we compare in Figure 1.6 three synthetic spectra at three different temperatures. At the lowest temperature of 3000 K, the spectral features of iron and nickel effectively vanish. This means that for spectra of cool stars, it will be especially difficult to clearly identify and analyze spectral lines for such elements. This figure also demonstrates the degeneracy temperature can have with abundance measurements and highlights the importance of accurate inputs for the models.

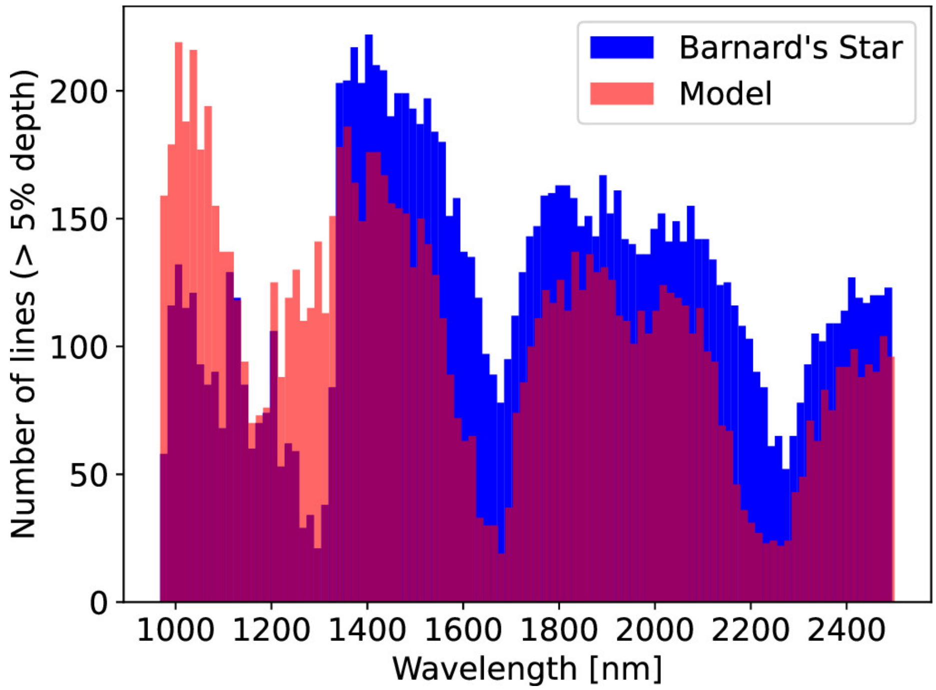

Figure 1.5: Figure from Jahandar et al. (2024) comparing lines in their observed SPIRou spectrum and in the models. One can see the excess of lines in the models at lower wavelengths are not reflected in the observed data, and vice versa.

Another reason why M stars are hard to study is that they are often magnetically active. All M dwarfs are magnetically active to some degree (Reiners, 2012). We know that the magnetic activity of stars will influence their spectra via Zeeman broadening (Reiners, 2014). The magnetic activity also varies over time, creating an inherent dispersion in the data. H-alpha at 650 nm is a line sensitive to chromospheric activity, making it a good indicator of magnetic activity. While some studies may filter out active stars using their H-alpha equivalent widths, it is not always feasible to select science targets based solely on their level of activity (Newton et al., 2015). Thus, magnetic activity remains another limiting factor when analyzing M dwarf spectra. Overall, these are all persistent issues in the literature, motivating limited attempts to calibrate M dwarf spectra.

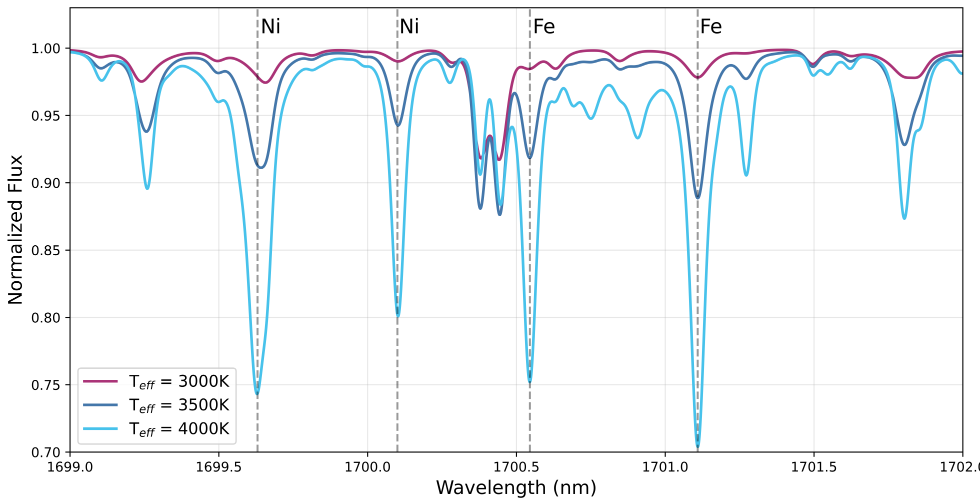

Figure 1.6: An illustration of how spectral lines can change and seemingly disappear at lower temperatures. Three model spectra were generated with temperatures of 3000 K, 3500 K, and 4000 K using MARCS and Turbospectrum. This region shows two nickel lines at 1699.62 nm & 1700.09 nm and two iron features at 1700.54 nm & 1701.10 nm.

1.7 Motivating the Framework

Because these inhomogeneities lead to large differences in derived atmospheric parameters and abundances, this has caused large deviations in literature values of elemental abundances (Hinkel et al., 2016; Jofré et al., 2017). With so many fields within astronomy reliant on getting accurate details on the chemistry of M dwarfs, it is essential to ensure the reliability of these derived abundances. Unlike effective temperature and surface gravity, elemental abundances can not be obtained through independent methods, further complicating efforts to ensure accuracy in results. Previous works either do not calibrate their results (Souto et al., 2017) or seek to calibrate only a subset of elements at low spectral resolutions (Veyette et al., 2017), which is insufficient for accurate line fits (Iyer et al., 2023; Souto et al., 2022). Several research groups have already developed their own codes and techniques to address these nuances (Blanco-Cuaresma, 2019; Hinkel et al., 2014). However, a large subset of the available frameworks used to extract elemental abundances from spectra are either black boxes or proprietary.

In order to facilitate a future calibration of our own, this motivated our need for a customizable framework to be built, which became my Master's project. I developed a flexible framework that can analyse high-resolution spectra in a comprehensive fashion, where each step of the process could be controlled and modified as needed. The development of a custom framework is motivated by the need to ultimately calibrate M dwarf abundances in hopes of alleviating many of the aforementioned concerns regarding the reliability of M dwarf abundance measurements in the literature. In Chapter 2, I describe SPIRou's capabilities in observing M dwarfs. I then provide justification for each of the choices in my framework and outline the details of each step needed to derive elemental abundances. I also discuss optional features that are specially designed to combat the difficulties in studying cool star spectra. In Chapter 3, I apply my framework to two stars in different temperature regimes ($\sim$3200 K and $\sim$4200 K) with two unique science cases. I present the extracted abundances for 13 elements. Finally, in Chapter 4, I conclude by interpreting the results and providing a summary of potential applications of this work.

Chapter 2

Methodology and Development

2.1 The Data

For our purposes, we will be using the Spectropolarimètre Infrarouge, referred to as SPIRou, located on the 3.6m Canada-France-Hawaii Telescope on Mauna Kea in Hawaii. It is a high spectral resolution (R$\sim$75,000) near-infrared spectropolarimeter that has a broad wavelength coverage in the YJHK bands, from 0.98 - 2.35 µm (Donati et al., 2020). Specifically, it is an achromatic polarimeter fibre-feeding a cryogenic high-resolution echelle spectropolarimeter. SPIRou was originally designed to detect and characterise exoplanets using high-precision velocimetry, but SPIRou's coverage and resolution make it ideal for our purposes of observing M dwarfs and mitigating the previously stated discrepancies (Jahandar et al., 2024). Because the luminosity of M dwarfs peaks in nIR, that is where we find most of the absorption features to be used for analysis. The broad wavelength coverage provides access to spectral features from many elements of interest for exoplanet characterization and galactic archaeology. Another important feature of SPIRou that makes it somewhat unique among nIR spectrographs is its access to the K-band between 2.0 – 2.4 µm. K-band coverage provides access to the so-called "CO forest" that resides in that regime, equipping us with a more robust sample of spectral features to measure C abundances in cool stars. A high spectral resolution is needed in order to resolve and identify absorption lines as well as their profiles. An example of this is shown in the following comparison between APOGEE's resolution of R∼22,500 and SPIRou's resolution of R∼75,000 in Figure 2.1 (Souto et al., 2017).

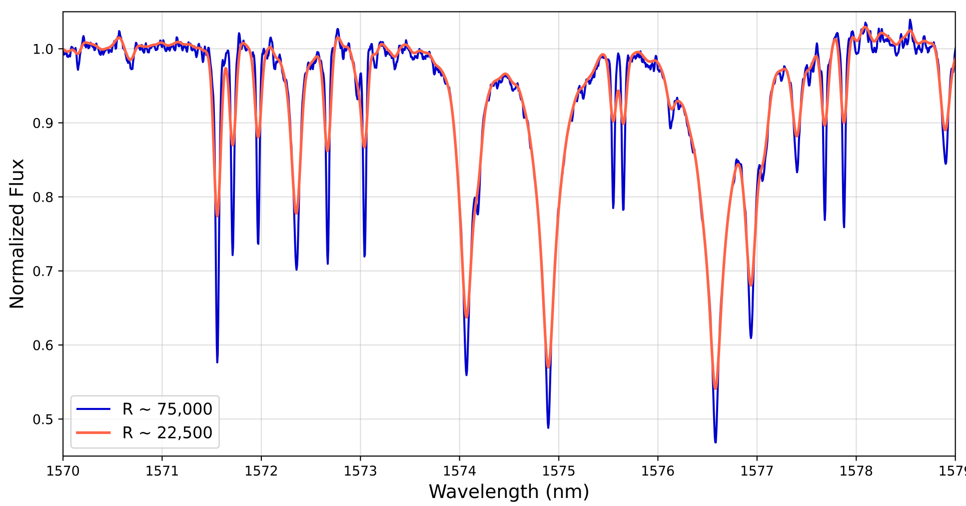

Figure 2.1: Comparison of spectra from SPIRou with R∼75,000 and the same spectra convolved down to APOGEE's lower resolution, R∼22,500. Despite the data itself being identical, it is clear to see the drastic difference made by a higher resolution.

Our SPIRou observations are initially reduced using A PipelinE to Reduce Observations (APERO; Cook et al. 2022), which outputs 1D extracted fluxes that have been corrected for detector gain, blaze, and artifacts, in addition to being calibrated and corrected for telluric atmospheric absorption.

2.2 Analysis Justifications

My abundance analysis framework uses the iSpec software (Blanco-Cuaresma, 2019; Blanco-Cuaresma et al., 2014), an open-source spectroscopic tool that is commonly used in the scientific community to analyse spectra and extract atmospheric parameters. It was recently updated with a whole suite of radiative transfer codes (Blanco-Cuaresma, 2019) and while I tested other tools, iSpec has proven to be the best choice for our purposes. Specifically, I explored two alternative options for the underlying analysis software: Synspec (Hubeny and Lanz, 2017) and PySME (Piskunov and Valenti, 2017; Valenti and Piskunov, 1996). PySME was adapted from the original IDL code Spectroscopy Made Easy (SME). Ultimately, I moved away from PySME because it has fewer relevant functionalities than iSpec. Synspec was promising because it had clear documentation and existing functionality that worked with a variety of input stellar atmosphere models and radiative transfer codes that are commonly used in the literature. However, while iSpec and PySME have the functionality to easily change and parse through the linelists, there is extremely limited documentation about which linelists were being used within Synspec. Upon further inspection, we concluded that the atomic and molecular lists were for solar parameters and were not applicable to M dwarfs.

We have elected to use synthetic spectrum analysis over equivalent widths. As Blanco-Cuaresma (2019) demonstrates, there are significant differences between the results derived from the two methodologies and so, this is a crucial choice. While the advantage of using the equivalent width method is that it requires less computation time, it is much more likely to inaccurately estimate abundances in the case of blended lines because the full line profiles are not being considered. Saturated or broadened lines (Freckelton et al., 2024) are not well represented by Gaussian profiles, meaning this method is less reliable for metal-poor and cooler stars (Blanco-Cuaresma, 2019). Spectral synthesis methods, despite being more computationally expensive, can reproduce blending effects much better and are therefore necessary for a better analysis (Blanco-Cuaresma, 2019). In an effort to reduce this computation time, we do not generate the entire spectrum. Rather, we only generate synthetic spectra for defined line regions for each element.

The second choice we made is to use the stellar atmosphere model MARCS (Gustafsson et al., 2008) and the radiative transfer code Turbospectrum (Alvarez and Plez, 1998; Plez, 2012). For the stellar atmosphere, MARCS is a common choice for spectroscopists (Hejazi et al., 2023; Martioli et al., 2022). Its range of grid values for effective temperature (2500 K < T_{eff} < 8000 K), surface gravity (-0.5 dex < log$g$ < 5.5 dex) and metallicity (-5 dex < [M/H] < 1 dex) is suitable for the vast majority of cool stars in the solar neighbourhood. MARCS also includes models computed with plane-parallel and spherical geometries. Other options such as ATLAS9 and PHOENIX were explored. ATLAS9 models cover a parameter space of T_{eff} from 3500 K to 8750 K in steps of 250 K, log$g$ from 0.0 dex to +5.0 dex in steps of 0.5 dex and [M/H] from +1.0 dex to -5.0 in steps of 0.5 dex (Kurucz, 2005). It only works with plane-parallel geometric atmospheres, neglecting 3D convection (Freckelton et al., 2024). Plez (2011) did an analysis comparing the performance of ATLAS, MARCS and PHOENIX for cool stars specifically. They found that while the three agree above 4000 K, an issue with ALTAS arises specifically with the nIR flux for T_{eff} < 4000 K. Because no ATLAS models go lower than 3500 K - a regime includes many M dwarfs of interest - it is ill-suited for our purposes. We then considered the new PHOENIX grid which uses the ACES descriptions for equations of state, henceforth called PHOENIX-ACES (Husser et al., 2013). Husser et al. (2013) argued that the ACES equations of state are more suitable for modelling cool stellar atmospheres. Work from Passegger et al. (2016) compares PHOENIX-ACES to spectra for a few benchmark stars between 3000 - 3500 K and finds good agreement on derived T_{eff} and log$g$. However, they do find large discrepancies up to 3σ to literature values of [M/H], highlighting the difficulties in accurately estimating M dwarf stellar parameters. Strictly speaking, iSpec only has the functionality for MARCS or ATLAS9 so we could not use PHOENIX-ACES. MARCS is an acceptable choice, as the performance between MARCS and PHOENIX-ACES is roughly equal (Plez, 2011). Different groups will use different stellar atmosphere models and a detailed comparison between the two is beyond the scope of this thesis.

For the radiative transfer code, the options available through the iSpec wrapper are SPECTRUM (Gray and Corbally, 2014), MOOG (Sneden et al., 2012), SME (Piskunov and Valenti, 2017), and Turbospectrum (Alvarez and Plez, 1998; Plez, 2012). All of these codes assume LTE, which we remind the reader is well-known to be a limitation and may influence the derived abundances for cool dwarfs (Olander et al., 2021; Short and Hauschildt, 2003). At first, we attempted to use SPECTRUM, which could not accurately represent the depth or line profile of spectral lines or molecular features in the spectrum. In the latest release of SME in 2020, a bug that impacted the concentration of negative ions was introduced. Because this heavily impacts M dwarfs, we elected not to use it. Between MOOG and Turbospectrum, I settled on using the latter. This is because it is commonly used throughout the literature and it is one of the fastest radiative transfer codes (Blanco-Cuaresma, 2019). There have been studies that directly compare and contrast the results derived when using different codes, methods, and atmospheres, and they find intrinsic differences even when starting from the same stellar parameters and linelists (Blanco-Cuaresma, 2019; Hinkel et al., 2016). For example, inherent differences in how the line-broadening parameters are handled across codes can cause discrepancies (Blanco-Cuaresma, 2019). In all these methods, there are complications in real-life data that are difficult to replicate - NLTE, 3D geometries, optically thin layers for metal-poor stars (Plez, 2011). These discrepancies show why it is important for us to carefully consider and select each part that goes into our framework and it is a key factor in why different papers will get different results for abundances and derived stellar parameters.

2.3 Steps of the Framework

2.3.1 Set-Up

After we received the data, we converted the files into .txt files readable by iSpec, consisting of three columns with wavelength, flux, and flux uncertainty. Because iSpec does not tolerate NaN values, any wavelengths with NaN fluxes are removed. The next step is to apply a radial velocity (RV) correction and a global continuum normalisation, both of which are done using the iSpec functionality. To calculate the RV correction, we use a cross-correlation function between the spectrum and an atomic line mask to find the velocity profile (Allende Prieto, 2007). The atomic line mask is developed from the VALD solar spectrum (T_{eff} = 5777.0 K, log$g$ = 4.44 dex and [M/H] = 0.02 dex) spanning 300 - 1100 nm, using the *cross_correlate_with_template* function in iSpec. The spectrum is then shifted according to the derived value. For most of our cases, using a solar spectrum as a comparison is adequate. However, upon testing with a variety of stars, we have seen cases where using the solar template for cooler M dwarfs returns unreliable values for the radial velocity. We are also restricted because while the program does offer masks for each spectral type, the ones available for cool stars fall out of SPIRou's wavelength range and cannot be used as a comparison. Therefore, we plan to use a custom template better suited for these cases. Once the RV correction is complete, we perform a global continuum normalisation across the entire spectrum. To do this, we use the *fit_continuum* and *normalize_continuum* functions in iSpec. These functions work by using a median filter of length 0.05 nm to identify noise and a maximum filter of 1.0 nm to block fluxes in absorption lines. The spectrum is then normalised by dividing all fluxes by a model which fits a b-spline of 2 degrees to the observed spectrum every 5 nm. A visualization of this procedure is shown in Figure 2.2.

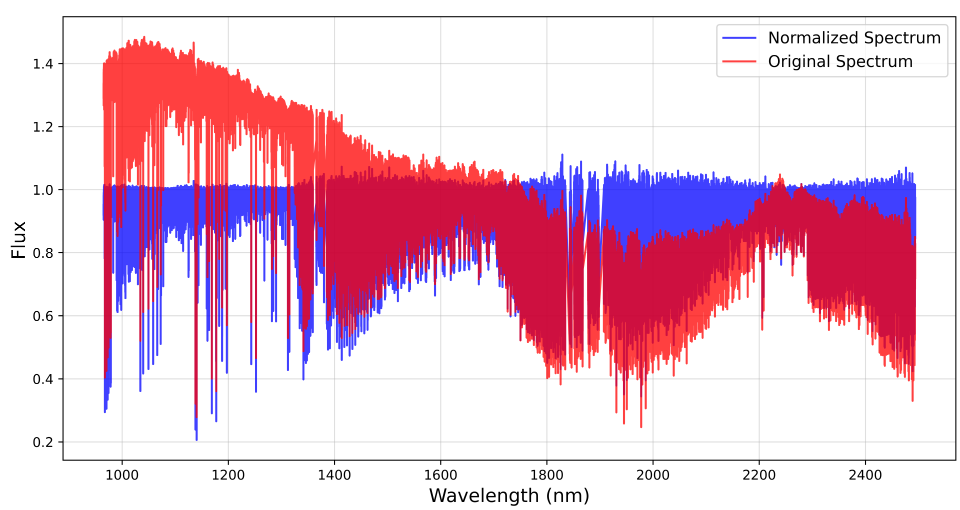

Figure 2.2: A demonstration of the global continuum normalization for a spectrum of Barnard's Star, before (red) and after (blue) the normalization.

The next step is establishing the linelist for the line-by-line determinations of elemental abundances. I start with the linelist derived from the VALD catalogue (Piskunov et al., 1995), from 300 - 1100 nm and 1100 - 2400 nm to cover our full wavelength range. I then use iSpec to identify linemasks for regions around each spectral line and create a custom linelist for the target of interest. To avoid spurious results from shallow or blended lines, each line must have a minimum depth of 0.05 (meaning 5% of the continuum), a maximum depth of 1.0, and a maximum atomic wavelength difference of 0.01 nm. In the case of cool stars with issues of continuum placement, weak lines are especially commonplace so this helps to remove them. I visually inspect all line masks before proceeding with my line-by-line analysis. I manually remove any tellurically contaminated lines, double lines, noisy lines where the core of the absorption line is not clear, extremely blended lines, and lines visibly discrepant to the corresponding lines in the model spectrum for reasons unknown, like artifacts or spectral noise. These cases are somewhat subjective. Oftentimes, if an element has few lines, then these criteria are relaxed. For example, the line region itself can sometimes be modified to exclude extraneous features in the nearby continuum. We repeat this process on a star-by-star basis so that the line selections are fine-tuned and adapted as needed.

We ultimately selected a list of 13 elements for the science targets analyzed in this thesis: C, O, Na, Mg, Al, Si, K, Ca, Sc, Ti, Cr, Mn, and Fe. This element list depends not on the framework but rather, the availability of the corresponding lines in the star's spectrum. It is important to note that we found that atomic carbon and oxygen lines are too shallow and too low in quantity when it comes to cool dwarfs. Instead, to measure C and O abundances, we use molecular CO and OH lines, respectively.

This assumption is not uncommon, as other studies have previously done this for cool stars where molecular features are commonplace (Hejazi et al., 2023; Sharma et al., 2024). The nIR regime contains a wealth of lines of OH in the H-band and the CO lines via the K-band in our data, increasing the sample of CO and OH lines from which to draw. Souto et al. (2017) note that OH lines may be sensitive to microturbulence. However, their wavelength range was limited to the H-band, not including the K-band which contains many CO features. Further investigation by Hejazi et al. (2023) showed with their access to the K-band that CO lines are much more sensitive to variations to microturbulence. It is worth mentioning that nitrogen is notably missing from our elemental list. While we do acknowledge the importance of nitrogen in elemental ratios in both planet formation and atmospheric studies (Cridland et al., 2017; Ohno and Fortney, 2023a), we found that the model lines generated for CN were not suitable for analysis. This is because the identified CN lines were either too weak to be differentiated from nearby spectral lines or did not match the corresponding lines in the model.

2.3.2 Synthesis

The first step is to set up the abundance grid over which I will compute forward models of synthetic spectra. We want to have a wide enough range that we can capture especially metal-rich or poor abundances, but with sufficient fidelity that allows us to obtain accurate results. We also aim to avoid generating too many models, as this quickly becomes computationally expensive. We adopt a grid of five abundances of [-0.5, -0.25, 0, +0.25, +0.5] dex, that are centered on the solar abundance for each element. We adopt solar abundance values from Asplund et al. (2009). We then use a custom function that calls the *generate_spectrum* function from iSpec to generate five synthetic spectra. This function takes in the parameters of effective temperature, surface gravity, metallicity, as well as rotational velocity ($v \sin i$), microturbulence, macroturbulence, alpha enhancement, and a fixed abundance list. This fixed abundance list consists of individual elements whose abundances I control independently of the overall metallicity, and this is the parameter that the abundance grid modifies over each iteration. The *generate_spectrum* function then synthesizes a spectrum over some wavelength range by combining the Turbospectrum code and the inputted parameters over a grid of MARCS stellar atmosphere models. We generate five synthetic spectra by modifying the fixed abundance value of one element according to the abundance grid, leaving the other elemental abundances to be the solar value added to the user-inputted value of [M/H]. For the parameters of temperature, surface gravity and metallicity, we adopt values from the literature. While we could try and derive these values from the spectra ourselves, as other papers have done and is feasible to do, this is ultimately not the focus of our research. During this initial synthesis step, all other stellar parameters are fixed (e.g. T_{eff}, log$g$, [M/H]). Their values are chosen on a case-by-case basis from the literature. Recall that spectroscopic parameters for M dwarfs can vary widely in the literature and so, care must be taken to select an appropriate value for this abundance analysis.

For M dwarfs that do not have values in the literature or have values derived using questionable methodologies, there are known empirical relations and tracers that can estimate these quantities independently of the spectra. For the effective temperature, we use equation 4 from Mann et al. (2015),

$$T_{eff}/3500K = a + bX + cX^2 + dX^3 + eX^4 \tag{2.3.1}$$

where a = 3.245, b = -2.4309, c = 1.043, d = 0.2127, e = 0.01659, and X is the absolute K-band magnitude. Equation 6 from Mann et al. (2015) is used if [Fe/H] is known for the star,

$$T_{eff}/3500K = a + bX + cX^2 + dX^3 + eX^4 + f([Fe/H] \tag{2.3.2}$$

where a = 2.835, b = -1.893, c = 0.7860, d = -0.1594, e = 0.01243, f = 0.04417, and X is the absolute K-band magnitude. These equations from Mann et al. (2015) use colour magnitudes from the Gaia database and best-fit coefficients from a Colour-Temperature relation. Rojas-Ayala et al. (2012) uses the Na I doublet and Ca I triplet in the K-band as metallicity indicators, and we refer to their methodology to derive [M/H] when necessary. For calculating surface gravity, we refer to equation 2 from Bean et al. (2006),

$$\log g = 5.491 - 3.229M_* + 5.949M_*^2 - 4.929M_*^3 \tag{2.3.3}$$

which calculates log$g$ in cgs units based on stellar mass M_* in solar units for stars between 0.123 - 0.621 M_*. The effects of microturbulence and macroturbulence are also considered within the framework. These are calculated using the *estimate_vmic* and *estimate_vmac* functions in iSpec that apply the empirical relation derived from the UVES Gaia-ESO Survey (Blomme et al., 2022; Jofré et al., 2014). Within the MARCS models, the alpha enhancement is calculated from the input metallicity. For [M/H] = +1 to 0, alpha is 0, but the alpha enhancement increases as M/H decreases. If the star is metal-poor, this alpha enhancement is applied to alpha elements, noticeably affecting the synthetic spectrum. We manually set the alpha enhancement to zero because we do not want it to unknowingly enhance the alpha element abundances that we get. It is a well-known effect that rotational broadening from stars with high ($v \sin i$) values will affect the line profiles. In fact, rotational velocity, macroturbulence and resolution are all degenerate parameters, making it quite challenging to separate their effects with spectroscopy alone (Blanco-Cuaresma, 2019). This is further complicated by the fact that most stars do not have accurate literature values for $v \sin i$, which can then go on to negatively impact our derived abundances.

Our ultimate goal for this step in the framework is to determine line-by-line abundances through a χ^2 minimization between the observed and model data over a grid of elemental abundances. The synthetic spectra are convolved down to R$\sim$75,000 with a Gaussian broadening kernel to match SPIRou's resolution. It is then interpolated onto the same wavelength grid as the observed spectra. We only generate these models for segments outlined by the line regions that were previously defined in the linelist, along with a margin of 0.2 nm on either side. This step is done to reduce the computational load, as the continuum and tellurically affected regions are not included in subsequent steps in our abundance analysis. Once the models are generated, we aim to compare them to the data. Five spectra between $\pm$ 0.5 dex is insufficient to resolve the most likely abundance for each line to a high enough level of precision. To avoid generating more models, we take advantage of the fact that the generated models for each line will typically form in a continuous pattern. An interpolation function then fits for and replicates this pattern by varying the abundance value. This then effectively gives us a finer grid of models to compare against without significantly increasing computation time. Therefore, we interpolate to make 100 spectra between -0.5 and 0.5 dex. We do expect minute differences between these and actual models generated, but they would cause very small variations that ultimately cause a very small error - smaller than the other sources of error present. While this technique cannot be utilized for too sparse an abundance grid, as the behaviour of the lines is not uniform, we found that five models is a reasonable value to avoid this issue. Any strange behaviours arising in the interpolated spectra are most likely caused by contaminated or blended features and are removed in the visual inspection step. An example of a silicon line and the corresponding generated models are shown in Figure 2.3.

We then perform a χ^2 minimization routine on a line-by-line basis between the grid of interpolated model spectra, which vary solely by the elemental abundance, and the observed spectra. An example is included in Figure 2.3. We define the interior line region around the core of the line, separating it from the local continuum region. The interior line region is used as the fitting window for the χ^2 minimization. This process was originally done by calculating the second derivative of the flux to detect where the curve of each line started. However, this methodology was not as precise as we wanted and so, we now simply use the line masks as determined by iSpec. This step is meant to reduce the effect of blended lines or noise in the wings on the derived abundance. These persistent issues in cool star spectra will skew the abundance to appear higher than it really is. One option that was explored in the beginning of this project was to use an MCMC in place of the χ^2 minimization. We ultimately decided against it, as it was even more computationally expensive and a χ^2 minimization is both suitable and widely used in synthetic spectral analysis (Brinkman et al., 2024b; Hejazi et al., 2023). We then output the plot of the spectral line and the χ^2 minimization. Each

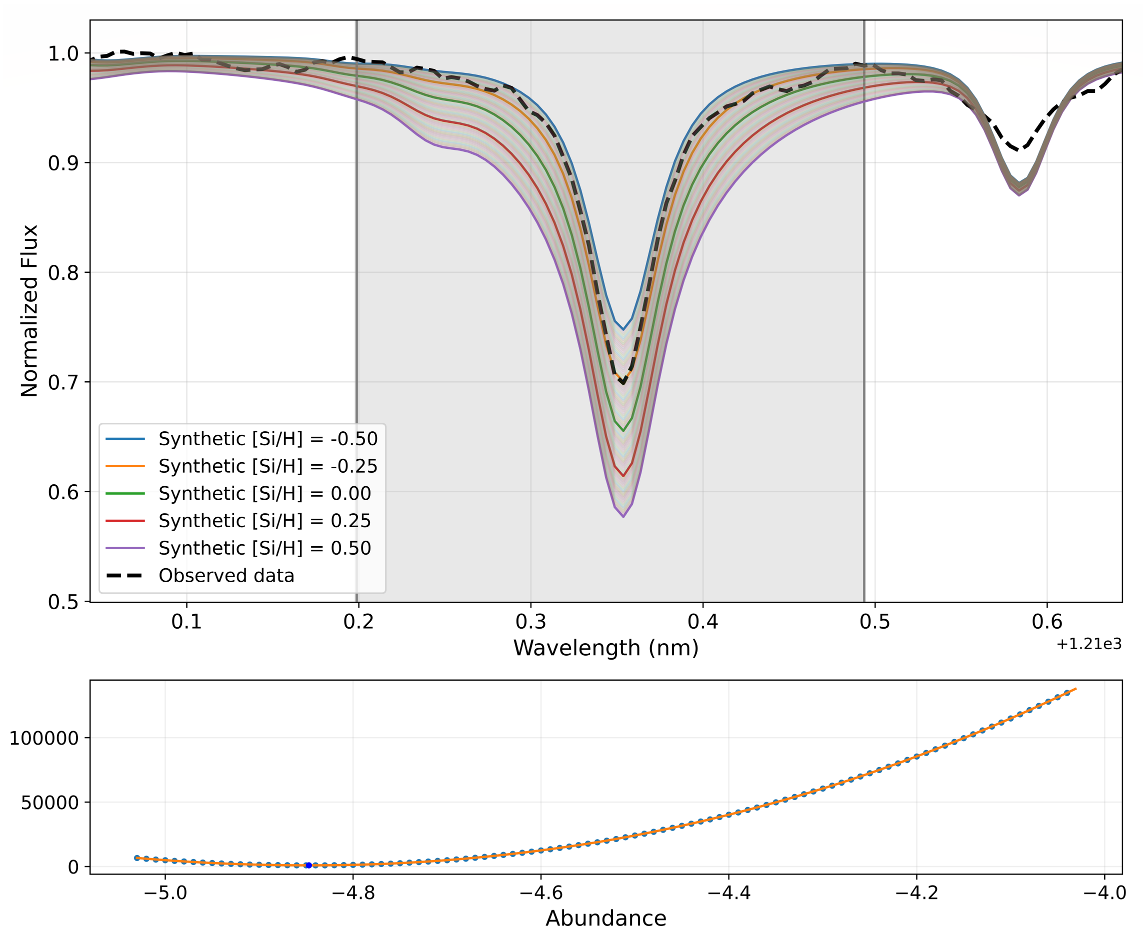

Figure 2.3: Top: Demonstration of the framework for a silicon line at 1210.35 nm. The grey region represents the interior line region and the white region is the assumed continuum region. A noted feature on the right that would bias the χ^2 minimization is excluded. Bottom: A plot of the χ^2 minimization between the observed spectra and the models for the silicon line, deriving A(Si) = -4.847 or [Si/H] = -0.317.

line has its own unique abundance value, leaving us with a distribution of values for abundance for each element. We then take the median and standard deviation of this distribution as the reported abundance and random error for each element.

2.4 Optional Features

Within the overall framework, additional steps are added to ensure the robustness of our results:

2.4.1 Line shifts

While we use the RV correction to ensure the data and the models are shifted to the rest frame, some spectral features do not line up with the line's position in the VALD linelist. This leads to a wavelength offset between the observed line and the model lines. This effect has been similarly described in previous studies (Jahandar et al., 2024), and is most likely due to uncertainties in the linelist, inaccuracies in the models being unable to replicate stellar behaviours, or other unknown factors. We remain agnostic to the source of any line position discrepancies and run an additional routine where the code identifies the position of the lowest point of the spectral line for both model and observed data. If the two do not align along their shared wavelength grid, it finds the difference in positions and applies said difference to the observed data on a line-by-line basis.

2.4.2 Pseudo-Continuum Normalization

It is well-known that a common issue with M dwarf spectra is that the continuum is obscured by broad molecular bands (Melo et al., 2024). This means that while we have normalised the continuum over the entire spectrum (see section 2.3.1), this broad approach means the continuum is at less than unity for some lines whereas the model spectra place the local continuum at or close to unity. An example of this is

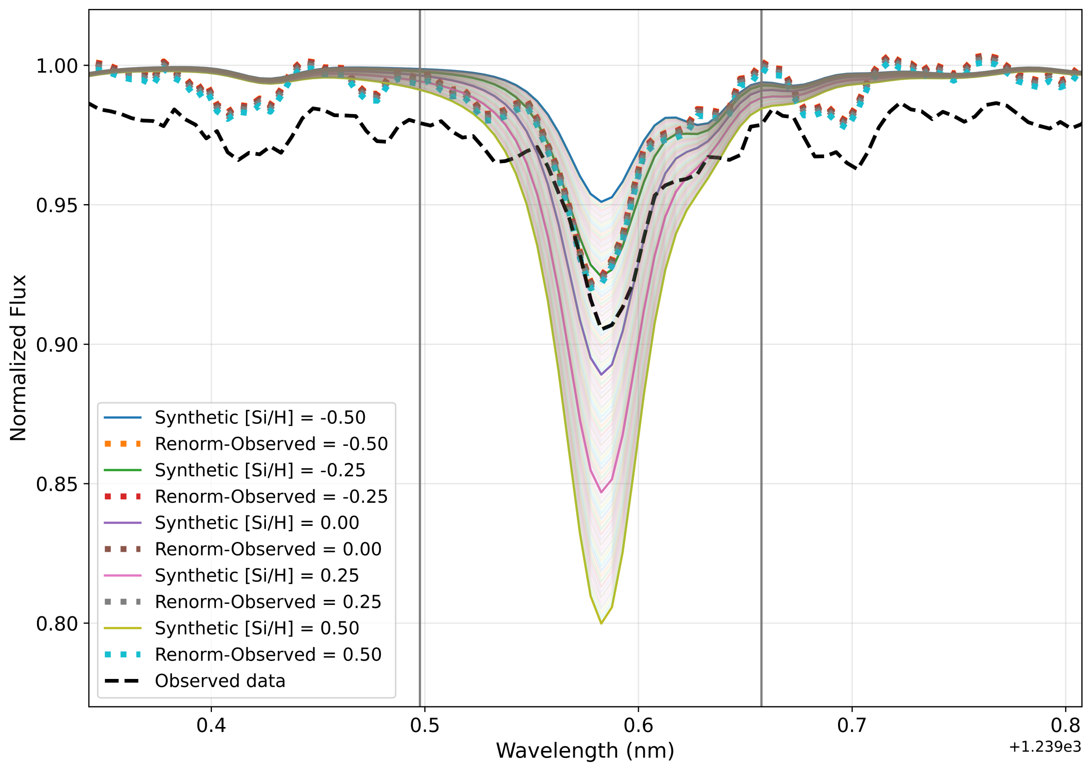

Figure 2.4: Demonstration of the pseudo-continuum normalization procedure for an alternate silicon line at 1239.58 nm. The original spectrum's continuum level appears lower than unity. The dotted lines show the location of the renormalized observed spectral line, which see good agreement with the models.

seen in Figure 2.4. Thus, we developed a pseudo-continuum normalization procedure as an optional step of our framework to ensure that the local continua of the observed spectra and the synthetic spectra are in close agreement in the vicinity of our line regions. This helps to ensure that any variation in the χ^2 value across our abundance grid is capturing variations in the line depth and width, rather than being dominated by variations in the local continuum. Our pseudo-continuum normalization is a modified version of the procedure presented in Hejazi et al. (2023), who in turn adapted their methodology from Santos-Peral et al. (2020). They use a low-order polynomial fit over the residuals between the observed data and the model, and three stages of σ-clipping to determine the continuum data points. A second polynomial is then fit over these data points, by which the observed data is renormalized. It is then this renormalized spectrum that is compared to the model spectra to derive the elemental abundances. When we originally implemented their methodology, we noticed this procedure would either change the shape of the line itself or be heavily influenced by the presence of nearby lines. Line depth and profile are equally important for obtaining accurate abundances. A possible explanation for this behavior is that for broadened or saturated spectral lines, the σ-clipped data points would also include those closer to the core of the line that inherently have a lower flux. This would then form a slight parabolic shape to the polynomial fit. Santos-Peral et al. (2020) likewise acknowledges this to be the case, although they do not aim to resolve the issue. The methodology of the pseudo-continuum normalization was modified in our framework as a result. The new process likewise σ-clips the residuals between model and observed data in the continuum region alone. However, instead of a polynomial fit, we calculate the median of the flux on corresponding wavelengths to the σ-clipped points on both the model and observed spectra. The framework will calculate the difference between these medians and offset the flux of the observed spectra by said difference. An example of the renormalized spectra is shown as the dotted lines in Figure 2.2. However, we would like to note that attempting to develop a single methodology to normalize this pseudo-continuum is rather challenging, as each spectral line will be unique and complex. Recent papers have proposed their own methodologies to address how to approach the pseudo-continuum. For example, Melo et al. (2024)

calculate an uncertainty tied to the pseudo-continuum by introducing shifts of -2%,-1%,+1%, and +2% in the normalized flux of the spectra and recomputing the derived abundances.

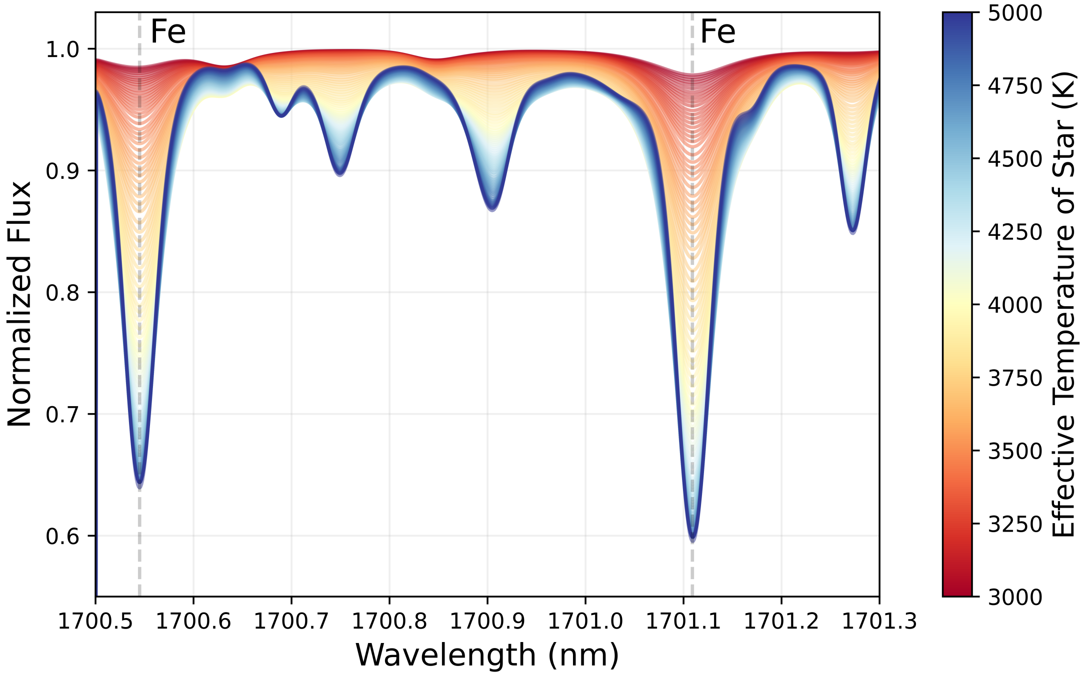

Figure 2.5: We vary T_{eff} in the model spectrum for the same line regions from 3000 K (red) to 5000 K (blue) in steps of 20 K. We fix the values of log$g$ and [M/H]. Such an exercise highlights the sensitivity of the models to variations in assumed stellar parameters.

2.4.3 Additional Error Analysis

Potential sources of uncertainty from blending, degeneracies of stellar parameters, and spectral noise are known to occur. For line-by-line spectroscopic analysis, abundance measurement errors in the literature are often quantified using only the dispersion between lines of the same element. While this is a key source for error, it is likewise important to acknowledge the influence of the assumed stellar parameters in generating spectra. As seen in Jahandar et al. (2024) and Melo et al. (2024), even small variations in the temperature, metallicity and surface gravity used in synthetic spectra can heavily influence the results. This effect is visualized in Figure 2.5. Thus far in the framework, we have only considered fixed stellar parameters such that the only source of error is the dispersion among N lines. We need a reliable way to account for uncertainties in stellar parameters such as T_{eff} and [M/H] and quantify their respective contributions to the overall error budget of our abundance measurements. We adopt the approach taken by Hejazi et al. (2023), which they in turn adapted from Souto et al. (2017). We modify the T_{eff} and [M/H] one at a time by sampling from their respective errors reported in the literature using a Gaussian distribution centered on best-fit values with 1σ error bars. We repeat this sampling a number of times and run the complete abundance analysis for each new value of either T_{eff} or [M/H] and save the final abundance values for each element. To test how many iterations would be necessary to reach a stable value for the error, we sampled 60 values from a Gaussian distribution of T_{eff} for one of our stars. The plot of the standard deviation for oxygen abundances is shown in Figure 2.6. The distribution plateaus between 10 - 15 iterations, which agrees with similar tests for other elements. Thus, we select 15 iterations as the basis for the error analysis. We then take the standard deviation of this distribution of abundances and attribute it as the corresponding error for effective temperature or metallicity for each element. We plan to add an additional term for the $\log g$ error in future work. Overall, this methodology allows us to obtain a more complete picture of the systematic uncertainties present in the derived abundance values.

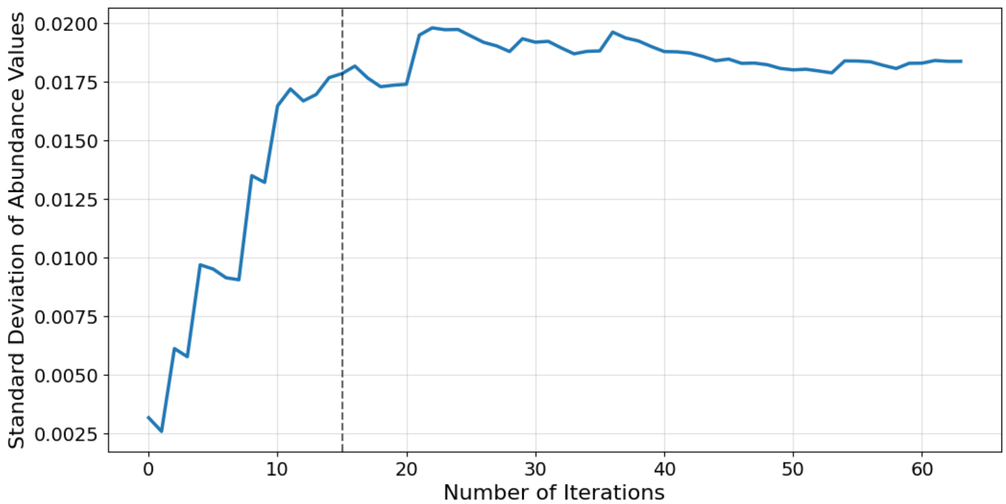

Figure 2.6: Plot visualizing the standard deviation across abundance values when varying input temperatures for abundance analysis of oxygen for Barnard's Star, using the methodology outlined in section 2.4.3. The standard deviation increases steadily until ∼15 iterations, at which point it begins to plateau.

2.5 Summary of the Framework

The steps of the framework are outlined in Figure 2.7. To summarize, we obtain data processed through APERO. Using modified functions from iSpec, the entire spectrum is then shifted into the rest frame using an RV correction and the continuum is globally normalized. A unique linelist is extracted using the VALD catalogue and each line region is manually verified to be free of contamination or blended features. 5 synthetic spectra are generated using MARCS stellar atmosphere models and the Turbospectrum code. These spectra vary across a grid of elemental abundances. The user can then choose to implement the pseudo-continuum normalization or correct for any potential wavelength offsets between the model and the observed data. To regain higher fidelity across the grid of model spectra, the 5 synthetic spectra are interpolated across a grid of 100 evenly spaced abundances ranging from -0.5 to 0.5 dex. The framework will then minimize the χ^2 to determine the elemental abundance for each line region for a particular element. The median of the array of derived abundances across all line regions for an element is then taken as the final abundance value. The standard deviation of this distribution is then as the random error, or σ_{random}. To enable a more detailed analysis of error sources, this procedure is repeated 15 times while varying the assumed temperature and 15 times when varying the metallicity within their respective error ranges. The standard deviation of each of these distributions is then taken as σ_{Teff} and $\sigma_{M/H}$.

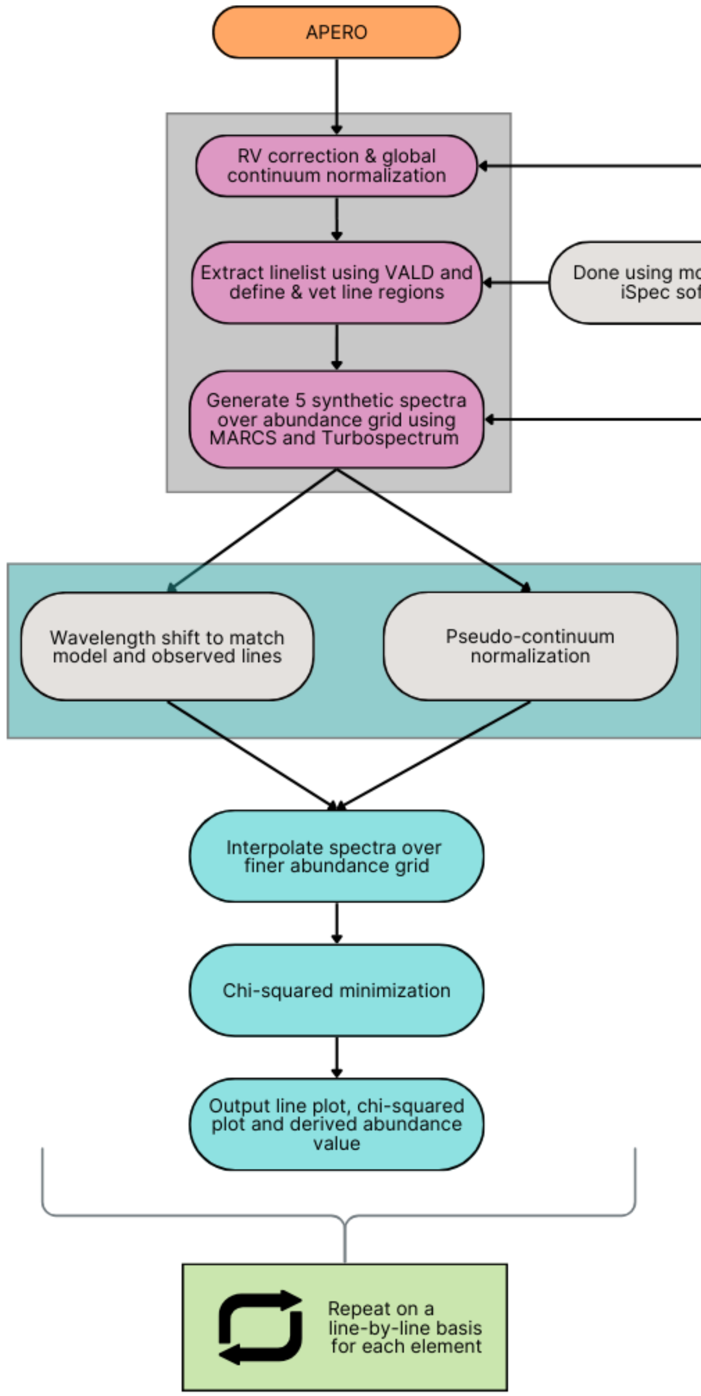

Figure 2.7: A flowchart of the steps of the framework. The items in the gray box are those that use adapted iSpec functions. The items in the blue box are optional steps in the framework.

Chapter 3

Results

3.1 Target Selection

Now that we have shown how the framework operates, we would like to showcase how it can be used in science cases that are both at the forefront of current efforts in exoplanetary science and have previously been studied in the literature. For these purposes, we will apply it to stellar spectra of GJ 9827 and GJ 699. For context, GJ 9827 is a nearby, bright K7-type dwarf star with an effective temperature of $\sim$4200K. As an M4 type star, GJ 699 (commonly known as Barnard's Star) is even smaller and cooler at $\sim$3200K. As such, these temperatures provide a good representation of both early (hotter) and late (cooler) type M dwarfs.

3.1.1 GJ 9827

GJ 9827 was recently studied in great detail by both Passegger et al. (2024) and Piaulet-Ghorayeb et al. (2024), providing us with stellar parameters with small errors and detailed methodology. It is the host star of a multi-planet system of two super-Earths (GJ 9827 b, with radius 1.57 $R_{\oplus}$ and an orbital period of 1.21 days, and GJ 9827 c, with radius 1.24 $R_{\oplus}$ and an orbital period of 3.65 days), and a sub-Neptune (GJ 9827 d, with radius 1.98 $R_{\oplus}$, orbital period of 6.20 days, and mass of 3.02 $M_{\oplus}$) (Passegger et al., 2024). These parameters make GJ 9827 d the smallest known warm sub-Neptune and the smallest exoplanet with a confirmed atmosphere (Piaulet-Ghorayeb et al., 2024). By using data from both HST and JWST, it has also been found that there is a high concentration of water vapour in the atmosphere - potentially making it a "steam world" (Piaulet-Ghorayeb et al., 2024). This makes it an important target for the search for habitability beyond Earth, and for characterising thick, water-rich atmospheres of rocky exoworlds using JWST. There has yet to be any research into the chemical composition of its host star. As explained in Chapter 1, it is important that we be able to place the spectroscopic data from JWST in the context of the system and not assume solar values. While this thesis focuses on M dwarfs, GJ 9827 is a cool K dwarf and so, many of the nuances and difficulties previously mentioned will apply here as well. This star is also cited to be moderately active. According to the measured flare rate, GJ 9827 is qualified as an active K dwarf with a flare rate similar to other active field stars nearby. Our data for GJ 9827 were taken originally by PI James Sikora in program 20BC27. It was observed by SPIRou on 2020-08-31. 19 individual spectra were co-added together to create the spectrum used for this analysis.

3.1.2 GJ 699 (Barnard's Star)

Located only 1.83pc away from the Earth, GJ 699 is one of the closest M dwarfs to Earth and the second closest star system to Earth (Jahandar et al., 2024). It is often used as a benchmark star because of its close proximity to us. There have been numerous previous studies that have derived abundances from its spectra which will provide a good backdrop for our results. It has also become the subject of recent news, as it has been recently confirmed to have an orbiting exoplanet (with a minimum mass of 0.37 ± 0.05 $M_{\oplus}$ and an orbital period of 3.15 days), with three other candidates for low-mass planet companions (González Hernández et al., 2024). While studying Barnard's Star has many benefits, it also proves to be particularly challenging for the retrieval of abundances from the spectra due to its low temperature of $\sim$3200 K. Another one of the many difficulties of modelling it is the wide range of metallicities reported in the literature for the star. These metallicities range from a reported value of -0.86 dex from Marfil et al. (2021) to 0.61 dex from Passegger et al. (2022). For Barnard's Star, the data itself provides a unique opportunity because the spectra have an extremely high signal-to-noise (S/N $\sim$ 1000). This is because the data were observed as part of the SPIRou Legacy Program as one of SPIRou's radial velocity standards (Donati et al., 2020). A total of 846 observations were taken between 2018 and 2023 and co-added to form the spectrum (Jahandar et al., 2024).

3.2 Results from Framework

The framework as outlined in Chapter 2 is run using the data for these two stars. The unique linelist used for each star is made available in Appendices B and C. The radial velocity corrections applied were 114.21 km/s for GJ 9827 and -28.28 km/s for Barnard's Star. These are not the physical radial velocities measured for each of these objects but merely the ones derived from the CCF fitting. The systemic radial velocities are -32.01 km/s for GJ 9827 and -110.46 km/s for GJ 699 (Gaia Collaboration 2018). When generating synthetic spectra for GJ 9827, I adopt the stellar parameters of 4236 ± 12 K, a metallicity of -0.29 ± 0.03 dex, and a surface gravity of 4.7 ± 0.05 dex from Passegger et al. (2024). Similarly, I adopt an effective temperature of 3231 ± 21 K, a metallicity of -0.48 ± 0.04 dex, and a surface gravity of 5.08 ± 0.15 dex from Jahandar et al. (2024) to generate the model spectra for GJ 699.

3.2.1 GJ 9827 Results

The results for GJ 9827 are summarised in Table 3.1, which contains our elemental abundance measurements alongside the derived errors. As a reminder, these derived abundances are the median of the abundances inferred from individual lines for each element. We use the median of all lines for each element and not the mean because of the potentially severe effect of outliers on the values. We calculated the total error by adding the three error values in quadrature. σ_{Random} is the standard deviation of the abundances for each element, and σ_{Teff} and $\sigma_{M/H}$ errors are the systematic errors attributed to variations in temperature and metallicity within their respective errors. As such, elements with only one suitable line do not have a random error attributed to them. We visualize the results from Table 3.1 in Figure 3.1. It is immediately clear that carbon is an outlier. For the sake of visual clarity, we exclude it in Figure 3.2 to gain better detail in the other elements. We also exclude it from

Table 3.1: Derived Abundances per Element for GJ 9827

Element	**N**	**[X/H]**	σ_{Random}	σ_{Teff}	$\sigma_{M/H}$	σ_{Total}
C (CO)	259	**0.004**	0.009	0.338	0.340	**0.479**
O (OH)	47	**-0.253**	0.004	0.003	0.025	**0.026**
Na	10	**-0.251**	0.011	0.001	0.009	**0.014**
Mg	8	**-0.233**	0.041	0.008	0.003	**0.042**
Al	8	**-0.267**	0.035	0.001	0.003	**0.035**
Si	56	**-0.227**	0.024	0.001	0.011	**0.026**
K	6	**-0.225**	0.033	0.003	0.002	**0.033**
Ca	26	**-0.335**	0.028	0.003	0.003	**0.028**
Sc	2	**-0.202**	0.036	0.004	0.002	**0.036**
Ti	65	**-0.276**	0.013	0.004	0.009	**0.016**
Cr	39	**-0.301**	0.027	0.001	0.004	**0.027**
Mn	10	**-0.222**	0.054	0.002	0.016	**0.056**
Fe	180	**-0.305**	0.012	0.007	0.003	**0.014**
[M/H]	-	**-0.258**	-	-	-	**0.040**
[α/H]	-	**-0.265**	-	-	-	**0.044**

our calculation for [M/H] in Table 3.1, which is derived by simply taking the mean of all the elemental abundances. The total error for the derived [M/H] comes from the standard deviation between all the derived abundances. We performed a separate trial where the pseudo-continuum normalization was applied. It was done only once, so only the associated random error is available. The complete table of results of the pseudo-continuum normalized values is in Appendix A. We present the results side-by-side with and without carbon in Figures 3.3 and 3.4.

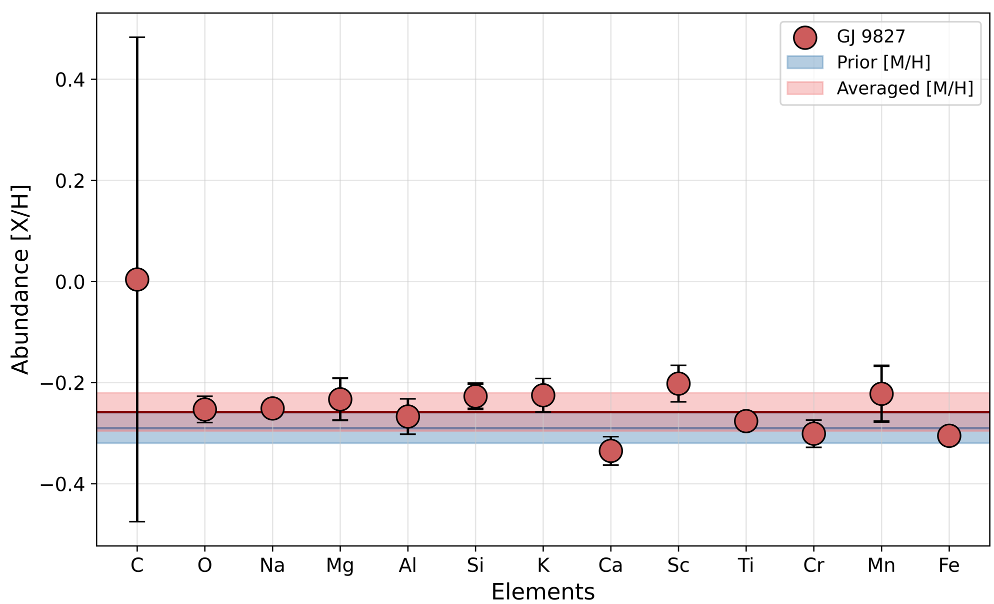

Figure 3.1: Derived Abundances for GJ 9827. The blue ribbon represents the error range around the literature value for metallicity, and the red ribbon is the error range for our averaged metallicity. The averaged metallicity excludes carbon's abundance.

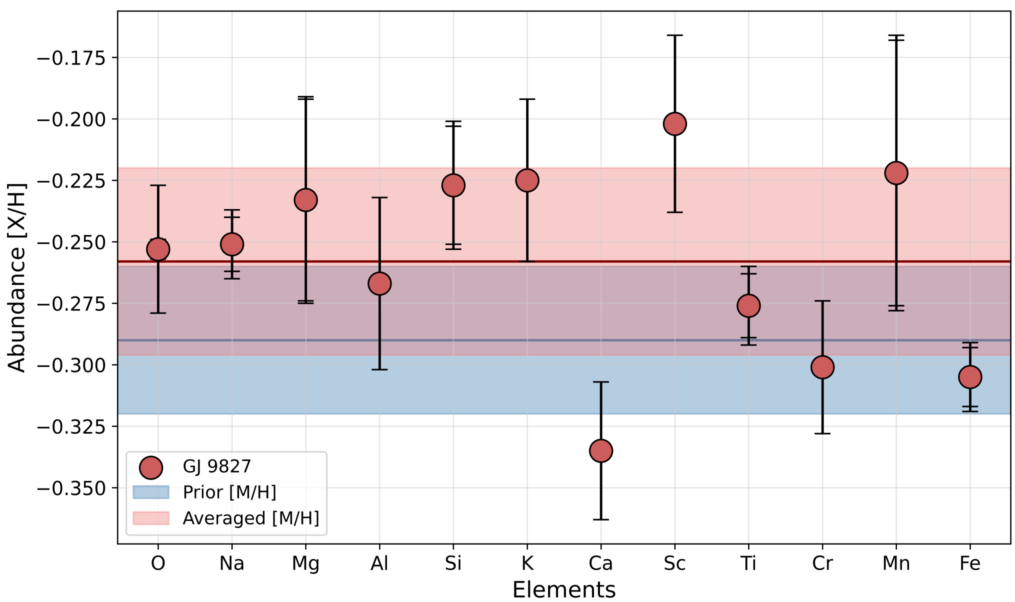

Figure 3.2: Derived Abundances for GJ 9827. Carbon has been excluded to improve the visibility of other elements. Note the dual error bars: the interior error bar represents the random error and the exterior error bar represents the total error.

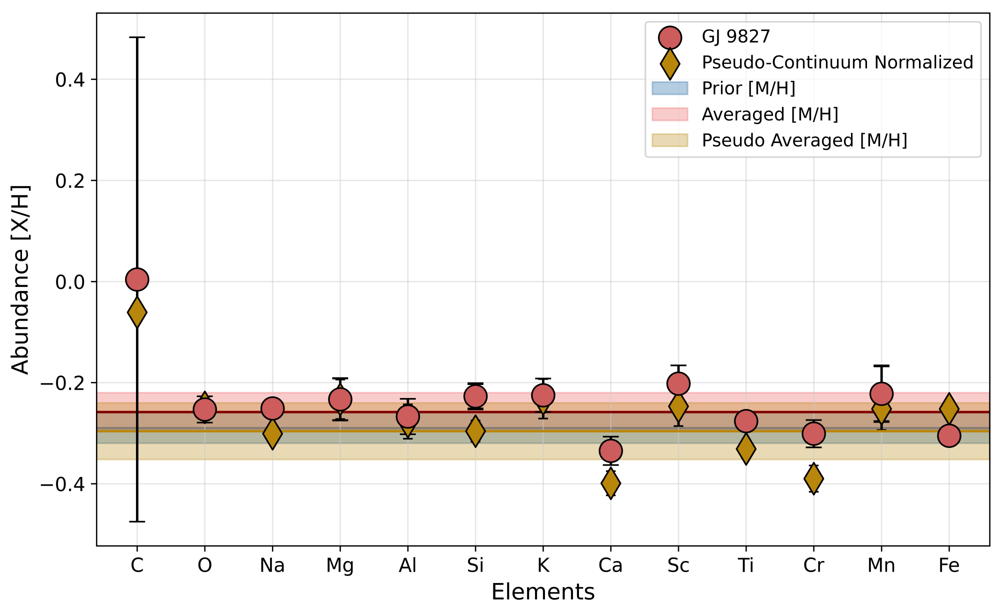

Figure 3.3: Derived Abundances for GJ 9827, alongside the pseudo-continuum normalized values. The yellow ribbon represents the error range around the averaged metallicity from the pseudo-continuum normalized values.

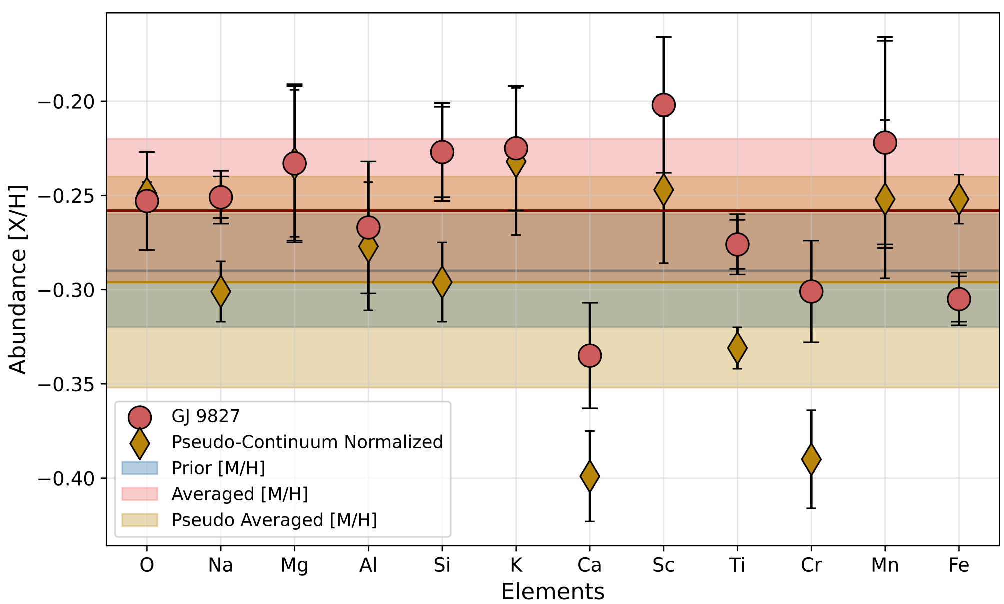

Figure 3.4: Derived Abundances for GJ 9827, alongside the pseudo-continuum normalized values excluding carbon. The interior error bar represents the random error and the exterior error bar represents the total error.

3.2.2 GJ 699 Results

We repeat the framework on Barnard's Star. Because Barnard's Star is such a metal-poor star at [M/H] = -0.48 ± 0.04 dex, many of the lines exist on the edge of our standard abundance grid. To preserve the fidelity of results and retain as many lines as possible, we instead use an abundance grid of [-1.0, -0.75, -0.5, -0.25, 0] dex relative to solar values. Certain elements such as silicon have fewer lines for Barnard's Star than for GJ 9827 as a result of their temperature difference. In a similar fashion, the difference in spectral quality could mean that more lines for other elements are resolved in the Barnard's Star spectra. The reader is reminded of the disparity in literature values for metallicity in Barnard's Star that the error value from Jahandar et al. (2024) may not reflect. To place our derived abundances in context, we also compare to literature values in Figure 3.7.

Table 3.2: Derived Abundances per Element for Barnard's Star

Element	**N**	**[X/H]**	σ_{Random}	σ_{Teff}	$\sigma_{M/H}$	σ_{Total}
C (CO)	56	**-0.267**	0.019	0.226	0.234	**0.326**
O (OH)	60	**-0.122**	0.016	0.002	0.014	**0.021**
Na	3	**-0.652**	0.105	0.010	0.002	**0.105**
Mg	2	**-0.524**	0.040	0.037	0.013	**0.056**
Al	7	**-0.443**	0.037	0.014	0.016	**0.043**
Si	1	**-0.313**	0	0.023	0.054	**0.058**
K	6	**-0.614**	0.100	0.060	0.006	**0.117**
Ca	7	**-0.490**	0.061	0.001	0.013	**0.062**
Sc	2	**-0.489**	0.044	0.013	0.010	**0.047**
Ti	39	**-0.545**	0.033	0.015	0.023	**0.043**
Cr	16	**-0.353**	0.046	0.008	0.016	**0.049**
Mn	6	**-0.495**	0.069	0.005	0.027	**0.074**
Fe	16	**-0.718**	0.075	0.008	0.023	**0.079**
[M/H]	-	**-0.463**	-	-	-	**0.165**
[α/H]	-	**-0.399**	-	-	-	**0.180**

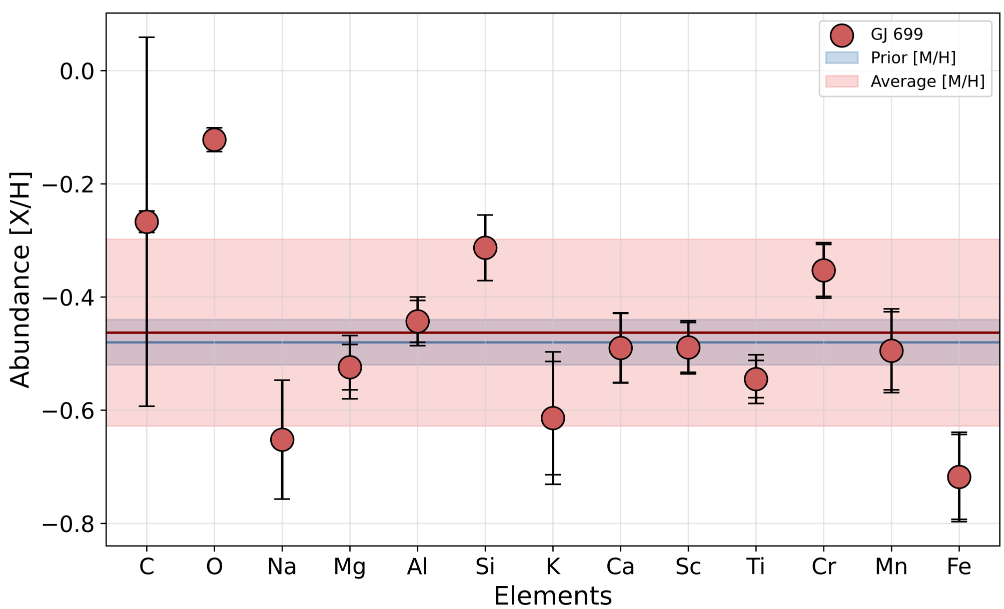

Figure 3.5: Derived Abundances for Barnard's Star. The blue ribbon represents the error range around the literature value for metallicity, and the red ribbon is the error range for our averaged metallicity.

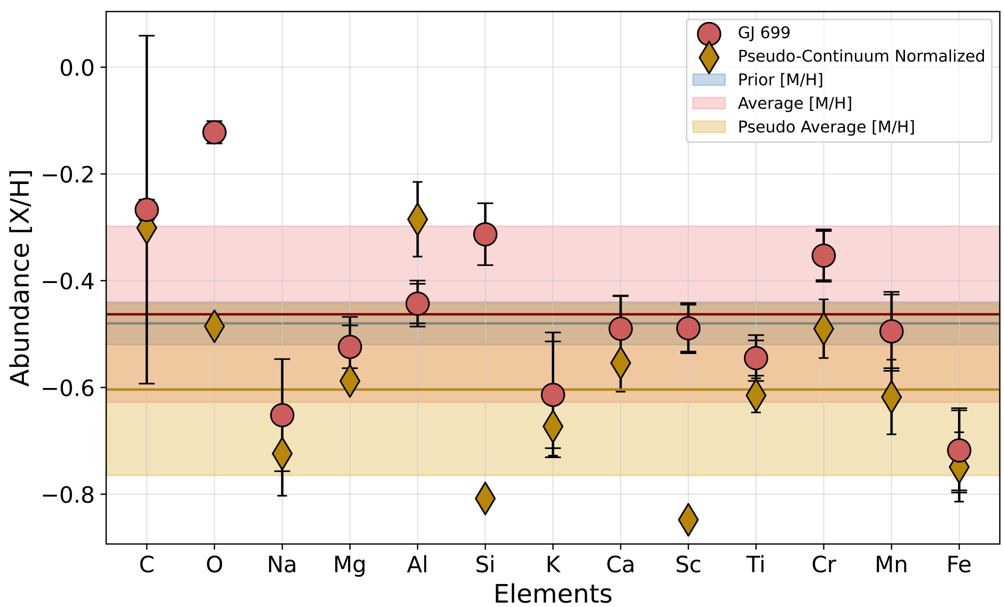

Figure 3.6: Derived Abundances for Barnard's Star, alongside the pseudo-continuum normalized values.

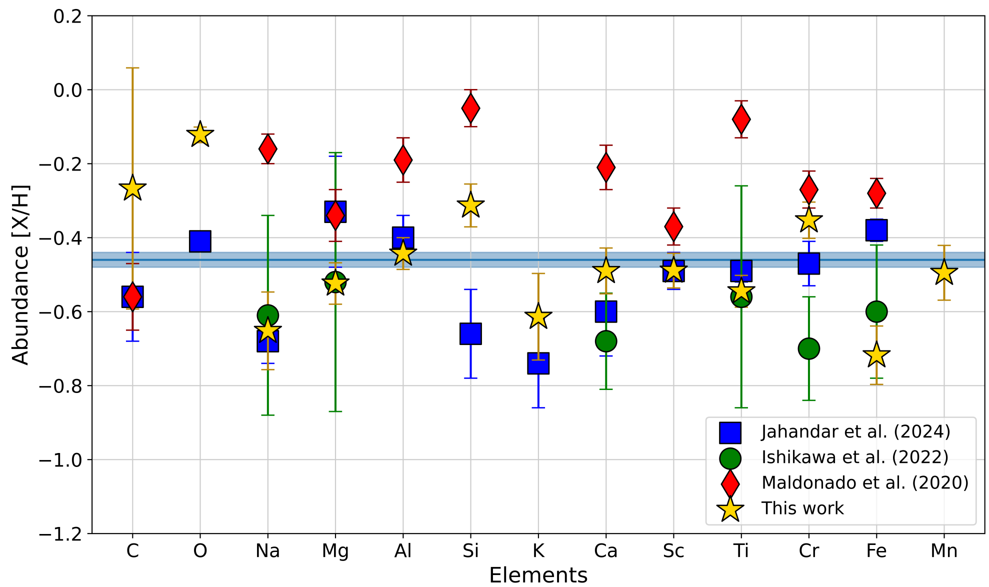

Figure 3.7: Derived Abundances for Barnard's Star, compared to values taken from Ishikawa et al. (2022); Jahandar et al. (2024); Maldonado et al. (2020). The blue line and ribbon represent the metallicity used in Jahandar et al. (2024) of [M/H] = -0.48 ± 0.04 dex

Chapter 4

Discussion and Future Work

4.1 Interpretation of Results

Immediately, we need to acknowledge our values for carbon, especially for GJ 9827, are outliers. That is most certainly the result of something amiss in the framework and not reflective of the physical state of the star. Although carbon is within 1 σ of the metallicity in GJ 699, the large systematic errors from varying effective temperature and metallicity likewise show a large discrepancy for carbon. As previously stated in Section 2.3.1, Hejazi et al. (2023) notes that CO lines are particularly sensitive to changes in microturbulence. Because we adopt our relation to calculate microturbulence from iSpec, this warrants further investigation in order to improve the accuracy of our derived carbon abundances. For GJ 9827, the overall metallicity derived from our abundances when ignoring the carbon outlier is -0.258 $\pm$ 0.038 dex. This is within the error range of the literature value, providing confidence in our results. Looking at the planet-forming refractories, Mg and Si are slightly enhanced whereas Fe is depleted. This agrees with the expected result from Sharma et al. (2024) that planet hosts are enhanced in magnesium and silicon at lower metallicities. Unfortunately, due to the strange behaviour of carbon, a reliable C/O ratio cannot yet be derived nor interpreted from these results. For Barnard's Star, the derived metallicity of -0.463 $\pm$ 0.165 dex is within the error range of the value used in Jahandar et al. (2024). The estimated alpha abundance of -0.399 $\pm$ 0.180 dex is enhanced, as expected for a metal-poor star. For both stars, when considering the overall error contributions, it is clear that random error contributes the most for nearly all elements. Certain elements like titanium and magnesium will show greater sensitivity to changes in the assumed effective temperature and metallicity, as can be seen using the error bars in Figures 3.2 and 3.5.

To comment on the effect that the pseudo-continuum normalization had on the derived abundances in GJ 9827, it seems that for some elements such as magnesium, oxygen, and potassium, it did little to impact the final values. However, for elements such as calcium and chromium, it had a much stronger influence, deviating their abundances outside the error range of the derived [M/H] values. For elements such as sodium, silicon, and scandium, this procedure also had a significant effect on their values but it instead meant that their abundances were closer to the assumed metallicity. Looking at the effect across all 13 elements, applying the pseudo-continuum normalization meant that the final averaged metallicity was overall lower and much closer to the literature metallicity. Comparing to results in Barnard's Star, we see similar trends that the pseudo-continuum normalized values are on average lower for most elements. This is especially exaggerated again for silicon and scandium. We remind the reader that these elements have few lines and so, adjustments made when pseudo-normalizing the continuum will seem especially exaggerated in the final averaged abundance values. This is especially important to consider when considering a key planet-forming element like silicon. When looking at Figure 3.5, the original value for silicon shows it to be enhanced whereas the pseudo-continuum normalized value shows it as severely depleted. This once again highlights the issues that come with analyzing low temperature stars such as M dwarfs. The averaged value for the pseudo-continuum normalized values for Barnard's Star is outside the error range on the metallicity from Jahandar et al. (2024), whereas the original values have a metallicity that falls within it. Overall, it is difficult to comment on the efficacy of the optional pseudo-continuum normalization procedure as we have only applied it to two stars thus far, but we will investigate it further in future works.

Interpreting how our individual elemental abundances compare to those of previous studies for Barnard's Star is more difficult. When looking at Figure 3.7, while there is overall agreement for most elements, there are a few key differences. Some elements where there are few lines, like silicon, diverge greatly whereas we see that values for elements such as magnesium, sodium, and titanium match closely. Some of these differences can be attributed to the differing linelists. We do use the same data as Jahandar et al. (2024) and we note that some of our lines failed their criteria, and vice versa. Sometimes the stringent conditions were relaxed to improve the statistical significance of selected elements. Our linelist also diverges from those listed as "M-dwarf Well-defined Spectral Lines" from Melo et al. (2024) in this temperature range. The most likely culprit for the differences seen in Figure 3.7 is that all of the papers listed use different methodologies and different synthetic models. Jahandar et al. (2024) compares their data to PHOENIX-ACES grids of varying metallicities, but they do not make use of a radiative transfer code to generate new spectra, nor are they varying individual abundances. Maldonado et al. (2020) uses ATLAS9 models with the spectral synthesis code MOOG. They use a novel approach that combines principle component analysis (PCA) and Bayesian regression methods, training their model on optical spectra of M dwarfs orbiting FGK primaries. Maldonado et al. (2020) does mention this technique's tendency to overestimate derived abundances, as can be seen in Figure 3.7. On the other hand, Ishikawa et al. (2022) compared the equivalent widths of their spectral data to equivalent widths of generated synthetic spectra, iteratively modifying the abundances until the lines converged. They did this using high-resolution spectra from the Subaru Telescope, which covers a wavelength range of 0.97 - 1.75 µm. From their results, Ishikawa et al. (2022) noted a consistent underestimation of the abundances. In the end, it is comforting to note that our values are in the right ballpark, especially for a star that is as hard to model as Barnard's Star.

4.2 Conclusion

In conclusion, we performed a brief literature review of the efforts to characterise stellar abundances using spectroscopy. By making use of the planet-star connection, M dwarfs represent a golden opportunity for understanding the planet formation pathways of super-Earths in habitable zones and more easily facilitating the retrieval of masses and radii of their planets. However, their spectra present unique challenges, such as broad molecular bands, which prevent certainty in the accuracy of their elemental abundances. Astronomers are actively working to address and solve these issues. As part of our own efforts to calibrate M dwarf spectra in the future, we developed a framework in Python that uses spectral synthesis methods with the stellar atmosphere model MARCS and the spectral synthesis code Turbospectrum to derive these abundances. By comparing the depths and line profiles along a grid of abundances via a χ^2 minimization routine, we can measure the stellar abundances of individual elements and quantify their uncertainties. This framework was designed to take many nuances into consideration that other papers may take for granted when dealing with M dwarf spectra, such as a normalization procedure for the pseudo-continuum and an extended error analysis. We then presented results from SPIRou data for two cool stars: GJ 699 and GJ 9827. These stars represent important science cases for exoplanet science, as stellar abundances are needed to inform both interior structure modelling and atmospheric characterisation. Even though our methods are similar to those used in the literature currently, we still see numerous pitfalls when doing line-by-line analysis that endanger the certainty we have in these abundances.

It is crucial that we have accurate abundances for M dwarfs and so, this project then motivates the need for an empirical calibration of their spectra. In future work, we will apply this framework to spectra from 24 FGK-M wide binary systems, which will be used as the basis for the generalised empirical calibration of M dwarf abundances measured with SPIRou. Further applications of this framework extend to emerging scientific cases. This framework is designed to allow rapid extraction and analysis of abundances from high-R nIR spectra from SPIRou and other instruments such as IGRINS and NIRPS for future science targets, particularly planet-hosting stars. Four sub-Neptunes orbiting cool stars — TOI-1685, TOI-4517, TOI-1201, and K2-18 — are scheduled to have their atmospheres observed with either JWST or HST. To make the most of this valuable data, we have an observing program to perform follow-up observations of these planetary hosts using SPIRou. This framework will be applied to the set of these planet-hosting stars, enabling the use of more accurate elemental abundances for modelling the planetary atmospheres and solid interiors. In summary, this project represents a crucial step in ensuring the precision and accuracy of future discoveries with direct implications for our understanding of stellar populations and the formation of potentially habitable super-Earths.

Appendix A

Values from Figures 3.1 - 3.6

Table A.1: Mean Abundances and Pseudo-Normalized Values for GJ 9827

Element	**[X/H] (mean)**	**[X/H] (median)**	**Random Error**	**Pseudo [X/H] (mean)**	**Pseudo [X/H] (median)**	**Random Error**
C (CO)	0.033	0.004	0.009	-0.058	-0.061	0.009
O (OH)	-0.258	-0.253	0.004	-0.24	-0.249	0.006
Na	-0.253	-0.251	0.011	-0.305	-0.301	0.016
Mg	-0.286	-0.233	0.041	-0.278	-0.233	0.039
Al	-0.269	-0.267	0.035	-0.279	-0.277	0.034
Si	-0.192	-0.227	0.024	-0.270	-0.296	0.021
K	-0.232	-0.225	0.033	-0.207	-0.232	0.039
Ca	-0.304	-0.335	0.028	-0.368	-0.399	0.024
Sc	-0.202	-0.202	0.036	-0.247	-0.247	0.039
Ti	-0.272	-0.276	0.013	-0.319	-0.331	0.011
Cr	-0.266	-0.301	0.027	-0.342	-0.39	0.026
Mn	-0.158	-0.222	0.054	-0.207	-0.252	0.042
Fe	-0.265	-0.305	0.012	-0.308	-0.345	0.013
[M/H]	-0.225	-0.238	0.082	-0.264	-0.278	0.086

Table A.2: Mean Abundances and Pseudo-Normalized Values for Barnard's Star

Element	**[X/H] (mean)**	**[X/H] (median)**	**Random Error**	**Pseudo [X/H] (mean)**	**Pseudo [X/H] (median)**	**Random Error**
C (CO)	-0.271	-0.267	0.019	-0.456	-0.414	0.021
O (OH)	-0.160	-0.122	0.016	-0.365	-0.485	0.018
Na	-0.674	-0.652	0.105	-0.689	-0.724	0.079
Mg	-0.524	-0.524	0.04	-0.588	-0.588	0
Al	-0.408	-0.443	0.037	-0.319	-0.285	0.07
Si	-0.313	-0.313	0	-0.808	-0.808	0
K	-0.558	-0.614	0.100	-0.72	-0.673	0.055
Ca	-0.542	-0.49	0.061	-0.601	-0.554	0.054
Sc	-0.489	-0.489	0.044	-0.848	-0.848	0
Ti	-0.522	-0.545	0.033	-0.63	-0.615	0.032
Cr	-0.39	-0.353	0.046	-0.486	-0.490	0.055
Mn	-0.549	-0.495	0.069	-0.699	-0.618	0.070
Fe	-0.633	-0.718	0.075	-0.714	-0.749	0.065
[M/H]	-0.466	-0.463	0.165	-0.609	-0.604	0.161

Appendix B

Linelist used in the Analysis of GJ 9827

Table B.1: Linelist of Spectral Lines used in Analysis of GJ 9827

Peak Wavelength (nm)	**Base Wavelength (nm)**	**Top Wavelength (nm)**	**Element**
966.72870	966.69662	966.78159	Cr 1
967.05441	967.01150	967.10647	Cr 1
967.55542	967.45133	967.69124	Ti 1
970.19287	970.15031	970.22028	Ca 1
970.56731	970.47018	970.65511	Ti 1
971.89668	971.84966	971.96461	Ti 1
972.84153	972.73932	972.90925	Ti 1
973.03220	973.00422	973.06419	Cr 1
973.85674	973.80891	973.89888	Fe 1
974.36117	974.26374	974.43367	Ti 1
974.69214	974.63360	974.71856	Ti 1
976.33855	976.28297	976.36294	Fe 1
976.39036	976.36294	976.42291	Fe 1
980.03074	979.96656	980.06153	Fe 1
981.15102	981.10113	981.18610	Fe 1
986.81642	986.76897	986.84894	Fe 1

Peak Wavelength (nm)	Base Wavelength (nm)	Top Wavelength (nm)	Element
988.90269	988.84818	988.95814	Fe 1
990.09160	990.04272	990.10770	Cr 1
992.73656	992.70171	992.81167	Ti 1
994.13932	994.11117	994.16116	Ti 1
994.90665	994.87089	994.95085	Cr 1
999.79519	999.74403	999.86398	Ti 1
1000.30917	1000.27383	1000.34380	Ti 1
1001.17503	1001.12850	1001.19847	Ti 1
1003.44931	1003.38764	1003.51759	Ti 1
1004.88324	1004.83709	1004.92205	Ti 1
1005.99153	1005.96666	1006.03663	Ti 1
1006.50446	1006.47146	1006.56643	Fe 1
1006.65155	1006.62141	1006.71637	Ti 1
1008.03598	1008.00588	1008.07585	Cr 1
1008.13926	1008.11584	1008.17581	Fe 1
1008.96708	1008.92553	1009.01050	Cr 1
1011.40552	1011.34961	1011.43957	Fe 1
1012.09004	1012.06433	1012.14430	Ti 1
1014.55630	1014.46842	1014.60337	Fe 1
1015.51674	1015.45304	1015.55300	Fe 1
1016.74754	1016.68257	1016.79753	Fe 1
1019.51116	1019.47151	1019.60146	Fe 1
1021.63167	1021.51573	1021.70066	Fe 1
1021.83940	1021.79063	1021.88559	Fe 1
1026.52125	1026.48384	1026.56881	Fe 1
1028.89457	1028.86293	1028.92291	Si 1
1034.08891	1034.03096	1034.13092	Fe 1
1034.38196	1034.23089	1034.50578	Ca 1
1037.12582	1037.04981	1037.21475	Si 1
1037.90028	1037.87950	1037.94947	Fe 1
1039.58015	1039.52887	1039.62883	Fe 1
1039.68130	1039.62883	1039.79377	Ti 1
1042.30347	1042.25783	1042.34279	Fe 1
1042.37474	1042.34279	1042.41777	Fe 1
1046.00603	1045.96641	1046.06638	Ti 1

Peak Wavelength (nm)	Base Wavelength (nm)	Top Wavelength (nm)	Element
1046.96609	1046.90106	1047.05600	Fe 1
1048.62552	1048.56043	1048.68038	Cr 1
1049.61242	1049.51506	1049.66500	Ti 1
1051.00146	1050.95951	1051.03948	Cr 1
1053.22395	1053.15368	1053.27363	Fe 1
1055.29696	1055.25787	1055.32785	Ti 1
1055.83706	1055.77768	1055.89263	Ca 1
1057.71458	1057.68195	1057.75692	Fe 1
1058.46505	1058.40168	1058.49164	Ti 1
1060.34310	1060.20599	1060.39592	Si 1
1060.77311	1060.70580	1060.86574	Ti 1
1061.67245	1061.64044	1061.70542	Fe 1
1064.76446	1064.71927	1064.79924	Cr 1
1066.09652	1065.99378	1066.12873	Si 1
1066.16287	1066.12873	1066.24369	Ti 1
1066.75180	1066.69851	1066.80847	Cr 1
1067.21440	1067.14334	1067.24830	Cr 1
1067.70589	1067.60317	1067.75811	Ti 1
1068.96893	1068.87269	1069.02763	Si 1
1069.42357	1069.34750	1069.51244	Si 1
1072.52002	1072.49131	1072.56628	Fe 1
1072.63975	1072.58127	1072.69123	Ti 1
1072.73984	1072.69123	1072.82618	Si 1
1073.28728	1073.20104	1073.34098	Ti 1
1074.64376	1074.60050	1074.68547	Na 1
1074.93766	1074.83041	1075.07032	Si 1
1075.30071	1075.26025	1075.36521	Fe 1
1078.06912	1078.03419	1078.09917	Fe 1
1078.30522	1078.23912	1078.36407	Fe 1
1078.68525	1078.58398	1078.79890	Si 1
1080.13615	1080.09841	1080.18837	Cr 1
1081.10817	1080.99806	1081.28296	Mg 1
1081.69132	1081.65282	1081.75778	Cr 1
1081.82740	1081.78776	1081.87273	Fe 1
1082.16612	1082.13263	1082.20760	Cr 1

Peak Wavelength (nm)	Base Wavelength (nm)	Top Wavelength (nm)	Element
1083.34084	1083.29219	1083.37716	Ca 1
1083.48619	1083.41714	1083.61707	Na 1
1084.38324	1084.29181	1084.42676	Si 1
1086.35223	1086.26106	1086.41600	Fe 1
1086.95348	1086.82584	1087.10574	Si 1
1087.29332	1087.25568	1087.37064	Al 1
1088.17610	1088.13534	1088.21032	Fe 1
1088.53227	1088.46522	1088.61516	Si 1
1089.16777	1089.06999	1089.21493	Al 1
1089.62984	1089.57979	1089.69475	Fe 1
1090.57091	1090.45946	1090.61440	Cr 1
1092.99261	1092.91352	1093.03848	Cr 1
1095.72511	1095.62249	1095.80742	Mg 1
1097.93064	1097.87163	1097.96660	Si 1
1098.20655	1098.14653	1098.24149	Si 1
1098.45338	1098.41143	1098.50639	Si 1
1101.32230	1101.28533	1101.34531	Fe 1
1101.55244	1101.49026	1101.60521	Cr 1
1101.79867	1101.73016	1101.87511	Si 1
1101.98233	1101.96507	1102.03505	K 1
1102.27101	1102.20998	1102.29495	K 1
1102.68359	1102.65481	1102.71979	Fe 1
1104.45736	1104.42414	1104.51910	Cr 1
1111.98028	1111.89129	1112.02124	Fe 1
1113.00397	1112.92590	1113.04585	Si 1
1114.92630	1114.85016	1114.96512	Fe 1
1115.69533	1115.62487	1115.80480	Cr 1
1118.75953	1118.69370	1118.82365	Si 1
1125.48823	1125.38115	1125.56608	Al 1
1128.98185	1128.91480	1129.06975	Si 1
1129.88600	1129.76448	1129.94941	Fe 1
1131.07338	1131.02400	1131.13396	Cr 1
1133.19191	1133.13820	1133.25315	Cr 1
1133.91600	1133.86792	1133.99287	Cr 1
1135.59693	1135.54728	1135.64224	Fe 1

Peak Wavelength (nm)	Base Wavelength (nm)	Top Wavelength (nm)	Element
1137.40811	1137.36159	1137.47654	Fe 1
1137.93348	1137.89638	1137.97635	Cr 1
1139.07512	1139.02095	1139.13591	Cr 1
1139.80608	1139.73068	1139.87563	Cr 1
1142.23219	1142.12477	1142.33469	Fe 1
1147.30206	1147.23782	1147.37277	Cr 1
1148.58429	1148.54233	1148.61730	Si 1
1159.14435	1159.08331	1159.19327	Si 1
1159.35907	1159.26324	1159.42818	Fe 1
1159.45192	1159.42818	1159.50315	Fe 1
1160.75738	1160.62272	1160.86263	Fe 1
1161.05591	1160.96259	1161.15252	Cr 1
1163.82631	1163.66156	1163.99144	Fe 1
1176.75476	1176.67660	1176.81155	Ca 1
1176.96382	1176.88153	1177.03147	K 1
1177.28431	1177.17142	1177.41132	K 1
1178.05555	1177.98111	1178.10106	Ti 1
1178.32631	1178.22601	1178.43094	Fe 1
1179.29117	1179.17982	1179.34929	Ca 1
1179.71825	1179.66547	1179.76043	Ti 1
1182.81660	1182.51438	1183.22911	Mg 1
1188.28463	1188.09725	1188.35715	Fe 1
1188.40818	1188.35715	1188.56707	Fe 1
1189.04620	1188.97192	1189.11686	Fe 1
1194.95448	1194.87967	1195.07459	Ti 1
1195.59303	1195.51443	1195.70435	Ca 1
1197.30426	1197.15880	1197.35372	Fe 1
1198.42031	1198.25838	1198.61824	Si 1
1199.15548	1198.99810	1199.30798	Si 1
1200.54089	1200.49253	1200.59749	Fe 1
1203.14996	1202.97658	1203.25148	Si 1
1203.97927	1203.91622	1204.06117	Mg 1
1205.30610	1205.23572	1205.35068	Fe 1
1210.35327	1210.19383	1210.49372	Si 1
1210.58225	1210.49372	1210.65366	Ca 1

Peak Wavelength (nm)	Base Wavelength (nm)	Top Wavelength (nm)	Element
1211.94732	1211.89318	1212.00814	Fe 1
1219.01105	1218.94050	1219.07545	Fe 1
1222.71296	1222.62410	1222.79403	Fe 1
1227.06856	1226.91746	1227.17236	Si 1
1232.00031	1231.96054	1232.09049	Na 1
1234.04783	1234.00976	1234.08473	Fe 1
1234.29306	1234.25466	1234.34963	Fe 1
1239.01393	1238.93788	1239.06783	Si 1
1239.58134	1239.49267	1239.65760	Si 1
1243.22384	1243.13628	1243.27123	K 1
1252.20782	1252.07287	1252.31278	K 1
1253.28334	1253.22244	1253.34239	Cr 1
1255.69983	1255.61652	1255.78646	Fe 1
1260.02769	1259.95987	1260.07982	Ti 1
1261.59363	1261.53427	1261.65422	Fe 1
1263.87035	1263.73843	1263.94335	Fe 1
1264.87344	1264.77803	1264.93797	Fe 1
1267.10963	1267.05217	1267.20711	Ti 1
1267.91291	1267.81188	1267.97181	Na 1
1273.83881	1273.74461	1273.90955	Ti 1
1274.49120	1274.41936	1274.55930	Ti 1
1280.71596	1280.66698	1280.76194	Fe 1
1281.14844	1281.10181	1281.20177	Ti 1
1281.60261	1281.51165	1281.66160	Ca 1
1282.16739	1282.08644	1282.26137	Ti 1
1282.38380	1282.29636	1282.44630	Ca 1
1282.48574	1282.44630	1282.55126	Fe 1
1282.70301	1282.63123	1282.76118	Ca 1
1283.14364	1283.08606	1283.22600	Ti 1
1284.70335	1284.55050	1284.76542	Ti 1
1287.97659	1287.91422	1288.07415	Fe 1
1289.97611	1289.81349	1290.07839	Mn 1
1290.90712	1290.84810	1290.95806	Ca 1
1291.00903	1290.95806	1291.09300	Cr 1
1291.99020	1291.94268	1292.08762	Ti 1

Peak Wavelength (nm)	Base Wavelength (nm)	Top Wavelength (nm)	Element
1293.70202	1293.62704	1293.80697	Cr 1
1295.08990	1295.02650	1295.13146	Ti 1
1297.59233	1297.49057	1297.69049	Mn 1
1298.75776	1298.69511	1298.80506	Ti 1
1300.13711	1300.08958	1300.18454	Ca 1
1300.66822	1300.60938	1300.78431	Fe 1
1301.18867	1301.14917	1301.26913	Ti 1
1303.35471	1303.27836	1303.41331	Ca 1
1305.78751	1305.73742	1305.84238	Ca 1
1308.64171	1308.56635	1308.72129	Ca 1
1310.20394	1310.06577	1310.29069	Si 1
1313.49285	1313.41450	1313.57444	Ca 1
1317.68163	1317.58291	1317.77784	Si 1
1320.11472	1320.06196	1320.17192	Cr 1
1321.70206	1321.62137	1321.80130	Cr 1
1326.06991	1326.01470	1326.12465	Fe 1
1328.15070	1328.04392	1328.23885	Mn 1
1329.38106	1329.27345	1329.51336	Mn 1
1330.90736	1330.85285	1331.00779	Si 1
1331.89948	1331.82748	1332.02241	Mn 1
1332.55892	1332.49723	1332.70215	Si 1
1335.21427	1335.09624	1335.34114	Fe 1
1338.44556	1338.36999	1338.49994	Fe 1
1338.93704	1338.81482	1339.03473	Fe 1
1339.20568	1339.11970	1339.32462	Fe 1
1341.56965	1341.50879	1341.69372	Mn 1
1386.41981	1386.26174	1386.58661	Mn 1
1407.33170	1407.20376	1407.39868	Si 1
1422.44871	1422.36798	1422.56290	Si 1
1425.94617	1425.90163	1426.09656	Ca 1
1428.50238	1428.35570	1428.64559	Fe 1
1429.23055	1429.10541	1429.33532	Fe 1
1430.86856	1430.78977	1430.91972	Fe 1
1434.84626	1434.68329	1434.91820	Cr 1
1440.05243	1439.90630	1440.30115	Fe 1

Peak Wavelength (nm)	Base Wavelength (nm)	Top Wavelength (nm)	Element
1443.43289	1443.38497	1443.47993	Ca 1
1443.75576	1443.70485	1443.81481	Fe 1
1444.22292	1444.09470	1444.31961	Fe 1
1451.21621	1450.98207	1451.33194	Fe 1
1455.49957	1455.39040	1455.69528	Fe 1
1456.58942	1456.49497	1456.73488	Fe 1
1465.10173	1465.00673	1465.15667	Fe 1
1465.28588	1465.21165	1465.38659	Fe 1
1470.29231	1470.13977	1470.37968	Fe 1
1471.96038	1471.77415	1472.10902	Fe 1
1472.23482	1472.15901	1472.31395	Fe 1
1473.75929	1473.67343	1473.81337	Fe 1
1474.53756	1474.48812	1474.60307	Fe 1
1474.97787	1474.87797	1475.05290	Fe 1
1476.74784	1476.68228	1476.77725	Na 1
1477.97346	1477.87183	1478.10174	Na 1
1481.47238	1481.41548	1481.62540	Fe 1
1482.63705	1482.51006	1482.79995	Fe 1
1484.56853	1484.50930	1484.62425	Cr 1
1484.96772	1484.87416	1485.03410	Ti 1
1495.61140	1495.50011	1495.74502	Fe 1
1497.87419	1497.76925	1497.92918	Cr 1
1498.87337	1498.78386	1499.00877	Fe 1
1502.49782	1502.32751	1503.13720	Mg 1
1504.02329	1503.55204	1504.39672	Mg 1
1504.76910	1504.51168	1504.99649	Mg 1
1507.72663	1507.66048	1507.79543	Fe 1
1509.46739	1509.36483	1509.53976	Fe 1
1511.73163	1511.64896	1511.78890	Ti 1
1512.23463	1512.12877	1512.35869	Fe 1
1514.57618	1514.49287	1514.63782	OH
1514.79364	1514.73278	1514.85773	OH
1515.91120	1515.76739	1516.03728	Mn 1
1516.30477	1516.14724	1516.39215	K 1
1516.83830	1516.69703	1517.00192	K 1

Peak Wavelength (nm)	Base Wavelength (nm)	Top Wavelength (nm)	Element
1518.67062	1518.63130	1518.73126	Ti 1
1518.80932	1518.73126	1518.92119	Ti 1
1519.44782	1519.37101	1519.54095	Fe 1
1520.74763	1520.57056	1520.89543	Fe 1
1521.76564	1521.63515	1521.85007	Mn 1
1524.49270	1524.37411	1524.63401	Fe 1
1526.23753	1526.12844	1526.36835	Mn 1
1527.85152	1527.78781	1527.95274	OH
1528.10445	1528.03771	1528.18765	OH
1529.45309	1529.18727	1529.65709	Fe 1
1534.37229	1534.30032	1534.44027	Fe 1
1537.68082	1537.60906	1537.74901	Si 1
1538.10576	1537.96893	1538.14386	Ti 1
1539.46347	1539.27843	1539.51834	Fe 1
1539.56302	1539.51834	1539.68327	Fe 1
1540.91649	1540.79285	1540.98778	OH
1541.94375	1541.87244	1542.00239	OH
1550.12634	1550.01933	1550.29423	Fe 1
1553.16955	1553.09816	1553.27309	Fe 1
1553.42187	1553.32308	1553.49801	Fe 1
1554.37559	1554.29770	1554.50762	Ti 1
1556.02420	1555.96207	1556.15700	OH
1556.87700	1556.82174	1556.93670	OH
1557.20727	1557.14662	1557.26657	OH
1559.14791	1558.93594	1559.27081	Fe 1
1560.28450	1560.19546	1560.33540	Ti 1
1560.42203	1560.33540	1560.52533	Fe 1
1561.11168	1561.03514	1561.19508	Fe 1
1562.16075	1561.88481	1562.37463	Fe 1
1563.19058	1563.01438	1563.40923	Fe 1
1564.84373	1564.67875	1565.01362	Fe 1
1566.19533	1565.97326	1566.40309	Fe 1
1568.00236	1567.89252	1568.09745	Cr 1
1569.89692	1569.85178	1569.98173	Ti 1
1571.55703	1571.46116	1571.65609	Ti 1

Peak Wavelength (nm)	Base Wavelength (nm)	Top Wavelength (nm)	Element
1571.71182	1571.65609	1571.78104	OH
1571.96860	1571.86601	1572.02595	OH
1572.35408	1572.18089	1572.48078	Fe 1
1573.04269	1572.99558	1573.10554	OH
1574.07052	1573.77028	1574.16014	Mg 1
1574.89487	1574.57998	1575.21473	Mg 1
1576.58087	1576.23435	1576.80413	Mg 1
1577.40213	1577.28395	1577.49886	Fe 1
1577.68367	1577.60382	1577.80375	OH
1577.87709	1577.80375	1577.95869	OH
1579.85515	1579.72302	1579.95793	Fe 1
1581.81024	1581.69227	1582.00715	Fe 1
1582.17425	1582.10211	1582.19707	Fe 1
1582.27572	1582.19707	1582.38700	Fe 1
1583.36171	1583.24167	1583.43660	Si 1
1583.51471	1583.43660	1583.63652	Fe 1
1583.67901	1583.63652	1583.71649	Ti 1
1583.76034	1583.71649	1583.90642	Fe 1
1586.84681	1586.72535	1587.04023	Fe 1
1587.94878	1587.88491	1588.07983	Mg 1
1588.83702	1588.66961	1589.07445	Si 1
1589.21788	1589.15942	1589.29937	OH
1589.77177	1589.68922	1589.88414	OH
1590.59740	1590.50391	1590.76881	Fe 1
1591.04142	1590.95873	1591.08369	OH
1596.48245	1596.38667	1596.60158	Fe 1
1597.12078	1597.06141	1597.18136	Fe 1
1598.07069	1597.95607	1598.28094	Fe 1
1600.68192	1600.57507	1600.76000	Fe 1
1600.95363	1600.85996	1601.07488	Fe 1
1601.53419	1601.44474	1601.58968	Cr 1
1603.68745	1603.50895	1603.73387	OH
1603.85197	1603.80884	1603.93379	OH
1604.27078	1604.17370	1604.40361	Fe 1
1605.27564	1605.21330	1605.34325	OH

Peak Wavelength (nm)	Base Wavelength (nm)	Top Wavelength (nm)	Element
1605.54546	1605.49320	1605.63814	OH
1605.99121	1605.88305	1606.12296	Si 1
1606.16973	1606.12296	1606.29289	OH
1606.50405	1606.41285	1606.63276	OH
1606.95204	1606.83768	1607.00262	OH
1607.41471	1607.33249	1607.47244	OH
1610.23602	1610.09644	1610.45131	Fe 1
1611.59611	1611.54089	1611.75081	Fe 1
1612.59086	1612.48053	1612.77042	Fe 1
1613.67931	1613.62510	1613.86001	Ca 1
1615.07129	1614.99457	1615.19450	Ca 1
1615.31686	1615.19450	1615.40942	Fe 1
1615.52506	1615.40942	1615.58435	Ca 1
1615.72808	1615.58435	1615.89423	Ca 1
1616.37292	1616.24410	1616.41903	Si 1
1616.50058	1616.41903	1616.68393	Fe 1
1617.49620	1617.36367	1617.64856	Fe 1
1618.08956	1618.03342	1618.19336	Fe 1
1619.01506	1618.95806	1619.07802	OH
1619.21175	1619.14799	1619.27294	OH
1619.50378	1619.35291	1619.57283	Fe 1
1619.70033	1619.57283	1619.77775	Ca 1
1620.40993	1620.30755	1620.55745	Ca 1
1621.35519	1621.24219	1621.47211	Fe 1
1621.56758	1621.47211	1621.63205	Si 1
1623.59412	1623.49134	1623.70626	Fe 1
1624.17877	1624.00114	1624.27104	Si 1
1624.64370	1624.60091	1624.73586	Fe 1
1625.49947	1625.43060	1625.55055	OH
1626.01419	1625.94540	1626.07535	OH
1628.47409	1628.39447	1628.58939	Fe 1
1629.27770	1629.14918	1629.33911	Fe 1
1631.63261	1631.38333	1631.80817	Fe 1
1632.43860	1632.23800	1632.56288	Fe 1
1633.05925	1632.98772	1633.10267	Ti 1

Peak Wavelength (nm)	Base Wavelength (nm)	Top Wavelength (nm)	Element
1633.14713	1633.10267	1633.23762	Fe 1
1635.22028	1635.12690	1635.28684	OH
1636.45858	1636.39142	1636.57635	OH
1636.81285	1636.74629	1636.94121	OH
1637.74653	1637.66594	1637.84087	Fe 1
1638.01346	1637.84087	1638.05579	Si 1
1638.15604	1638.05579	1638.33068	Si 1
1639.43309	1639.31031	1639.54022	Fe 1
1639.63961	1639.60020	1639.67517	Fe 1
1639.81642	1639.71515	1639.95506	Fe 1
1640.15527	1640.05503	1640.25495	Ti 1
1640.46438	1640.38990	1640.54984	Fe 1
1640.78639	1640.68978	1640.88471	Fe 1
1643.48970	1643.42874	1643.56369	Si 1
1644.03920	1643.98353	1644.12847	Fe 1
1644.47730	1644.41836	1644.64328	Fe 1
1646.69012	1646.57754	1646.81245	Fe 1
1648.66289	1648.49681	1648.97163	Fe 1
1650.62557	1650.50604	1650.74095	Fe 1
1651.72353	1651.56064	1651.85553	Fe 1
1652.20332	1652.06545	1652.28536	Fe 1
1652.35035	1652.28536	1652.39032	OH
1652.44558	1652.39032	1652.57026	Fe 1
1652.62365	1652.57026	1652.75519	OH
1653.45786	1653.37495	1653.51490	OH
1653.85784	1653.66984	1654.01471	OH
1654.13436	1654.01471	1654.30959	Fe 1
1656.17271	1656.03893	1656.34882	Fe 1
1663.51804	1663.45611	1663.60105	Ti 1
1664.58345	1664.49071	1664.76561	Fe 1
1666.54411	1666.35000	1666.65489	Fe 1
1668.07497	1667.95439	1668.30926	Si 1
1670.43532	1670.34348	1670.52341	OH
1671.43529	1671.31811	1671.49304	OH
1671.89120	1671.55302	1672.12780	Al 1

Peak Wavelength (nm)	Base Wavelength (nm)	Top Wavelength (nm)	Element
1675.05181	1674.95173	1675.14665	Al 1
1676.33134	1676.20125	1676.49614	Al 1
1682.81114	1682.73376	1682.89870	Si 1
1689.51816	1689.43121	1689.63613	OH
1690.42699	1690.32587	1690.49081	OH
1690.92775	1690.86566	1690.99561	OH
1696.98850	1696.83839	1697.16826	Fe 1
1700.53786	1700.47200	1700.60195	Fe 1
1701.10167	1700.97181	1701.22671	Fe 1
1709.63810	1709.50856	1709.68849	OH
1710.86089	1710.74309	1710.98799	Mg 1
1716.10708	1715.99109	1716.24099	Fe 1
1720.42523	1720.28445	1720.49937	Fe 1
1730.22595	1730.09072	1730.35062	Fe 1
1730.84291	1730.72547	1730.89541	OH
1731.29781	1731.22028	1731.40521	OH
1731.61087	1731.52517	1731.67011	OH
1732.22315	1732.07496	1732.31987	OH
1732.73164	1732.60476	1732.97961	Si 1
1738.84282	1738.74742	1738.90236	Ti 1
1748.06691	1747.97890	1748.18882	Fe 1
1753.88861	1753.79168	1754.01660	OH
1760.86061	1760.77402	1760.96395	Fe 1
1761.70308	1761.55373	1761.83862	Si 1
1768.38740	1768.29116	1768.49108	Fe 1
1769.58955	1769.43072	1769.64064	Fe 1
1770.66655	1770.49532	1770.75522	Fe 1
1772.11936	1771.99974	1772.33462	Fe 1
1772.80979	1772.61951	1772.96938	Fe 1
1777.10790	1776.99284	1777.21276	Fe 1
1782.25526	1782.14588	1782.37579	Fe 1
1783.60740	1783.47537	1783.74527	Fe 1
1784.59543	1784.44500	1784.74489	Fe 1
1793.00742	1792.80182	1793.13169	Fe 1
1793.77909	1793.57652	1793.98137	Fe 1

Peak Wavelength (nm)	Base Wavelength (nm)	Top Wavelength (nm)	Element
1795.60127	1795.40583	1795.67072	Fe 1
1798.23083	1798.13978	1798.33471	Fe 1
1807.36919	1807.27130	1807.44624	Fe 1
1809.63194	1809.42548	1809.77535	Fe 1
1812.79951	1812.72423	1812.90416	Fe 1
1818.99265	1818.83690	1819.12179	Fe 1
1844.17934	1844.04229	1844.33218	Fe 1
1879.09913	1879.06395	1879.12392	Fe 1
1885.66477	1885.50649	1885.92633	Fe 1
1892.54794	1892.36888	1892.66376	Ca 1
1911.36786	1911.22169	1911.46660	Fe 1
1935.46245	1935.37749	1935.52243	Fe 1
1938.60091	1938.33136	1938.86116	Si 1
1942.52063	1942.33983	1942.63972	Mg 1
1943.29566	1943.07455	1943.43442	Si 1
1963.52252	1963.24187	1963.71169	Fe 1
1972.24802	1971.99353	1972.52333	Si 1
1981.49681	1981.33497	1981.74982	Ca 1
1985.30145	1985.01357	1985.65333	Ca 1
1991.71332	1991.51609	1991.90595	Ca 1
1992.32952	1992.24082	1992.45074	Fe 1
1992.89014	1992.70564	1993.03052	Si 1
1993.36310	1993.08550	1993.64528	Ca 1
1996.17382	1995.91942	1996.32426	Ca 1
1997.00443	1996.94902	1997.05898	Fe 1
2023.89072	2023.71882	2023.93874	Cr 1
2029.64043	2029.48662	2029.74653	Si 1
2034.97348	2034.88457	2035.03451	Fe 1
2037.84517	2037.80845	2037.94340	Si 1
2069.83801	2069.65632	2070.02618	Fe 1
2071.68539	2071.53560	2071.78551	Fe 1
2091.71083	2091.56297	2091.85786	Si 1
2096.23990	2096.17621	2096.39613	Ca 1
2109.29741	2109.10628	2109.46615	Al 1
2116.36919	2115.93868	2116.60843	Al 1

Peak Wavelength (nm)	Base Wavelength (nm)	Top Wavelength (nm)	Element
2123.84284	2123.69572	2123.99561	Fe 1
2177.96453	2177.81010	2178.04501	Si 1
2178.29361	2178.13498	2178.42987	Ti 1
2181.96742	2181.87855	2182.09347	Si 1
2185.13655	2185.03735	2185.19229	Fe 1
2189.73719	2189.61560	2189.85551	Ti 1
2200.44971	2200.25155	2200.57143	Ti 1
2205.64304	2205.30463	2206.04934	Na 1
2206.53129	2206.41920	2206.61413	Sc 1
2208.36775	2208.08357	2208.66335	Na 1
2221.12177	2221.01364	2221.20357	Ti 1
2223.28539	2223.17282	2223.47270	Ti 1
2225.71046	2225.59189	2225.88678	Fe 1
2226.01753	2225.92677	2226.15168	Fe 1
2226.67067	2226.59651	2226.78644	Sc 1
2227.40298	2227.27125	2227.53116	Ti 1
2231.05801	2230.94485	2231.15477	Ti 1
2238.07688	2237.78725	2238.25207	Fe 1
2239.29051	2239.14173	2239.37664	Fe 1
2244.39032	2244.26478	2244.48969	Ti 1
2260.79268	2260.48360	2260.94342	Ca 1
2261.98403	2261.77311	2262.08799	Fe 1
2262.49608	2262.19295	2262.60779	Ca 1
2265.12395	2264.78196	2265.28677	Ca 1
2265.36574	2265.28677	2265.51668	Ca 1
2280.77227	2280.44599	2281.04576	Mg 1
2292.92294	2292.73131	2292.98121	CO
2293.72358	2293.65096	2293.74592	CO
2293.78553	2293.74592	2293.86088	CO
2294.00361	2293.93585	2294.03581	CO
2294.07708	2294.03581	2294.16077	CO
2294.32630	2294.24573	2294.36569	CO
2294.40763	2294.36569	2294.56561	CO
2294.69263	2294.56561	2294.73055	CO
2294.77795	2294.73055	2294.96046	CO

Peak Wavelength (nm)	Base Wavelength (nm)	Top Wavelength (nm)	Element
2295.09829	2294.96046	2295.13539	CO
2295.18808	2295.13539	2295.26534	CO
2295.54663	2295.38030	2295.58522	CO
2295.63802	2295.58522	2295.72517	CO
2296.03669	2295.95008	2296.07504	CO
2296.12832	2296.07504	2296.22998	CO
2296.33434	2296.22998	2296.43490	Ti 1
2296.56963	2296.49987	2296.60983	CO
2296.65945	2296.60983	2296.73978	CO
2297.14449	2297.02467	2297.17961	CO
2297.23062	2297.17961	2297.31956	CO
2297.76104	2297.57946	2297.78938	CO
2297.84253	2297.78938	2297.94432	CO
2298.41853	2298.34917	2298.44413	CO
2298.49168	2298.44413	2298.56409	CO
2299.18012	2298.99392	2299.26382	CO
2299.90821	2299.77862	2300.06851	CO
2300.68001	2300.56832	2300.80323	CO
2301.49622	2301.37801	2301.58294	CO
2302.35057	2302.21270	2302.45760	CO
2303.24591	2303.11235	2303.35226	CO
2304.17618	2304.09698	2304.32189	CO
2305.14547	2304.98664	2305.20656	CO
2305.24416	2305.20656	2305.31651	CO
2306.15770	2306.06123	2306.23117	CO
2306.29139	2306.23117	2306.36611	CO
2307.21055	2307.09084	2307.29076	CO
2307.38938	2307.32075	2307.44070	CO
2308.30204	2308.16543	2308.40034	CO
2308.52453	2308.40034	2308.59526	CO
2309.43458	2309.31499	2309.55990	CO
2309.70917	2309.63487	2309.76482	CO
2310.60809	2310.52453	2310.75444	CO
2310.92948	2310.83941	2311.06932	CO
2311.82207	2311.69908	2311.90400	CO

Peak Wavelength (nm)	Base Wavelength (nm)	Top Wavelength (nm)	Element
2312.20870	2312.13392	2312.28386	CO
2313.07525	2312.92362	2313.20351	CO
2313.52850	2313.37844	2313.59836	CO
2314.37064	2314.26810	2314.51801	CO
2314.88795	2314.82289	2314.98783	CO
2315.70369	2315.62259	2315.83750	CO
2316.42643	2316.32732	2316.56723	Fe 1
2317.07900	2316.93709	2317.15700	CO
2317.75477	2317.71179	2317.86173	CO
2318.49632	2318.42152	2318.58646	CO
2319.25780	2319.19123	2319.38115	CO
2319.95265	2319.87597	2320.10088	CO
2320.80293	2320.72064	2320.86559	CO
2321.44820	2321.37040	2321.61530	CO
2322.04547	2321.82522	2322.15510	CO
2322.32840	2322.28005	2322.35002	CO
2322.38177	2322.35002	2322.44499	CO
2322.50652	2322.44499	2322.53995	CO
2322.57886	2322.53995	2322.65491	CO
2322.72835	2322.65491	2322.76986	CO
2322.81647	2322.76986	2322.90981	CO
2322.99010	2322.90981	2323.04476	CO
2323.09408	2323.04476	2323.19970	CO
2323.30219	2323.19970	2323.35464	CO
2323.41323	2323.35464	2323.55456	CO
2323.65416	2323.55456	2323.70951	CO
2323.77339	2323.70951	2323.89443	CO
2324.04750	2323.96441	2324.10935	CO
2324.17564	2324.10935	2324.34426	CO
2324.48318	2324.34426	2324.51920	CO
2324.96106	2324.87406	2325.02400	CO
2325.10355	2325.02400	2325.22393	CO
2325.48305	2325.40386	2325.54880	CO
2325.62918	2325.54880	2325.70375	CO
2325.73454	2325.70375	2325.81370	CO

Peak Wavelength (nm)	Base Wavelength (nm)	Top Wavelength (nm)	Element
2326.04925	2325.97864	2326.11359	CO
2326.19189	2326.11359	2326.30352	CO
2326.65795	2326.49844	2326.72336	CO
2326.80196	2326.72336	2326.89829	CO
2327.31006	2327.22816	2327.37311	CO
2327.45196	2327.37311	2327.72797	CO
2327.84832	2327.72797	2327.93290	CO
2328.00568	2327.93290	2328.06784	CO
2328.14117	2328.06784	2328.25777	CO
2328.74597	2328.66762	2328.80256	CO
2328.87147	2328.80256	2328.98250	CO
2329.54328	2329.42733	2329.59226	CO
2329.64353	2329.59226	2329.75220	CO
2330.35705	2330.25701	2330.39696	CO
2330.45725	2330.39696	2330.57189	CO
2331.30527	2331.15667	2331.44656	CO
2332.20530	2332.05133	2332.29623	CO
2334.11933	2334.04057	2334.26048	CO
2334.84511	2334.58036	2335.04019	Na 1
2335.14217	2335.04019	2335.27510	CO
2336.19973	2335.99982	2336.32970	CO
2336.77383	2336.67456	2336.84950	CO
2337.30003	2337.21436	2337.36430	CO
2337.39994	2337.36430	2337.46926	CO
2337.91351	2337.59921	2338.24397	Na 1
2338.44253	2338.32893	2338.52886	CO
2338.58875	2338.52886	2338.62882	CO
2338.68225	2338.62882	2338.76377	CO
2339.62543	2339.50349	2339.72840	CO
2339.82125	2339.72840	2339.90833	CO
2340.63389	2340.55808	2340.70303	CO
2340.85049	2340.74801	2340.94794	CO
2341.10318	2341.04790	2341.17785	CO
2342.11662	2341.96755	2342.22245	CO
2342.42837	2342.36240	2342.53233	CO

Peak Wavelength (nm)	Base Wavelength (nm)	Top Wavelength (nm)	Element
2342.63136	2342.53233	2342.71726	CO
2343.42575	2343.33703	2343.50696	CO
2343.80056	2343.70189	2343.87182	CO
2344.14630	2343.99677	2344.27667	Ti 1
2344.77416	2344.70650	2344.94641	CO
2345.22360	2345.16633	2345.30628	CO
2346.16481	2346.02100	2346.30090	CO
2346.68798	2346.55580	2346.74073	CO
2347.59715	2347.50544	2347.75034	CO
2348.20371	2348.11021	2348.26015	CO
2349.07149	2348.98487	2349.17480	CO
2349.76306	2349.67461	2349.89952	CO
2350.58699	2350.50929	2350.66423	CO
2351.37100	2351.30399	2351.56389	CO
2351.85281	2351.70384	2352.00872	CO
2352.04368	2352.00872	2352.07370	CO
2352.29125	2352.24363	2352.35359	CO
2352.41009	2352.35359	2352.45855	CO
2352.51512	2352.45855	2352.58850	CO
2352.65764	2352.58850	2352.71845	CO
2352.77904	2352.71845	2352.86340	CO
2352.95105	2352.86340	2353.00334	CO
2353.08714	2353.00334	2353.16328	CO
2353.28177	2353.16328	2353.35321	CO
2353.43771	2353.35321	2353.52314	CO
2353.66564	2353.52314	2353.69808	CO
2353.74465	2353.69808	2353.78804	CO
2353.82901	2353.78804	2353.92299	CO
2354.08590	2354.00796	2354.18289	CO
2354.26503	2354.18289	2354.36282	CO
2354.55554	2354.43780	2354.64772	CO
2354.74242	2354.64772	2354.86763	CO
2355.06565	2355.00258	2355.17751	CO
2355.26296	2355.17751	2355.32246	CO
2355.38251	2355.32246	2355.43741	CO

Peak Wavelength (nm)	Base Wavelength (nm)	Top Wavelength (nm)	Element
2355.47726	2355.43741	2355.53738	CO
2355.62233	2355.53738	2355.72231	CO
2355.82494	2355.72231	2355.94722	CO
2356.22032	2356.14215	2356.31708	CO
2356.42848	2356.31708	2356.54699	CO
2356.65629	2356.54699	2356.79190	Fe 1
2356.86518	2356.79190	2356.94684	CO
2357.07301	2356.94684	2357.16176	CO
2357.55221	2357.39167	2357.62658	CO
2357.76338	2357.62658	2357.85649	CO
2358.28940	2358.20636	2358.41128	CO
2358.49277	2358.41128	2358.61620	CO
2358.79649	2358.71117	2358.94608	CO
2359.06880	2358.94608	2359.18099	CO
2359.26483	2359.18099	2359.43589	CO
2359.89250	2359.77076	2359.97069	CO
2360.08562	2359.97069	2360.25558	CO
2360.56502	2360.40552	2360.68541	CO
2360.76392	2360.68541	2360.84036	CO
2360.93488	2360.84036	2361.01529	CO
2361.67750	2361.58507	2361.74501	CO
2361.83435	2361.74501	2361.94993	CO
2362.37482	2362.26481	2362.42975	CO
2362.47956	2362.42975	2362.56470	CO
2362.63275	2362.56470	2362.69965	CO
2362.77545	2362.69965	2362.86458	CO
2363.64153	2363.51933	2363.69427	CO
2363.75777	2363.69427	2363.88919	CO
2364.00517	2363.93917	2364.06413	CO
2364.22648	2364.15409	2364.34402	CO
2364.69654	2364.61892	2364.72887	CO
2364.78304	2364.72887	2364.84883	CO
2364.89846	2364.84883	2365.07374	CO
2365.84847	2365.71350	2365.94341	CO
2366.12345	2366.05337	2366.20831	CO

Peak Wavelength (nm)	Base Wavelength (nm)	Top Wavelength (nm)	Element
2366.95761	2366.84807	2367.04799	CO
2367.36126	2367.27290	2367.45783	CO
2368.10612	2367.97264	2368.26753	CO
2369.30288	2369.17718	2369.42209	CO
2369.48358	2369.42209	2369.52705	Fe 1
2369.87163	2369.79194	2369.95188	CO
2370.04472	2369.95188	2370.11182	CO
2370.54059	2370.45669	2370.61163	CO
2370.65470	2370.61163	2370.72659	CO
2371.82244	2371.69622	2371.87115	CO
2371.90110	2371.87115	2371.96112	Ti 1
2371.98858	2371.96112	2372.02609	CO
2372.06554	2372.02609	2372.13105	CO
2372.42122	2372.25601	2372.52090	CO
2373.14204	2373.02571	2373.25562	CO
2373.37562	2373.25562	2373.49553	CO
2374.50640	2374.35521	2374.59012	CO
2374.80238	2374.74506	2374.90999	CO
2375.01794	2374.90999	2375.12491	CO
2375.91317	2375.80465	2376.00958	CO
2376.27975	2376.13953	2376.34445	CO
2377.36286	2377.27409	2377.47402	CO
2377.65535	2377.54899	2377.73892	CO
2377.80935	2377.73892	2377.87386	CO
2378.40862	2378.31870	2378.51362	CO
2378.85593	2378.76852	2378.93846	CO
2379.38261	2379.33331	2379.49825	CO
2380.59898	2380.52286	2380.67780	CO
2381.96888	2381.86234	2382.07726	CO
2382.32911	2382.20721	2382.48711	CO
2382.53031	2382.48711	2382.56708	CO
2382.59303	2382.56708	2382.64205	CO
2382.69178	2382.64205	2382.74201	CO
2382.79262	2382.74201	2382.85697	CO
2382.90094	2382.85697	2382.95693	CO

Peak Wavelength (nm)	Base Wavelength (nm)	Top Wavelength (nm)	Element
2383.01845	2382.95693	2383.03690	CO
2383.06473	2383.03690	2383.11187	CO
2383.15659	2383.11187	2383.22183	CO
2383.28969	2383.22183	2383.37177	CO
2383.45220	2383.37177	2383.51671	CO
2383.59633	2383.51671	2383.70164	CO
2383.79332	2383.70164	2383.86658	CO
2383.97175	2383.86658	2384.09150	CO
2384.17547	2384.09150	2384.25143	CO
2384.38436	2384.25143	2384.51633	CO
2384.60105	2384.51633	2384.74625	CO
2384.83894	2384.74625	2384.98116	CO
2385.08027	2384.98116	2385.18108	CO
2385.25285	2385.18108	2385.30103	CO
2385.33547	2385.30103	2385.44598	CO
2385.58450	2385.49596	2385.68089	CO
2386.14063	2386.05575	2386.25067	CO
2386.47027	2386.34064	2386.59054	CO
2386.73834	2386.65552	2386.88043	CO
2386.95885	2386.88043	2387.03537	CO
2387.10663	2387.03537	2387.26029	CO
2387.38572	2387.26029	2387.43022	CO
2387.44994	2387.43022	2387.53019	CO
2387.78723	2387.70512	2387.87006	CO
2388.06951	2387.92503	2388.15495	CO
2388.51876	2388.29989	2388.58478	CO
2388.79781	2388.74972	2388.93465	CO
2389.28684	2389.20955	2389.36948	CO
2389.57047	2389.47944	2389.71935	CO
2389.82698	2389.71935	2390.02923	CO
2390.11043	2390.02923	2390.20916	CO
2390.38601	2390.27914	2390.44407	CO
2390.50215	2390.44407	2390.60401	CO
2390.97399	2390.87891	2391.04385	CO
2391.24347	2391.13381	2391.34373	CO

Peak Wavelength (nm)	Base Wavelength (nm)	Top Wavelength (nm)	Element
2391.52671	2391.41371	2391.63362	CO
2391.89081	2391.82355	2391.97849	CO
2392.14582	2391.97849	2392.19841	CO
2392.24107	2392.19841	2392.28837	CO
2392.33820	2392.28837	2392.45831	CO
2392.84547	2392.76819	2392.92313	CO
2393.09164	2392.98311	2393.20302	CO
2393.85677	2393.78780	2393.98772	CO
2394.08084	2393.98772	2394.15266	CO
2394.21983	2394.15266	2394.35259	CO
2394.43785	2394.35259	2394.52752	CO
2394.70327	2394.62748	2394.82740	CO
2394.90640	2394.82740	2394.98235	CO
2395.11420	2394.98235	2395.25224	CO
2396.01036	2395.91699	2396.07193	CO
2397.20470	2397.04656	2397.25648	CO
2397.30563	2397.25648	2397.35144	CO
2397.39211	2397.35144	2397.54137	CO
2397.88938	2397.82126	2397.99120	CO
2398.11081	2397.99120	2398.23111	CO
2398.35507	2398.28109	2398.40104	CO
2398.46769	2398.40104	2398.63095	CO
2399.67175	2399.52561	2399.72054	CO
2399.75932	2399.72054	2399.84049	CO

Appendix C

Linelist used in the Analysis of Barnard's Star

Table C.2: Linelist of Spectral Lines used in Analysis of Barnard's Star

Peak Wavelength (nm)	Base Wavelength (nm)	Top Wavelength (nm)	Element
966.14186	966.10565	966.21522	Ti 1
967.55456	967.37941	967.71183	Ti 1
970.56645	970.46594	970.67314	Ti 1
971.89593	971.83621	971.96589	Ti 1
973.45706	973.42270	973.51362	Cr 1
974.69152	974.65083	974.72236	Ti 1
977.03046	976.90644	977.18020	Ti 1
978.76886	978.67094	978.90275	Ti 1
983.21403	983.16993	983.26504	Ti 1
1000.30907	1000.28200	1000.34540	Ti 1
1003.44360	1003.38650	1003.52708	Ti 1
1004.88313	1004.85353	1004.92727	Ti 1
1012.08937	1012.05211	1012.12300	Ti 1
1034.38076	1034.23124	1034.58663	Ca 1
1039.68049	1039.60965	1039.83161	Ti 1
1042.30482	1042.26240	1042.34932	Fe 1

Peak Wavelength (nm)	Base Wavelength (nm)	Top Wavelength (nm)	Element
1042.38677	1042.34932	1042.41539	Fe 1
1048.62466	1048.59160	1048.66505	Cr 1
1049.61153	1049.50140	1049.70446	Ti 1
1050.99912	1050.94471	1051.02884	Cr 1
1058.46349	1058.40992	1058.56527	Ti 1
1060.77274	1060.71430	1060.83106	Ti 1
1064.76361	1064.72352	1064.82652	Cr 1
1066.16266	1066.09885	1066.23755	Ti 1
1066.72253	1066.68933	1066.81031	Cr 1
1067.21210	1067.15554	1067.24097	Cr 1
1067.70434	1067.55786	1067.79647	Ti 1
1072.63832	1072.56921	1072.74453	Ti 1
1073.28646	1073.23487	1073.32795	Ti 1
1074.92482	1074.83629	1074.96537	Si 1
1077.48604	1077.36329	1077.58971	Ti 1
1090.57333	1090.49862	1090.59683	Cr 1
1115.69402	1115.65032	1115.72847	Cr 1
1125.31838	1125.19915	1125.40184	Al 1
1125.48736	1125.40184	1125.59331	Al 1
1129.88785	1129.82514	1129.94575	Fe 1
1131.07140	1131.04309	1131.14118	Cr 1
1133.92126	1133.84215	1133.95184	Cr 1
1142.23192	1142.16288	1142.33814	Fe 1
1143.91376	1143.82900	1143.98544	Fe 1
1147.30287	1147.25654	1147.35221	Cr 1
1148.46126	1148.38984	1148.53924	Cr 1
1159.35836	1159.26634	1159.45197	Fe 1
1160.75686	1160.62829	1160.84898	Fe 1
1161.05496	1160.99614	1161.11232	Cr 1
1163.82566	1163.74511	1163.95086	Fe 1
1169.01845	1168.84144	1169.15729	K 1
1176.96366	1176.85359	1177.05774	K 1
1177.28357	1177.16767	1177.47399	K 1
1178.32705	1178.22834	1178.39735	Fe 1
1179.71619	1179.65978	1179.78177	Ti 1

Peak Wavelength (nm)	Base Wavelength (nm)	Top Wavelength (nm)	Element
1182.81514	1182.66595	1182.97369	Mg 1
1188.28384	1188.18198	1188.35638	Fe 1
1188.40738	1188.35638	1188.57045	Fe 1
1194.95351	1194.89895	1194.99063	Ti 1
1195.59072	1195.54083	1195.65249	Ca 1
1243.22230	1243.10919	1243.35801	K 1
1252.20906	1251.97282	1252.35291	K 1
1260.02719	1259.94528	1260.07977	Ti 1
1267.10817	1266.98341	1267.20320	Ti 1
1267.91293	1267.80356	1268.14192	Na 1
1273.83784	1273.75916	1273.91213	Ti 1
1274.49372	1274.43490	1274.56244	Ti 1
1281.14819	1281.10520	1281.19067	Ti 1
1281.60036	1281.48986	1281.65658	Ca 1
1282.16686	1282.05423	1282.25524	Ti 1
1282.37650	1282.31940	1282.44773	Ca 1
1282.70215	1282.63168	1282.75576	Ca 1
1283.14310	1283.09383	1283.27360	Ti 1
1284.70310	1284.58840	1284.83695	Ti 1
1287.97611	1287.92640	1288.08967	Fe 1
1289.97616	1289.81376	1290.19672	Mn 1
1291.01114	1290.96730	1291.12664	Cr 1
1291.99001	1291.93225	1292.08740	Ti 1
1293.70312	1293.65717	1293.74779	Cr 1
1297.59422	1297.49906	1297.71547	Mn 1
1301.18836	1301.09193	1301.27856	Ti 1
1312.34072	1312.15792	1312.63509	Al 1
1315.07426	1314.79545	1315.28674	Al 1
1320.11388	1320.06882	1320.18772	Cr 1
1328.78310	1328.73195	1328.82946	Fe 1
1329.39381	1329.28165	1329.49894	Mn 1
1331.89674	1331.82032	1331.96693	Mn 1
1386.41711	1386.35005	1386.49804	Mn 1
1513.08841	1513.03605	1513.13194	OH
1514.57418	1514.51047	1514.65698	OH

Peak Wavelength (nm)	Base Wavelength (nm)	Top Wavelength (nm)	Element
1526.61687	1526.55630	1526.65814	OH
1527.84934	1527.80436	1527.93177	OH
1533.48415	1533.38979	1533.59440	Ti 1
1540.72407	1540.66495	1540.80372	OH
1540.91314	1540.80372	1541.00931	OH
1549.02815	1548.98184	1549.10068	Fe 1
1554.37472	1554.31284	1554.42691	Ti 1
1556.02427	1555.95205	1556.10776	OH
1556.87660	1556.83981	1556.94367	OH
1557.20731	1557.16181	1557.25011	OH
1562.67061	1562.56267	1562.70340	OH
1562.73660	1562.70340	1562.79723	OH
1565.19007	1565.12915	1565.22835	OH
1571.55699	1571.46421	1571.60575	Ti 1
1571.70524	1571.65293	1571.79973	OH
1571.96564	1571.84691	1572.01995	OH
1573.03993	1572.96410	1573.11626	OH
1575.54831	1575.48985	1575.60022	OH
1575.65198	1575.60022	1575.73687	OH
1577.67858	1577.57758	1577.72493	OH
1588.48745	1588.44451	1588.56108	OH
1588.78514	1588.70945	1588.84194	OH
1589.21281	1589.16526	1589.27659	OH
1589.76518	1589.67953	1589.87574	OH
1603.68352	1603.59044	1603.79371	OH
1605.27754	1605.19059	1605.37264	OH
1605.54458	1605.49046	1605.64577	OH
1606.17128	1606.12251	1606.24574	OH
1606.50107	1606.40648	1606.55652	OH
1606.95110	1606.89417	1607.03354	OH
1607.41495	1607.36056	1607.48388	OH
1619.01278	1618.89158	1619.06980	OH
1619.21048	1619.15081	1619.33985	OH
1624.78819	1624.69621	1624.89132	OH
1625.16406	1625.08103	1625.23282	OH

Peak Wavelength (nm)	Base Wavelength (nm)	Top Wavelength (nm)	Element
1626.01122	1625.95400	1626.11129	OH
1635.21712	1635.13486	1635.32576	OH
1635.45532	1635.39122	1635.52215	OH
1636.81114	1636.73918	1636.95212	OH
1644.37273	1644.30173	1644.47177	OH
1644.80278	1644.67474	1644.86676	OH
1647.27392	1647.20026	1647.33763	OH
1652.34862	1652.24640	1652.43380	OH
1652.62230	1652.50545	1652.78108	OH
1653.45626	1653.36006	1653.53103	OH
1653.85650	1653.79580	1653.92820	OH
1658.12248	1658.04894	1658.18168	OH
1660.54532	1660.50084	1660.64485	OH
1660.74961	1660.64485	1660.83874	OH
1670.43379	1670.33914	1670.52859	OH
1671.43523	1671.35907	1671.49287	OH
1671.88436	1671.73264	1671.98917	Al 1
1672.83825	1672.78689	1672.89291	OH
1672.97366	1672.89291	1673.06032	OH
1675.04768	1674.96443	1675.13205	Al 1
1676.31835	1676.23318	1676.37856	Al 1
1688.45017	1688.31461	1688.50046	OH
1688.62572	1688.57368	1688.68070	OH
1689.51623	1689.39059	1689.59910	OH
1689.88325	1689.78510	1689.96547	OH
1690.27128	1690.18534	1690.34320	OH
1690.42443	1690.34320	1690.48981	OH
1690.92652	1690.85637	1691.02558	OH
1705.22114	1705.15774	1705.40802	OH
1706.61205	1706.56890	1706.66567	OH
1706.94533	1706.88201	1706.97881	OH
1709.63605	1709.54868	1709.72546	OH
1710.03242	1709.99352	1710.10761	OH
1710.46685	1710.36432	1710.54689	OH
1710.86324	1710.76373	1710.94634	Mg 1

Peak Wavelength (nm)	Base Wavelength (nm)	Top Wavelength (nm)	Element
1711.01070	1710.94634	1711.12327	OH
1723.97845	1723.92189	1724.05415	OH
1730.84027	1730.80154	1730.87082	OH
1731.29062	1731.21727	1731.34432	OH
1741.09654	1740.99829	1741.13187	OH
1742.39400	1742.34031	1742.50305	OH
1761.06275	1761.03775	1761.09062	OH
1762.38309	1762.32467	1762.46576	OH
1781.45390	1781.41482	1781.50990	OH
1783.07165	1783.01993	1783.11509	OH
1803.36581	1803.33251	1803.41072	OH
1803.80824	1803.71753	1803.85592	OH
1804.36260	1804.28920	1804.42161	OH
2189.73450	2189.63303	2189.86676	Ti 1
2200.44546	2200.36666	2200.53548	Ti 1
2205.64175	2205.32650	2205.90035	Na 1
2208.36790	2208.14571	2208.66136	Na 1
2226.66432	2226.57724	2226.69608	Sc 1
2227.39937	2227.29778	2227.49096	Ti 1
2239.46916	2239.34369	2239.56779	Sc 1
2262.50632	2262.24994	2262.61218	Ca 1
2265.12235	2264.98326	2265.33082	Ca 1
2292.92057	2292.72054	2292.98058	CO
2292.92057	2292.72054	2292.98058	CO
2293.01571	2292.98058	2293.07236	CO
2293.14101	2293.07236	2293.22534	CO
2293.31865	2293.22534	2293.40129	CO
2293.53258	2293.40129	2293.66140	CO
2293.78108	2293.66140	2293.91389	CO
2294.00048	2293.91389	2294.02867	CO
2294.07429	2294.02867	2294.15876	CO
2294.32585	2294.24294	2294.35008	CO
2294.40589	2294.35008	2294.47253	CO
2294.68926	2294.64092	2294.72511	CO
2294.77611	2294.72511	2294.87055	CO

Peak Wavelength (nm)	Base Wavelength (nm)	Top Wavelength (nm)	Element
2295.09721	2295.03131	2295.13083	CO
2295.18807	2295.13083	2295.32989	CO
2295.54786	2295.47536	2295.57491	CO
2295.63942	2295.57491	2295.78166	CO
2296.04149	2295.91951	2296.07268	CO
2296.12679	2296.07268	2296.21820	CO
2296.56769	2296.46332	2296.60120	CO
2296.66173	2296.60120	2296.83869	CO
2297.22780	2297.08387	2297.29843	CO
2300.68763	2300.52680	2300.82609	CO
2307.20666	2307.10490	2307.29730	CO
2308.30031	2308.05166	2308.41354	CO
2309.43336	2309.29921	2309.57653	CO
2310.59813	2310.47807	2310.76324	CO
2311.81929	2311.69608	2311.93514	CO
2313.07339	2312.93789	2313.23880	CO
2314.36257	2314.25755	2314.58951	CO
2315.70018	2315.54707	2315.76335	CO
2317.07983	2317.02279	2317.23148	CO
2318.49624	2318.36025	2318.67734	CO
2319.95212	2319.87646	2320.04671	CO
2321.44655	2321.35494	2321.50981	CO
2322.57011	2322.44699	2322.65616	CO
2322.72664	2322.65616	2322.76463	CO
2322.81410	2322.76463	2322.88085	CO
2322.98728	2322.88085	2323.04357	CO
2323.09617	2323.04357	2323.22955	CO
2323.30371	2323.22955	2323.33805	CO
2323.40569	2323.33805	2323.56281	CO
2323.65076	2323.56281	2323.69457	CO
2323.76951	2323.69457	2323.88060	CO
2324.04722	2323.93486	2324.08990	CO
2324.16671	2324.08990	2324.22170	CO
2324.58376	2324.42328	2324.81098	CO
2324.95919	2324.81098	2325.02812	CO

Peak Wavelength (nm)	Base Wavelength (nm)	Top Wavelength (nm)	Element
2325.10162	2325.02812	2325.18324	CO
2325.47616	2325.43144	2325.54004	CO
2325.63198	2325.54004	2325.89690	CO
2326.05305	2325.95121	2326.11414	CO
2326.18905	2326.11414	2326.39349	CO
2326.65583	2326.57197	2326.71943	CO
2326.80133	2326.71943	2326.98332	CO
2327.29779	2327.13080	2327.37922	CO
2327.45066	2327.37922	2327.57331	CO
2327.84540	2327.73636	2327.93824	CO
2328.00598	2327.93824	2328.02366	CO
2328.13966	2328.02366	2328.24110	CO
2328.87315	2328.67605	2329.08000	CO
2329.54772	2329.42963	2329.59281	CO
2329.64022	2329.59281	2329.74046	CO
2330.45368	2330.19900	2330.52548	CO
2331.30612	2331.13969	2331.41186	CO
2332.20559	2332.07298	2332.36860	CO
2333.13376	2332.98329	2333.24790	CO
2334.12302	2334.04967	2334.28325	CO
2335.13782	2335.06980	2335.23337	CO
2336.19733	2336.14492	2336.29299	CO
2336.77141	2336.70605	2336.84636	CO
2337.29771	2337.18936	2337.40766	CO
2337.91202	2337.75074	2338.02368	Na 1
2338.43997	2338.36685	2338.53066	CO
2338.69106	2338.61647	2338.76468	CO
2339.62590	2339.51373	2339.69322	CO
2340.62979	2340.55967	2340.68459	CO
2340.84985	2340.76267	2340.94226	CO
2342.11603	2342.04352	2342.19977	CO
2342.62560	2342.55918	2342.71547	CO
2343.42525	2343.30944	2343.53613	CO
2343.81103	2343.70029	2343.98175	CO
2344.14608	2344.11467	2344.22414	Ti 1

Peak Wavelength (nm)	Base Wavelength (nm)	Top Wavelength (nm)	Element
2344.77894	2344.66207	2344.93582	CO
2346.16360	2346.08592	2346.21896	CO
2347.59683	2347.40100	2347.72206	CO
2349.06854	2348.93620	2349.14776	CO
2349.76900	2349.70418	2349.87662	CO
2350.58607	2350.44105	2350.71547	CO
2351.00802	2350.91935	2351.14677	CO
2351.37032	2351.14677	2351.49187	CO
2351.83673	2351.75073	2351.91547	CO
2352.05216	2352.00177	2352.07238	CO
2352.13305	2352.07238	2352.20576	CO
2352.40817	2352.37053	2352.45685	CO
2352.51371	2352.45685	2352.59810	CO
2352.77792	2352.74720	2352.87277	CO
2352.94964	2352.87277	2352.99835	CO
2353.08495	2352.99835	2353.13963	CO
2353.28575	2353.25737	2353.32017	CO
2353.43184	2353.39867	2353.50857	CO
2353.74504	2353.68129	2353.79121	CO
2353.82941	2353.79121	2353.90113	CO
2354.07805	2354.00321	2354.16811	CO
2354.26627	2354.16811	2354.33302	CO
2354.73596	2354.60790	2354.88281	CO
2355.05503	2355.02420	2355.12632	CO
2355.25820	2355.12632	2355.32273	CO
2355.38468	2355.32273	2355.43272	CO
2355.47247	2355.43272	2355.53487	CO
2355.61319	2355.53487	2355.66058	CO
2355.82300	2355.77845	2355.91204	CO
2356.24101	2356.16353	2356.35216	CO
2356.42594	2356.35216	2356.61155	CO
2356.85904	2356.82380	2356.91814	CO
2357.06907	2357.02035	2357.15401	CO
2357.55209	2357.49212	2357.57863	CO
2357.76655	2357.67300	2357.85389	CO

Peak Wavelength (nm)	Base Wavelength (nm)	Top Wavelength (nm)	Element
2358.28903	2358.23143	2358.32583	CO
2358.49317	2358.44383	2358.63264	CO
2358.78827	2358.73492	2358.86868	CO
2359.06326	2358.96310	2359.16770	CO
2359.26107	2359.16770	2359.38805	CO
2359.87945	2359.77372	2359.96264	CO
2360.08530	2359.96264	2360.15944	CO
2360.56213	2360.42713	2360.70272	CO
2360.74922	2360.70272	2360.82871	CO
2360.93385	2360.82871	2360.99409	CO
2361.66646	2361.61633	2361.69511	CO
2362.04332	2361.94721	2362.14418	CO
2362.37311	2362.27025	2362.39633	CO
2362.63280	2362.57758	2362.65639	CO
2362.76942	2362.65639	2362.88495	CO
2363.75562	2363.59441	2363.89403	CO
2364.02382	2363.89403	2364.06751	CO
2364.22495	2364.17791	2364.29620	CO
2364.78177	2364.71422	2364.84043	CO
2364.89274	2364.84043	2365.12442	CO
2365.84988	2365.74775	2365.99240	CO
2366.11013	2365.99240	2366.21338	CO
2366.97393	2366.86858	2367.05017	CO
2367.35507	2367.27916	2367.48447	CO
2368.11235	2367.95835	2368.25061	CO
2369.30050	2369.13554	2369.40424	CO
2369.86796	2369.79154	2369.92593	CO
2370.02621	2369.99708	2370.13938	CO
2370.54286	2370.44773	2370.69286	CO
2371.82368	2371.72900	2371.89515	CO
2372.06714	2372.01383	2372.12460	CO
2372.41878	2372.29868	2372.48860	CO
2373.14278	2373.05055	2373.24053	CO
2374.50782	2374.38075	2374.64213	CO
2375.02391	2374.91145	2375.12535	CO

Peak Wavelength (nm)	Base Wavelength (nm)	Top Wavelength (nm)	Element
2375.90587	2375.78302	2375.99700	CO
2377.36960	2377.28920	2377.51124	CO
2377.65518	2377.51124	2377.79676	CO
2378.40986	2378.32823	2378.45516	CO
2378.85358	2378.78047	2378.94710	CO
2379.38798	2379.35184	2379.45502	CO
2380.35940	2380.25679	2380.54263	CO
2380.59363	2380.54263	2380.66175	CO
2382.32325	2382.19486	2382.48889	CO
2382.52615	2382.48889	2382.56836	CO
2382.59830	2382.56836	2382.63989	CO
2382.69762	2382.63989	2382.75910	CO
2382.91127	2382.75910	2382.95781	CO
2383.07477	2382.95781	2383.22808	CO
2383.28243	2383.22808	2383.32348	CO
2383.44937	2383.41888	2383.51429	CO
2383.58684	2383.51429	2383.69716	CO
2383.78757	2383.69716	2383.86414	CO
2384.17203	2384.11065	2384.26175	CO
2384.37694	2384.26175	2384.44468	CO
2384.61693	2384.55604	2384.72308	CO
2385.09209	2384.97764	2385.14471	CO
2385.24994	2385.22427	2385.30383	CO
2385.34479	2385.30383	2385.48684	CO
2385.58651	2385.48684	2385.68577	CO
2385.84867	2385.68577	2385.92452	CO
2386.15361	2386.05982	2386.27472	CO
2386.74278	2386.64090	2386.80809	CO
2386.94464	2386.80809	2387.03898	CO
2387.10722	2387.03898	2387.29379	CO
2387.43813	2387.29379	2387.50084	CO
2388.07360	2387.88314	2388.13007	CO
2388.65813	2388.47263	2388.75149	CO
2388.79377	2388.75149	2388.83914	CO
2389.58033	2389.51654	2389.69987	CO

Peak Wavelength (nm)	Base Wavelength (nm)	Top Wavelength (nm)	Element
2389.81752	2389.69987	2389.90713	CO
2390.12230	2390.04266	2390.23400	CO
2390.38558	2390.28981	2390.43334	CO
2390.49547	2390.43334	2390.54497	CO
2390.97008	2390.88788	2391.01548	CO
2391.24377	2391.19095	2391.31060	CO
2391.52109	2391.40632	2391.59777	CO
2391.88423	2391.82115	2391.96476	CO
2392.13755	2392.06849	2392.19616	CO
2392.24113	2392.19616	2392.29191	CO
2392.35548	2392.29191	2392.49940	CO
2393.09054	2393.01819	2393.14591	CO
2394.09060	2393.99222	2394.15194	CO
2394.21753	2394.15194	2394.31965	CO
2394.43223	2394.36757	2394.51133	CO
2394.69965	2394.63115	2394.83084	CO
2394.89503	2394.83084	2394.95067	CO
2395.11023	2395.03855	2395.25426	CO
2396.01826	2395.90951	2396.09333	CO
2396.17830	2396.09333	2396.26917	CO
2397.20613	2397.12458	2397.25252	CO
2397.38166	2397.25252	2397.46044	CO
2398.10738	2398.01230	2398.17228	CO
2398.48265	2398.37228	2398.62029	CO
2399.65809	2399.54858	2399.70867	CO
2399.75986	2399.70867	2399.83674	CO

Bibliography

E. R. Adams, S. Seager, and L. Elkins-Tanton. Ocean Planet or Thick Atmosphere: On the Mass-Radius Relationship for Solid Exoplanets with Massive Atmospheres. *The Astrophysical Journal*, 673(2):1160–1164, Feb. 2008. doi: 10.1086/524925.

V. Adibekyan, N. C. Santos, C. Dorn, S. G. Sousa, A. A. Hakobyan, B. Bitsch, C. Mordasini, S. C. C. Barros, E. Delgado Mena, O. D. S. Demangeon, J. P. Faria, P. Figueira, B. M. T. B. Soares, and G. Israelian. Composition of super-Earths, super-Mercuries, and their host stars. *Communications of the Byurakan Astrophysical Observatory*, 68(2):447–453, Dec. 2021. doi: 10.52526/25792776-2021.68.2-447.

V. Adibekyan, M. Deal, C. Dorn, I. Dittrich, B. M. T. B. Soares, S. G. Sousa, N. C. Santos, B. Bitsch, C. Mordasini, S. C. C. Barros, D. Bossini, T. L. Campante, E. Delgado Mena, O. D. S. Demangeon, P. Figueira, N. Moedas, Z. Martirosyan, G. Israelian, and A. A. Hakobyan. Linking the primordial composition of planet building disks to the present-day composition of rocky exoplanets. *Astronomy & Astrophysics*, 692:A67, Dec. 2024. doi: 10.1051/0004-6361/202452193.

V. Z. Adibekyan, N. C. Santos, S. G. Sousa, G. Israelian, E. Delgado Mena, J. I.

González Hernández, M. Mayor, C. Lovis, and S. Udry. Overabundance of α-elements in exoplanet-hosting stars. *Astronomy & Astrophysics*, 543:A89, July 2012. doi: 10.1051/0004-6361/201219564.

Y. Alibert, C. Mordasini, and W. Benz. Extrasolar planet population synthesis. III. Formation of planets around stars of different masses. *Astronomy & Astrophysics*, 526:A63, Feb. 2011. doi: 10.1051/0004-6361/201014760.

F. Allard, P. H. Hauschildt, and D. Schwenke. TiO and H_2O Absorption Lines in Cool Stellar Atmospheres. *The Astrophysical Journal*, 540(2):1005–1015, Sept. 2000. doi: 10.1086/309366.

C. Allende Prieto. Velocities from Cross-Correlation: A Guide for Self-Improvement. *The Astronomical Journal*, 134(5):1843–1848, Nov. 2007. doi: 10.1086/522051.

C. Allende Prieto. Solar and stellar photospheric abundances. *Living Reviews in Solar Physics*, 13(1):1, Dec. 2016. doi: 10.1007/s41116-016-0001-6.

L. H. Aller and J. L. Greenstein. The Abundances of the Elements in G-Type Subdwarfs. *Astrophysical Journal, Supplement*, 5:139, Nov. 1960. doi: 10.1086/190054.

R. Alvarez and B. Plez. Near-infrared narrow-band photometry of M-giant and Mira stars: models meet observations. *Astronomy & Astrophysics*, 330:1109–1119, Feb. 1998. doi: 10.48550/arXiv.astro-ph/9710157.

A. M. Amarsi, S. Liljegren, and P. E. Nissen. 3D non-LTE iron abundances in FG-type dwarfs. *Astronomy & Astrophysics*, 668:A68, Dec. 2022. doi: 10.1051/0004-6361/202244542.

M. Asplund, N. Grevesse, A. J. Sauval, and P. Scott. The Chemical Composition of the Sun. *Annual Review of Astron and Astrophys*, 47(1):481–522, Sept. 2009. doi: 10.1146/annurev.astro.46.060407.145222.

I. Baraffe, G. Chabrier, F. Allard, and P. H. Hauschildt. Evolutionary models for solar metallicity low-mass stars: mass-magnitude relationships and color-magnitude diagrams. *Astronomy & Astrophysics*, 337:403–412, Sept. 1998. doi: 10.48550/arXiv.astro-ph/9805009.

J. L. Bean, C. Sneden, P. H. Hauschildt, C. M. Johns-Krull, and G. F. Benedict. Accurate M Dwarf Metallicities from Spectral Synthesis: A Critical Test of Model Atmospheres. *The Astrophysical Journal*, 652(2):1604–1616, Dec. 2006. doi: 10.1086/508321.

G. F. Benedict, T. J. Henry, O. G. Franz, B. E. McArthur, L. H. Wasserman, W.-C. Jao, P. A. Cargile, S. B. Dieterich, A. J. Bradley, E. P. Nelan, and A. L. Whipple. The Solar Neighborhood. XXXVII: The Mass-Luminosity Relation for Main-sequence M Dwarfs. *The Astronomical Journal*, 152(5):141, Nov. 2016. doi: 10.3847/0004-6256/152/5/141.

B. Benneke, P.-A. Roy, L.-P. Coulombe, M. Radica, C. Piaulet, E.-M. Ahrer, R. Pierrehumbert, J. Krissansen-Totton, H. E. Schlichting, R. Hu, J. Yang, D. Christie, D. Thorngren, E. D. Young, S. Pelletier, H. A. Knutson, Y. Miguel, T. M. Evans-Soma, C. Dorn, A. Gagnebin, J. J. Fortney, T. Komacek, R. MacDonald, E. Raul, R. Cloutier, L. Acuna, D. Lafrenière, C. Cadieux, R. Doyon, L. Welbanks, and

R. Allart. JWST Reveals CH_4, CO_2, and H_2O in a Metal-rich Miscible Atmosphere on a Two-Earth-Radius Exoplanet. *arXiv e-prints*, art. arXiv:2403.03325, Mar. 2024. doi: 10.48550/arXiv.2403.03325.

W. Benz, A. Anic, J. Horner, and J. A. Whitby. The Origin of Mercury. *Space Science Reviews*, 132(2-4):189–202, Oct. 2007. doi: 10.1007/s11214-007-9284-1.

B. Bitsch and C. Battistini. Influence of sub- and super-solar metallicities on the composition of solid planetary building blocks. *Astronomy & Astrophysics*, 633: A10, Jan. 2020. doi: 10.1051/0004-6361/201936463.

S. Blanco-Cuaresma. Modern stellar spectroscopy caveats. *Monthly Notices of the RAS*, 486(2):2075–2101, June 2019. doi: 10.1093/mnras/stz549.

S. Blanco-Cuaresma, C. Soubiran, U. Heiter, and P. Jofré. Determining stellar atmospheric parameters and chemical abundances of FGK stars with iSpec. *Astronomy & Astrophysics*, 569:A111, Sept. 2014. doi: 10.1051/0004-6361/201423945.

R. Blomme, S. Daflon, M. Gebran, A. Herrero, A. Lobel, L. Mahy, F. Martins, T. Morel, S. R. Berlanas, A. Blazère, Y. Frémat, E. Gosset, J. Maíz Apellániz, W. Santos, T. Semaan, S. Simón-Díaz, D. Volpi, G. Holgado, F. Jiménez-Esteban, M. F. Nieva, N. Przybilla, G. Gilmore, S. Randich, I. Negueruela, T. Prusti, A. Vallenari, E. J. Alfaro, T. Bensby, A. Bragaglia, E. Flaccomio, P. Francois, A. J. Korn, A. Lanzafame, E. Pancino, R. Smiljanic, M. Bergemann, G. Carraro, E. Franciosini, A. Gonneau, U. Heiter, A. Hourihane, P. Jofré, L. Magrini, L. Morbidelli, G. G. Sacco, C. C. Worley, and S. Zaggia. The Gaia-ESO Survey: The analysis of the hot-star spectra. *Astronomy & Astrophysics*, 661:A120, May 2022. doi: 10.1051/0004-6361/202142349.

J. J. Bochanski, J. A. Munn, S. L. Hawley, A. A. West, K. R. Covey, and D. P. Schneider. Exploring the Local Milky Way: M Dwarfs as Tracers of Galactic Populations. *The Astronomical Journal*, 134(6):2418–2429, Dec. 2007. doi: 10.1086/522053.

J. J. Bochanski, S. L. Hawley, K. R. Covey, A. A. West, I. N. Reid, D. A. Golimowski, and Ž. Ivezić. The Luminosity and Mass Functions of Low-mass Stars in the Galactic Disk. II. The Field. *The Astronomical Journal*, 139(6):2679–2699, June 2010. doi: 10.1088/0004-6256/139/6/2679.

J. C. Bond, D. S. Lauretta, and D. P. O'Brien. Making the Earth: Combining dynamics and chemistry in the Solar System. *Icarus*, 205(2):321–337, Feb. 2010. doi: 10.1016/j.icarus.2009.07.037.

X. Bonfils, X. Delfosse, S. Udry, N. C. Santos, T. Forveille, and D. Ségransan. Metallicity of M dwarfs. I. A photometric calibration and the impact on the mass-luminosity relation at the bottom of the main sequence. *Astronomy & Astrophysics*, 442(2):635–642, Nov. 2005. doi: 10.1051/0004-6361:20053046.

W. J. Borucki, D. Koch, G. Basri, N. Batalha, T. Brown, D. Caldwell, J. Caldwell, J. Christensen-Dalsgaard, W. D. Cochran, E. DeVore, E. W. Dunham, A. K. Dupree, T. N. Gautier, J. C. Geary, R. Gilliland, A. Gould, S. B. Howell, J. M. Jenkins, Y. Kondo, D. W. Latham, G. W. Marcy, S. Meibom, H. Kjeldsen, J. J. Lissauer, D. G. Monet, D. Morrison, D. Sasselov, J. Tarter, A. Boss, D. Brownlee, T. Owen, D. Buzasi, D. Charbonneau, L. Doyle, J. Fortney, E. B. Ford, M. J. Holman, S. Seager, J. H. Steffen, W. F. Welsh, J. Rowe, H. Anderson, L. Buchhave,

D. Ciardi, L. Walkowicz, W. Sherry, E. Horch, H. Isaacson, M. E. Everett, D. Fischer, G. Torres, J. A. Johnson, M. Endl, P. MacQueen, S. T. Bryson, J. Dotson, M. Haas, J. Kolodziejczak, J. Van Cleve, H. Chandrasekaran, J. D. Twicken, E. V. Quintana, B. D. Clarke, C. Allen, J. Li, H. Wu, P. Tenenbaum, E. Verner, F. Bruhweiler, J. Barnes, and A. Prsa. Kepler Planet-Detection Mission: Introduction and First Results. *Science*, 327(5968):977, Feb. 2010. doi: 10.1126/science.1185402.

C. L. Brinkman, A. S. Polanski, D. Huber, L. M. Weiss, D. Valencia, and M. Plotnykov. Revisiting the Relationship Between Rocky Exoplanet and Stellar Compositions: Reduced Evidence for a Super-Mercury Population. *arXiv e-prints*, art. arXiv:2409.08361, Sept. 2024a. doi: 10.48550/arXiv.2409.08361.

C. L. Brinkman, L. M. Weiss, D. Huber, R. A. Lee, J. Kolecki, G. Tenn, J. Zhang, S. Narayanan, A. S. Polanski, F. Dai, J. L. Bean, C. Beard, M. Brady, M. Brodheim, M. Brown, W. Deich, J. Edelstein, B. J. Fulton, S. Giacalone, S. R. Gibson, G. J. Gilbert, S. Halverson, L. Handley, G. M. Hill, R. Holcomb, B. Holden, A. Householder, A. W. Howard, H. Isaacson, S. Kaye, R. R. Laher, K. Lanclos, J. M. J. Ong, J. Payne, E. A. Petigura, D. Pidhorodetska, C. Poppett, A. Roy, R. Rubenzahl, N. Saunders, C. Schwab, A. Seifahrt, A. P. Shaum, M. M. Sirk, C. Smith, R. Smith, G. Stefánsson, J. Stürmer, J. Thorne, E. V. Turtelboom, D. Tyler, J. Valliant, J. Van Zandt, J. Walawender, S. W. Yee, S. Yeh, and J. Zink. The Compositions of Rocky Planets in Close-in Orbits Tend to be Earth-Like. *arXiv e-prints*, art. arXiv:2410.00213, Sept. 2024b. doi: 10.48550/arXiv.2410.00213.

M. K. Browning. Simulations of Dynamo Action in Fully Convective Stars. *The Astrophysical Journal*, 676(2):1262–1280, Apr. 2008. doi: 10.1086/527432.

B. Brugger, O. Mousis, M. Deleuil, and F. Deschamps. Constraints on Super-Earth Interiors from Stellar Abundances. *The Astrophysical Journal*, 850(1):93, Nov. 2017. doi: 10.3847/1538-4357/aa965a.

N. Brügger, Y. Alibert, S. Ataiee, and W. Benz. Metallicity effect and planet mass function in pebble-based planet formation models. *Astronomy & Astrophysics*, 619: A174, Nov. 2018. doi: 10.1051/0004-6361/201833347.

L. A. Buchhave, D. W. Latham, A. Johansen, M. Bizzarro, G. Torres, J. F. Rowe, N. M. Batalha, W. J. Borucki, E. Brugamyer, C. Caldwell, S. T. Bryson, D. R. Ciardi, W. D. Cochran, M. Endl, G. A. Esquerdo, E. B. Ford, J. C. Geary, R. L. Gilliland, T. Hansen, H. Isaacson, J. B. Laird, P. W. Lucas, G. W. Marcy, J. A. Morse, P. Robertson, A. Shporer, R. P. Stefanik, M. Still, and S. N. Quinn. An abundance of small exoplanets around stars with a wide range of metallicities. *Nature*, 486(7403):375–377, June 2012. doi: 10.1038/nature11121.

R. Burn, M. Schlecker, C. Mordasini, A. Emsenhuber, Y. Alibert, T. Henning, H. Klahr, and W. Benz. The New Generation Planetary Population Synthesis (NGPPS). IV. Planetary systems around low-mass stars. *Astronomy & Astrophysics*, 656:A72, Dec. 2021. doi: 10.1051/0004-6361/202140390.

R. P. Butler, S. S. Vogt, G. W. Marcy, D. A. Fischer, J. T. Wright, G. W. Henry, G. Laughlin, and J. J. Lissauer. A Neptune-Mass Planet Orbiting the Nearby M Dwarf GJ 436. *The Astrophysical Journal*, 617(1):580–588, Dec. 2004. doi: 10.1086/425173.

C. I. Cañas, S. Kanodia, C. F. Bender, S. Mahadevan, G. Stefánsson, W. D. Cochran, A. S. J. Lin, H.-C. Hwang, L. Powers, A. Monson, E. M. Green, B. A. Parker,

T. N. Swaby, H. A. Kobulnicky, J. Wisniewski, A. F. Gupta, M. E. Everett, S. Jones, B. Anjakos, C. Beard, C. H. Blake, S. A. Diddams, Z. Dong, C. Fredrick, E. Hakemiamjad, L. Hebb, J. E. Libby-Roberts, S. E. Logsdon, M. W. McElwain, A. J. Metcalf, J. P. Ninan, J. Rajagopal, L. W. Ramsey, P. Robertson, A. Roy, J. Ruhle, C. Schwab, R. C. Terrien, and J. T. Wright. TOI-3714 b and TOI-3629 b: Two Gas Giants Transiting M Dwarfs Confirmed with the Habitable-zone Planet Finder and NEID. *The Astronomical Journal*, 164(2):50, Aug. 2022. doi: 10.3847/1538-3881/ac7804.

C. Cadieux, R. Doyon, M. Plotnykov, G. Hébrard, F. Jahandar, É. Artigau, D. Valencia, N. J. Cook, E. Martioli, T. Vandal, J.-F. Donati, R. Cloutier, N. Narita, A. Fukui, T. Hirano, F. Bouchy, N. B. Cowan, E. J. Gonzales, D. R. Ciardi, K. G. Stassun, L. Arnold, B. Benneke, I. Boisse, X. Bonfils, A. Carmona, P. Cortés-Zuleta, X. Delfosse, T. Forveille, P. Fouqué, J. Gomes da Silva, J. M. Jenkins, F. Kiefer, Á. Kóspál, D. Lafrenière, J. H. C. Martins, C. Moutou, J. D. do Nascimento, M. Ould-Elhkim, S. Pelletier, J. D. Twicken, L. G. Bouma, S. Cartwright, A. Darveau-Bernier, K. Grankin, M. Ikoma, T. Kagetani, K. Kawauchi, T. Kodama, T. Kotani, D. W. Latham, K. Menou, G. Ricker, S. Seager, M. Tamura, R. Vanderspek, and N. Watanabe. TOI-1452 b: SPIRou and TESS Reveal a Super-Earth in a Temperate Orbit Transiting an M4 Dwarf. *The Astronomical Journal*, 164(3):96, Sept. 2022. doi: 10.3847/1538-3881/ac7cea.

Y. Chachan, H. A. Knutson, J. Lothringer, and G. A. Blake. Breaking Degeneracies in Formation Histories by Measuring Refractory Content in Gas Giants. *The Astrophysical Journal*, 943(2):112, Feb. 2023. doi: 10.3847/1538-4357/aca614.

D. Charbonneau and D. Deming. The Dynamics-Based Approach to Studying Terrestrial Exoplanets. *arXiv e-prints*, art. arXiv:0706.1047, June 2007. doi: 10.48550/arXiv.0706.1047.

A. C. Childs, R. G. Martin, and M. Livio. Life on Exoplanets in the Habitable Zone of M Dwarfs? *Astrophysical Journal, Letters*, 937(2):L41, Oct. 2022. doi: 10.3847/2041-8213/ac9052.

R. Cloutier. Exoplanet Demographics: Physical and Orbital Properties. *arXiv e-prints*, art. arXiv:2409.13062, Sept. 2024. doi: 10.48550/arXiv.2409.13062.

N. J. Cook, É. Artigau, R. Doyon, M. Hobson, E. Martioli, F. Bouchy, C. Moutou, A. Carmona, C. Usher, P. Fouqué, L. Arnold, X. Delfosse, I. Boisse, C. Cadieux, T. Vandal, J.-F. Donati, and A. Deslières. APERO: A PipelinE to Reduce Observations-Demonstration with SPIRou. *Publications of the ASP*, 134(1041): 114509, Nov. 2022. doi: 10.1088/1538-3873/ac9e74.

A. J. Cridland, R. E. Pudritz, T. Birnstiel, L. I. Cleeves, and E. A. Bergin. Composition of early planetary atmospheres - II. Coupled Dust and chemical evolution in protoplanetary discs. *Monthly Notices of the RAS*, 469(4):3910–3927, Aug. 2017. doi: 10.1093/mnras/stx1069.

E. Delgado Mena, G. Israelian, J. I. González Hernández, J. C. Bond, N. C. Santos, S. Udry, and M. Mayor. Chemical Clues on the Formation of Planetary Systems: C/O Versus Mg/Si for HARPS GTO Sample. *The Astrophysical Journal*, 725(2): 2349–2358, Dec. 2010. doi: 10.1088/0004-637X/725/2/2349.

J. F. Donati, D. Kouach, C. Moutou, R. Doyon, X. Delfosse, E. Artigau,

S. Baratchart, M. Lacombe, G. Barrick, G. Hébrard, F. Bouchy, L. Saddlemyer, L. Parès, P. Rabou, Y. Micheau, F. Dolon, V. Reshetov, Z. Challita, A. Carmona, N. Striebig, S. Thibault, E. Martioli, N. Cook, P. Fouqué, T. Vermeulen, S. Y. Wang, L. Arnold, F. Pepe, I. Boisse, P. Figueira, J. Bouvier, T. P. Ray, C. Feugeade, J. Morin, S. Alencar, M. Hobson, B. Castilho, S. Udry, N. C. Santos, O. Hernandez, T. Benedict, P. Vallée, G. Gallou, M. Dupieux, M. Larrieu, S. Perruchot, R. Sottile, F. Moreau, C. Usher, M. Baril, F. Wildi, B. Chazelas, L. Malo, X. Bonfils, D. Loop, D. Kerley, I. Wevers, J. Dunn, J. Pazder, S. Macdonald, B. Dubois, E. Carrié, H. Valentin, F. Henault, C. H. Yan, and T. Steinmetz. SPIRou: NIR velocimetry and spectropolarimetry at the CFHT. *Monthly Notices of the RAS*, 498(4):5684–5703, Nov. 2020. doi: 10.1093/mnras/staa2569.

C. Dorn, A. Khan, K. Heng, J. A. D. Connolly, Y. Alibert, W. Benz, and P. Tackley. Can we constrain the interior structure of rocky exoplanets from mass and radius measurements? *Astronomy & Astrophysics*, 577:A83, May 2015. doi: 10.1051/0004-6361/201424915.

C. Dorn, J. Venturini, A. Khan, K. Heng, Y. Alibert, R. Helled, A. Rivoldini, and W. Benz. A generalized Bayesian inference method for constraining the interiors of super Earths and sub-Neptunes. *Astronomy & Astrophysics*, 597:A37, Jan. 2017. doi: 10.1051/0004-6361/201628708.

C. Dorn, J. H. D. Harrison, A. Bonsor, and T. O. Hands. A new class of Super-Earths formed from high-temperature condensates: HD219134 b, 55 Cnc e, WASP-47 e. *Monthly Notices of the RAS*, 484(1):712–727, Mar. 2019. doi: 10.1093/mnras/sty3435.

C. D. Dressing and D. Charbonneau. The Occurrence Rate of Small Planets around Small Stars. *The Astrophysical Journal*, 767(1):95, Apr. 2013. doi: 10.1088/0004-637X/767/1/95.

C. D. Dressing and D. Charbonneau. The Occurrence of Potentially Habitable Planets Orbiting M Dwarfs Estimated from the Full Kepler Dataset and an Empirical Measurement of the Detection Sensitivity. *The Astrophysical Journal*, 807(1):45, July 2015. doi: 10.1088/0004-637X/807/1/45.

S. Elser, M. R. Meyer, and B. Moore. On the origin of elemental abundances in the terrestrial planets. *Icarus*, 221(2):859–874, Nov. 2012. doi: 10.1016/j.icarus.2012.09.016.

D. A. Fischer and J. Valenti. The Planet-Metallicity Correlation. *The Astrophysical Journal*, 622(2):1102–1117, Apr. 2005. doi: 10.1086/428383.

B. J. Foley and P. E. Driscoll. Whole planet coupling between climate, mantle, and core: Implications for rocky planet evolution. *Geochemistry, Geophysics, Geosystems*, 17(5):1885–1914, May 2016. doi: 10.1002/2015GC006210.

A. V. Freckelton, D. Sebastian, A. Mortier, A. H. M. J. Triaud, P. F. L. Maxted, L. Acuña, D. J. Armstrong, M. P. Battley, T. A. Baycroft, I. Boisse, V. Bourrier, A. Carmona, G. A. L. Coleman, A. C. Cameron, P. Cortés-Zuleta, X. Delfosse, G. Dransfield, A. Duck, T. Forveille, J. R. French, N. Hara, N. Heidari, C. Hellier, V. Kunovac, D. V. Martin, E. Martioli, J. J. McCormac, R. P. Nelson, L. Sairam, S. G. Sousa, M. R. Standing, and E. Willett. BEBOP V. Homogeneous stellar analysis of potential circumbinary planet hosts. *Monthly Notices of the RAS*, 531 (4):4085–4098, July 2024. doi: 10.1093/mnras/stae1405.

E. Gaidos, N. Haghighipour, E. Agol, D. Latham, S. Raymond, and J. Rayner. New Worlds on the Horizon: Earth-Sized Planets Close to Other Stars. *Science*, 318 (5848):210, Oct. 2007. doi: 10.1126/science.1144358.

E. Gaidos, A. W. Mann, A. L. Kraus, and M. Ireland. They are small worlds after all: revised properties of Kepler M dwarf stars and their planets. *Monthly Notices of the RAS*, 457(3):2877–2899, Apr. 2016. doi: 10.1093/mnras/stw097.

T. Gan, S. X. Wang, S. Wang, S. Mao, C. X. Huang, K. A. Collins, K. G. Stassun, A. Shporer, W. Zhu, G. R. Ricker, R. Vanderspek, D. W. Latham, S. Seager, J. N. Winn, J. M. Jenkins, K. Barkaoui, A. A. Belinski, D. R. Ciardi, P. Evans, E. Girardin, N. A. Maslennikova, T. Mazeh, A. Panahi, F. J. Pozuelos, D. J. Radford, R. P. Schwarz, J. D. Twicken, A. Wünsche, and S. Zucker. Occurrence Rate of Hot Jupiters Around Early-type M Dwarfs Based on Transiting Exoplanet Survey Satellite Data. *The Astronomical Journal*, 165(1):17, Jan. 2023. doi: 10.3847/1538-3881/ac9b12.

L. Ghezzi, K. Cunha, V. V. Smith, F. X. de Araújo, S. C. Schuler, and R. de la Reza. Stellar Parameters and Metallicities of Stars Hosting Jovian and Neptunian Mass Planets: A Possible Dependence of Planetary Mass on Metallicity. *The Astrophysical Journal*, 720(2):1290–1302, Sept. 2010. doi: 10.1088/0004-637X/720/2/1290.

M. Gillon, B. O. Demory, T. Barman, X. Bonfils, T. Mazeh, F. Pont, S. Udry, M. Mayor, and D. Queloz. Accurate Spitzer infrared radius measurement for the hot Neptune GJ 436b. *Astronomy & Astrophysics*, 471(3):L51–L54, Sept. 2007. doi: 10.1051/0004-6361:20078283.

M. Gillon, A. H. M. J. Triaud, B.-O. Demory, E. Jehin, E. Agol, K. M. Deck, S. M. Lederer, J. de Wit, A. Burdanov, J. G. Ingalls, E. Bolmont, J. Leconte, S. N. Raymond, F. Selsis, M. Turbet, K. Barkaoui, A. Burgasser, M. R. Burleigh, S. J. Carey, A. Chaushev, C. M. Copperwheat, L. Delrez, C. S. Fernandes, D. L. Holdsworth, E. J. Kotze, V. Van Grootel, Y. Almleaky, Z. Benkhaldoun, P. Magain, and D. Queloz. Seven temperate terrestrial planets around the nearby ultracool dwarf star TRAPPIST-1. *Nature*, 542(7642):456–460, Feb. 2017. doi: 10.1038/nature21360.

S. Ginzburg, H. E. Schlichting, and R. Sari. Core-powered mass-loss and the radius distribution of small exoplanets. *Monthly Notices of the RAS*, 476(1):759–765, May 2018. doi: 10.1093/mnras/sty290.

J. E. Gizis, I. N. Reid, and S. L. Hawley. The Palomar/MSU Nearby Star Spectroscopic Survey. III. Chromospheric Activity, M Dwarf Ages, and the Local Star Formation History. *The Astronomical Journal*, 123(6):3356–3369, June 2002. doi: 10.1086/340465.

G. Gonzalez. The stellar metallicity-giant planet connection. *Monthly Notices of the RAS*, 285(2):403–412, Feb. 1997. doi: 10.1093/mnras/285.2.403.

J. I. González Hernández, A. Suárez Mascareño, A. M. Silva, A. K. Stefanov, J. P. Faria, H. M. Tabernero, A. Sozzetti, R. Rebolo, F. Pepe, N. C. Santos, S. Cristiani, C. Lovis, X. Dumusque, P. Figueira, J. Lillo-Box, N. Nari, S. Benatti, M. J. Hobson, A. Castro-González, R. Allart, V. M. Passegger, M. R. Zapatero Osorio, V. Adibekyan, Y. Alibert, C. Allende Prieto, F. Bouchy, M. Damasso, V. D'Odorico, P. Di Marcantonio, D. Ehrenreich, G. Lo Curto, R. G. Santos,

C. J. A. P. Martins, A. Mehner, G. Micela, P. Molaro, N. Nunes, E. Palle, S. G. Sousa, and S. Udry. A sub-Earth-mass planet orbiting Barnard's star. *Astronomy & Astrophysics*, 690:A79, Oct. 2024. doi: 10.1051/0004-6361/202451311.

R. O. Gray and C. J. Corbally. An Expert Computer Program for Classifying Stars on the MK Spectral Classification System. *The Astronomical Journal*, 147(4):80, Apr. 2014. doi: 10.1088/0004-6256/147/4/80.

A. Gupta and H. E. Schlichting. Sculpting the valley in the radius distribution of small exoplanets as a by-product of planet formation: the core-powered mass-loss mechanism. *Monthly Notices of the RAS*, 487(1):24–33, July 2019. doi: 10.1093/mnras/stz1230.

A. Gupta and H. E. Schlichting. Caught in the act: core-powered mass-loss predictions for observing atmospheric escape. *Monthly Notices of the RAS*, 504(3):4634–4648, July 2021. doi: 10.1093/mnras/stab1128.

B. Gustafsson, B. Edvardsson, K. Eriksson, U. G. Jørgensen, Å. Nordlund, and B. Plez. A grid of MARCS model atmospheres for late-type stars. I. Methods and general properties. *Astronomy & Astrophysics*, 486(3):951–970, Aug. 2008. doi: 10.1051/0004-6361:200809724.

K. K. Hardegree-Ullman, M. C. Cushing, P. S. Muirhead, and J. L. Christiansen. Kepler Planet Occurrence Rates for Mid-type M Dwarfs as a Function of Spectral Type. *The Astronomical Journal*, 158(2):75, Aug. 2019. doi: 10.3847/1538-3881/ab21d2.

M. Haywood. Radial mixing and the transition between the thick and thin Galactic discs. *Monthly Notices of the RAS*, 388(3):1175–1184, Aug. 2008. doi: 10.1111/j.1365-2966.2008.13395.x.

N. Hejazi, I. J. M. Crossfield, T. Nordlander, M. Mansfield, D. Souto, E. Marfil, D. R. Coria, J. Brande, A. S. Polanski, J. E. Hand, and K. F. Wienke. Elemental Abundances of the Super-Neptune WASP-107b's Host Star Using High-resolution, Near-infrared Spectroscopy. *The Astrophysical Journal*, 949(2):79, June 2023. doi: 10.3847/1538-4357/accb97.

R. Helled, S. Werner, C. Dorn, T. Guillot, M. Ikoma, Y. Ito, M. Kama, T. Lichtenberg, Y. Miguel, O. Shorttle, P. J. Tackley, D. Valencia, and A. Vazan. Ariel planetary interiors White Paper. *Experimental Astronomy*, 53(2):323–356, Apr. 2022. doi: 10.1007/s10686-021-09739-3.

T. J. Henry, W.-C. Jao, J. P. Subasavage, T. D. Beaulieu, P. A. Ianna, E. Costa, and R. A. Méndez. The Solar Neighborhood. XVII. Parallax Results from the CTIOPI 0.9 m Program: 20 New Members of the RECONS 10 Parsec Sample. *The Astronomical Journal*, 132(6):2360–2371, Dec. 2006. doi: 10.1086/508233.

N. R. Hinkel, F. X. Timmes, P. A. Young, M. D. Pagano, and M. C. Turnbull. Stellar Abundances in the Solar Neighborhood: The Hypatia Catalog. *The Astronomical Journal*, 148(3):54, Sept. 2014. doi: 10.1088/0004-6256/148/3/54.

N. R. Hinkel, P. A. Young, M. D. Pagano, S. J. Desch, A. D. Anbar, V. Adibekyan, S. Blanco-Cuaresma, J. K. Carlberg, E. Delgado Mena, F. Liu, T. Nordlander, S. G. Sousa, A. Korn, P. Gruyters, U. Heiter, P. Jofré, N. C. Santos, and C. Soubiran. A Comparison of Stellar Elemental Abundance Techniques and

Measurements. *Astrophysical Journal, Supplement*, 226(1):4, Sept. 2016. doi: 10.3847/0067-0049/226/1/4.

N. R. Hinkel, P. A. Young, and I. Wheeler, Caleb H. A Concise Treatise on Converting Stellar Mass Fractions to Abundances to Molar Ratios. *The Astronomical Journal*, 164(6):256, Dec. 2022. doi: 10.3847/1538-3881/ac9bfa.

N. R. Hinkel, A. Youngblood, and M. Soares-Furtado. Host Stars and How Their Compositions Influence Exoplanets. *Reviews in Mineralogy and Geochemistry*, 90 (1):1–26, July 2024. doi: 10.2138/rmg.2024.90.01.

D. C. Hsu, E. B. Ford, and R. Terrien. Occurrence rates of planets orbiting M Stars: applying ABC to Kepler DR25, Gaia DR2, and 2MASS data. *Monthly Notices of the RAS*, 498(2):2249–2262, Oct. 2020. doi: 10.1093/mnras/staa2391.

I. Hubeny and T. Lanz. A brief introductory guide to TLUSTY and SYNSPEC. *arXiv e-prints*, art. arXiv:1706.01859, June 2017. doi: 10.48550/arXiv.1706.01859.

O. Hubickyj, P. Bodenheimer, and J. J. Lissauer. Core Accretion - Gas Capture Model for Gas Giant Planet Formation. In *AGU Fall Meeting Abstracts*, volume 2005, pages P42A–07, Dec. 2005.

T. O. Husser, S. Wende-von Berg, S. Dreizler, D. Homeier, A. Reiners, T. Barman, and P. H. Hauschildt. A new extensive library of PHOENIX stellar atmospheres and synthetic spectra. *Astronomy & Astrophysics*, 553:A6, May 2013. doi: 10. 1051/0004-6361/201219058.

S. Ida and D. N. C. Lin. Toward a Deterministic Model of Planetary Formation. II. The Formation and Retention of Gas Giant Planets around Stars with a Range of

Metallicities. *The Astrophysical Journal*, 616(1):567–572, Nov. 2004. doi: 10.1086/424830.

H. T. Ishikawa, W. Aoki, T. Hirano, T. Kotani, M. Kuzuhara, M. Omiya, Y. Hori, E. Kokubo, T. Kudo, T. Kurokawa, N. Kusakabe, N. Narita, J. Nishikawa, M. Ogihara, A. Ueda, T. Currie, T. Henning, Y. Kasagi, J. R. Kolecki, J. Kwon, M. N. Machida, M. W. McElwain, T. Nakagawa, S. Vievard, J. Wang, M. Tamura, and B. Sato. Elemental Abundances of nearby M Dwarfs Based on High-resolution Near-infrared Spectra Obtained by the Subaru/IRD Survey: Proof of Concept. *The Astronomical Journal*, 163(2):72, Feb. 2022. doi: 10.3847/1538-3881/ac3ee0.

A. R. Iyer, M. R. Line, P. S. Muirhead, J. J. Fortney, and E. Gharib-Nezhad. The SPHINX M-dwarf Spectral Grid. I. Benchmarking New Model Atmospheres to Derive Fundamental M-dwarf Properties. *The Astrophysical Journal*, 944(1):41, Feb. 2023. doi: 10.3847/1538-4357/acabc2.

F. Jahandar, R. Doyon, É. Artigau, N. J. Cook, C. Cadieux, D. Lafrenière, T. Forveille, J.-F. Donati, P. Fouqué, A. Carmona, R. Cloutier, P. Cristofari, E. Gaidos, J. Gomes da Silva, L. Malo, E. Martioli, J. D. do Nascimento, S. Pelletier, T. Vandal, and K. Venn. Comprehensive High-resolution Chemical Spectroscopy of Barnard's Star with SPIRou. *The Astrophysical Journal*, 966(1):56, May 2024. doi: 10.3847/1538-4357/ad3063.

P. Jofré, U. Heiter, C. Soubiran, S. Blanco-Cuaresma, C. C. Worley, E. Pancino, T. Cantat-Gaudin, L. Magrini, M. Bergemann, J. I. González Hernández, V. Hill,

C. Lardo, P. de Laverny, K. Lind, T. Masseron, D. Montes, A. Mucciarelli, T. Nordlander, A. Recio Blanco, J. Sobeck, R. Sordo, S. G. Sousa, H. Tabernero, A. Vallenari, and S. Van Eck. Gaia FGK benchmark stars: Metallicity. *Astronomy & Astrophysics*, 564:A133, Apr. 2014. doi: 10.1051/0004-6361/201322440.

P. Jofré, U. Heiter, C. C. Worley, S. Blanco-Cuaresma, C. Soubiran, T. Masseron, K. Hawkins, V. Adibekyan, S. Buder, L. Casamiquela, G. Gilmore, A. Hourihane, and H. Tabernero. Gaia FGK benchmark stars: opening the black box of stellar element abundance determination. *Astronomy & Astrophysics*, 601:A38, May 2017. doi: 10.1051/0004-6361/201629833.

J. A. Johnson, K. M. Aller, A. W. Howard, and J. R. Crepp. Giant Planet Occurrence in the Stellar Mass-Metallicity Plane. *Publications of the ASP*, 122(894):905, Aug. 2010. doi: 10.1086/655775.

S. Kanodia, S. Mahadevan, J. Libby-Roberts, G. Stefansson, C. I. Cañas, A. A. A. Piette, A. Boss, J. Teske, J. Chambers, G. Zeimann, A. Monson, P. Robertson, J. P. Ninan, A. S. J. Lin, C. F. Bender, W. D. Cochran, S. A. Diddams, A. F. Gupta, S. Halverson, S. Hawley, H. A. Kobulnicky, A. J. Metcalf, B. A. Parker, L. Powers, L. W. Ramsey, A. Roy, C. Schwab, T. N. Swaby, R. C. Terrien, and J. Wisniewski. TOI-5205b: A Short-period Jovian Planet Transiting a Mid-M Dwarf. *The Astronomical Journal*, 165(3):120, Mar. 2023. doi: 10.3847/1538-3881/acabce.

G. M. Kennedy and S. J. Kenyon. Planet Formation around Stars of Various Masses: The Snow Line and the Frequency of Giant Planets. *The Astrophysical Journal*, 673(1):502–512, Jan. 2008. doi: 10.1086/524130.

D. Khata, S. Mondal, R. Das, S. Ghosh, and S. Ghosh. Understanding the physical properties of young M dwarfs: NIR spectroscopic studies. *Monthly Notices of the RAS*, 493(3):4533–4550, Apr. 2020. doi: 10.1093/mnras/staa427.

R. K. Kopparapu, R. Ramirez, J. F. Kasting, V. Eymet, T. D. Robinson, S. Mahadevan, R. C. Terrien, S. Domagal-Goldman, V. Meadows, and R. Deshpande. Habitable Zones around Main-sequence Stars: New Estimates. *The Astrophysical Journal*, 765(2):131, Mar. 2013. doi: 10.1088/0004-637X/765/2/131.

D. Kossakowski, J. Kemmer, P. Bluhm, S. Stock, J. A. Caballero, V. J. S. Béjar, C. C. Guillén, N. Lodieu, K. A. Collins, M. Oshagh, M. Schlecker, N. Espinoza, E. Pallé, T. Henning, L. Kreidberg, M. Kürster, P. J. Amado, D. R. Anderson, J. C. Morales, S. Cartwright, D. Charbonneau, P. Chaturvedi, C. Cifuentes, D. M. Conti, M. Cortés-Contreras, S. Dreizler, D. Galadí-Enríquez, P. Guerra, R. Hart, C. Hellier, C. Henze, E. Herrero, S. V. Jeffers, J. M. Jenkins, E. L. N. Jensen, A. Kaminski, J. F. Kielkopf, M. Kunimoto, M. Lafarga, D. W. Latham, J. Lillo-Box, R. Luque, K. Molaverdikhani, D. Montes, G. Morello, E. H. Morgan, G. Nowak, A. Pavlov, M. Perger, E. V. Quintana, A. Quirrenbach, S. Reffert, A. Reiners, G. Ricker, I. Ribas, C. Rodríguez López, M. R. Zapatero Osorio, S. Seager, P. Schöfer, A. Schweitzer, T. Trifonov, S. Vanaverbeke, R. Vanderspek, R. West, J. Winn, and M. Zechmeister. TOI-1201 b: A mini-Neptune transiting a bright and moderately young M dwarf. *Astronomy & Astrophysics*, 656:A124, Dec. 2021. doi: 10.1051/0004-6361/202141587.

R. L. Kurucz. ATLAS12, SYNTHE, ATLAS9, WIDTH9, et cetera. *Memorie della Societa Astronomica Italiana Supplementi*, 8:14, Jan. 2005.

G. Laughlin, P. Bodenheimer, and F. C. Adams. The End of the Main Sequence. *The Astrophysical Journal*, 482(1):420–432, June 1997. doi: 10.1086/304125.

G. Laughlin, P. Bodenheimer, and F. C. Adams. The Core Accretion Model Predicts Few Jovian-Mass Planets Orbiting Red Dwarfs. *Astrophysical Journal, Letters*, 612 (1):L73–L76, Sept. 2004. doi: 10.1086/424384.

S. Lépine and E. Gaidos. An All-sky Catalog of Bright M Dwarfs. *The Astronomical Journal*, 142(4):138, Oct. 2011. doi: 10.1088/0004-6256/142/4/138.

S. Lépine, E. J. Hilton, A. W. Mann, M. Wilde, B. Rojas-Ayala, K. L. Cruz, and E. Gaidos. A Spectroscopic Catalog of the Brightest (J ¡ 9) M Dwarfs in the Northern Sky. *The Astronomical Journal*, 145(4):102, Apr. 2013. doi: 10.1088/0004-6256/145/4/102.

Z. Liu and D. Ni. Quantitative correlation of refractory elemental abundances between rocky exoplanets and their host stars. *Astronomy & Astrophysics*, 674:A137, June 2023. doi: 10.1051/0004-6361/202245387.

K. Lodders. Solar Elemental Abundances. *arXiv e-prints*, art. arXiv:1912.00844, Dec. 2019. doi: 10.48550/arXiv.1912.00844.

M. Lozovsky, R. Helled, I. Pascucci, C. Dorn, J. Venturini, and R. Feldmann. Why do more massive stars host larger planets? *Astronomy & Astrophysics*, 652:A110, Aug. 2021. doi: 10.1051/0004-6361/202140563.

H. Luo, C. Dorn, and J. Deng. The interior as the dominant water reservoir in super-Earths and sub-Neptunes. *Nature Astronomy*, 8:1399–1407, Nov. 2024. doi: 10.1038/s41550-024-02347-z.

N. Madhusudhan. Exoplanetary Atmospheres: Key Insights, Challenges, and Prospects. *Annual Review of Astron and Astrophys*, 57:617–663, Aug. 2019. doi: 10.1146/annurev-astro-081817-051846.

N. Madhusudhan, H. Knutson, J. J. Fortney, and T. Barman. Exoplanetary Atmospheres. In H. Beuther, R. S. Klessen, C. P. Dullemond, and T. Henning, editors, *Protostars and Planets VI*, pages 739–762, Jan. 2014. doi: 10.2458/azu_uapress_9780816531240-ch032.

N. Madhusudhan, M. Agúndez, J. I. Moses, and Y. Hu. Exoplanetary Atmospheres—Chemistry, Formation Conditions, and Habitability. *Space Science Reviews*, 205(1-4):285–348, Dec. 2016. doi: 10.1007/s11214-016-0254-3.

N. Madhusudhan, S. Sarkar, S. Constantinou, M. Holmberg, A. A. A. Piette, and J. I. Moses. Carbon-bearing Molecules in a Possible Hycean Atmosphere. *Astrophysical Journal, Letters*, 956(1):L13, Oct. 2023. doi: 10.3847/2041-8213/acf577.

J. Mah and B. Bitsch. Forming super-Mercuries: Role of stellar abundances. *Astronomy & Astrophysics*, 673:A17, May 2023. doi: 10.1051/0004-6361/202346021.

J. Maldonado, G. Micela, M. Baratella, V. D'Orazi, L. Affer, K. Biazzo, A. F. Lanza, A. Maggio, J. I. González Hernández, M. Perger, M. Pinamonti, G. Scandariato, A. Sozzetti, D. Locci, C. Di Maio, A. Bignamini, R. Claudi, E. Molinari, R. Rebolo, I. Ribas, B. Toledo-Padrón, E. Covino, S. Desidera, E. Herrero, J. C. Morales, A. Suárez-Mascareño, I. Pagano, A. Petralia, G. Piotto, and E. Poretti. HADES RV programme with HARPS-N at TNG. XII. The abundance signature of M dwarf stars with planets. *Astronomy & Astrophysics*, 644:A68, Dec. 2020. doi: 10.1051/0004-6361/202039478.

A. W. Mann, G. A. Feiden, E. Gaidos, T. Boyajian, and K. von Braun. How to Constrain Your M Dwarf: Measuring Effective Temperature, Bolometric Luminosity, Mass, and Radius. *The Astrophysical Journal*, 804(1):64, May 2015. doi: 10.1088/0004-637X/804/1/64.

R. A. Marcus, S. T. Stewart, D. Sasselov, and L. Hernquist. Collisional Stripping and Disruption of Super-Earths. *Astrophysical Journal, Letters*, 700(2):L118–L122, Aug. 2009. doi: 10.1088/0004-637X/700/2/L118.

E. Marfil, H. M. Tabernero, D. Montes, J. A. Caballero, F. J. Lázaro, J. I. González Hernández, E. Nagel, V. M. Passegger, A. Schweitzer, I. Ribas, A. Reiners, A. Quirrenbach, P. J. Amado, C. Cifuentes, M. Cortés-Contreras, S. Dreizler, C. Duque-Arribas, D. Galadí-Enríquez, T. Henning, S. V. Jeffers, A. Kaminski, M. Kürster, M. Lafarga, Á. López-Gallifa, J. C. Morales, Y. Shan, and M. Zechmeister. The CARMENES search for exoplanets around M dwarfs. Stellar atmospheric parameters of target stars with SteParSyn. *Astronomy & Astrophysics*, 656:A162, Dec. 2021. doi: 10.1051/0004-6361/202141980.

E. Martioli, G. Hébrard, P. Fouqué, É. Artigau, J. F. Donati, C. Cadieux, S. Bellotti, A. Lecavelier des Etangs, R. Doyon, J. D. do Nascimento, L. Arnold, A. Carmona, N. J. Cook, P. Cortes-Zuleta, L. de Almeida, X. Delfosse, C. P. Folsom, P. C. König, C. Moutou, M. Ould-Elhkim, P. Petit, K. G. Stassun, A. A. Vidotto, T. Vandal, B. Benneke, I. Boisse, X. Bonfils, P. Boyd, C. Brasseur, D. Charbonneau, R. Cloutier, K. Collins, P. Cristofari, I. Crossfield, R. F. Díaz, M. Fausnaugh, P. Figueira, T. Forveille, E. Furlan, E. Girardin, C. L. Gnilka, J. Gomes da Silva, P. G. Gu, P. Guerra, S. B. Howell, G. A. J. Hussain, J. M. Jenkins,

F. Kiefer, D. W. Latham, R. A. Matson, E. C. Matthews, J. Morin, R. Naves, G. Ricker, S. Seager, M. Takami, J. D. Twicken, A. Vanderburg, R. Vanderspek, and J. Winn. TOI-1759 b: A transiting sub-Neptune around a low mass star characterized with SPIRou and TESS. *Astronomy & Astrophysics*, 660:A86, Apr. 2022. doi: 10.1051/0004-6361/202142540.

M. Mayor, M. Marmier, C. Lovis, S. Udry, D. Ségransan, F. Pepe, W. Benz, J. L. Bertaux, F. Bouchy, X. Dumusque, G. Lo Curto, C. Mordasini, D. Queloz, and N. C. Santos. The HARPS search for southern extra-solar planets XXXIV. Occurrence, mass distribution and orbital properties of super-Earths and Neptune-mass planets. *arXiv e-prints*, art. arXiv:1109.2497, Sept. 2011. doi: 10.48550/arXiv.1109.2497.

E. Melo, D. Souto, K. Cunha, V. V. Smith, F. Wanderley, V. Grilo, D. Camara, K. Murta, N. Hejazi, I. J. M. Crossfield, J. Teske, R. Luque, M. Zhang, and J. Bean. Stellar Characterization and Chemical Abundances of Exoplanet-hosting M Dwarfs from APOGEE Spectra: Future JWST Targets. *The Astrophysical Journal*, 973 (2):90, Oct. 2024. doi: 10.3847/1538-4357/ad5004.

K. Ment and D. Charbonneau. The Occurrence Rate of Terrestrial Planets Orbiting Nearby Mid-to-late M Dwarfs from TESS Sectors 1-42. *The Astronomical Journal*, 165(6):265, June 2023. doi: 10.3847/1538-3881/acd175.

T. Mikal-Evans, N. Madhusudhan, J. Dittmann, M. N. Günther, L. Welbanks, V. Van Eylen, I. J. M. Crossfield, T. Daylan, and L. Kreidberg. Hubble Space Telescope Transmission Spectroscopy for the Temperate Sub-Neptune TOI-270 d: A Possible

Hydrogen-rich Atmosphere Containing Water Vapor. *The Astronomical Journal*, 165(3):84, Mar. 2023. doi: 10.3847/1538-3881/aca90b.

C. Mordasini. Planetary evolution with atmospheric photoevaporation. I. Analytical derivation and numerical study of the evaporation valley and transition from super-Earths to sub-Neptunes. *Astronomy & Astrophysics*, 638:A52, June 2020. doi: 10.1051/0004-6361/201935541.

C. Mordasini, Y. Alibert, W. Benz, H. Klahr, and T. Henning. Extrasolar planet population synthesis . IV. Correlations with disk metallicity, mass, and lifetime. *Astronomy & Astrophysics*, 541:A97, May 2012. doi: 10.1051/0004-6361/201117350.

G. D. Mulders. Planet Populations as a Function of Stellar Properties. In H. J. Deeg and J. A. Belmonte, editors, *Handbook of Exoplanets*, page 153. 2018. doi: 10.1007/978-3-319-55333-7_153.

G. D. Mulders, I. Pascucci, and D. Apai. An Increase in the Mass of Planetary Systems around Lower-mass Stars. *The Astrophysical Journal*, 814(2):130, Dec. 2015. doi: 10.1088/0004-637X/814/2/130.

D. J. Mullan and J. MacDonald. Are Magnetically Active Low-Mass M Dwarfs Completely Convective? *The Astrophysical Journal*, 559(1):353–371, Sept. 2001. doi: 10.1086/322336.

M. K. Ness, K. V. Johnston, K. Blancato, H. W. Rix, A. Beane, J. C. Bird, and K. Hawkins. In the Galactic Disk, Stellar [Fe/H] and Age Predict Orbits and Precise [X/Fe]. *The Astrophysical Journal*, 883(2):177, Oct. 2019. doi: 10.3847/1538-4357/ab3e3c.

E. R. Newton, D. Charbonneau, J. Irwin, and A. W. Mann. An Empirical Calibration to Estimate Cool Dwarf Fundamental Parameters from H-band Spectra. *The Astrophysical Journal*, 800(2):85, Feb. 2015. doi: 10.1088/0004-637X/800/2/85.

L. Noack and M. Lasbleis. Parameterisations of interior properties of rocky planets. An investigation of planets with Earth-like compositions but variable iron content. *Astronomy & Astrophysics*, 638:A129, June 2020. doi: 10.1051/0004-6361/202037723.

K. I. Öberg and E. A. Bergin. Excess C/O and C/H in Outer Protoplanetary Disk Gas. *Astrophysical Journal, Letters*, 831(2):L19, Nov. 2016. doi: 10.3847/2041-8205/831/2/L19.

K. I. Öberg, R. Murray-Clay, and E. A. Bergin. The Effects of Snowlines on C/O in Planetary Atmospheres. *Astrophysical Journal, Letters*, 743(1):L16, Dec. 2011. doi: 10.1088/2041-8205/743/1/L16.

K. Ohno and J. J. Fortney. Nitrogen as a Tracer of Giant Planet Formation. II. Comprehensive Study of Nitrogen Photochemistry and Implications for Observing NH_3 and HCN in Transmission and Emission Spectra. *The Astrophysical Journal*, 956(2):125, Oct. 2023a. doi: 10.3847/1538-4357/ace531.

K. Ohno and J. J. Fortney. Nitrogen as a Tracer of Giant Planet Formation. I. A Universal Deep Adiabatic Profile and Semianalytical Predictions of Disequilibrium Ammonia Abundances in Warm Exoplanetary Atmospheres. *The Astrophysical Journal*, 946(1):18, Mar. 2023b. doi: 10.3847/1538-4357/acafed.

T. Olander, U. Heiter, and O. Kochukhov. Comparative high-resolution spectroscopy of M dwarfs: Exploring non-LTE effects. *Astronomy & Astrophysics*, 649:A103, May 2021. doi: 10.1051/0004-6361/202039747.

J. E. Owen and Y. Wu. Kepler Planets: A Tale of Evaporation. *The Astrophysical Journal*, 775(2):105, Oct. 2013. doi: 10.1088/0004-637X/775/2/105.

J. E. Owen and Y. Wu. The Evaporation Valley in the Kepler Planets. *The Astrophysical Journal*, 847(1):29, Sept. 2017. doi: 10.3847/1538-4357/aa890a.

E. K. Pass, J. G. Winters, D. Charbonneau, J. M. Irwin, D. W. Latham, P. Berlind, M. L. Calkins, G. A. Esquerdo, and J. Mink. Mid-to-late M Dwarfs Lack Jupiter Analogs. *The Astronomical Journal*, 166(1):11, July 2023. doi: 10.3847/1538-3881/acd349.

V. M. Passegger, S. Wende-von Berg, and A. Reiners. Fundamental M-dwarf parameters from high-resolution spectra using PHOENIX ACES models. I. Parameter accuracy and benchmark stars. *Astronomy & Astrophysics*, 587:A19, Mar. 2016. doi: 10.1051/0004-6361/201322261.

V. M. Passegger, A. Bello-García, J. Ordieres-Meré, A. Antoniadis-Karnavas, E. Marfil, C. Duque-Arribas, P. J. Amado, E. Delgado-Mena, D. Montes, B. Rojas-Ayala, A. Schweitzer, H. M. Tabernero, V. J. S. Béjar, J. A. Caballero, A. P. Hatzes, T. Henning, S. Pedraz, A. Quirrenbach, A. Reiners, and I. Ribas. Metallicities in M dwarfs: Investigating different determination techniques. *Astronomy & Astrophysics*, 658:A194, Feb. 2022. doi: 10.1051/0004-6361/202141920.

V. M. Passegger, A. Suárez Mascareño, R. Allart, J. I. González Hernández, C. Lovis,

B. Lavie, A. M. Silva, H. M. Müller, H. M. Tabernero, S. Cristiani, F. Pepe, R. Rebolo, N. C. Santos, V. Adibekyan, Y. Alibert, C. Allende Prieto, S. C. C. Barros, F. Bouchy, A. Castro-González, V. D'Odorico, X. Dumusque, P. Di Marcantonio, D. Ehrenreich, P. Figueira, R. Génova Santos, G. Lo Curto, C. J. A. P. Martins, A. Mehner, G. Micela, P. Molaro, N. Nari, N. J. Nunes, E. Pallé, E. Poretti, J. Rodrigues, S. G. Sousa, A. Sozzetti, S. Udry, and M. R. Zapatero Osorio. The compact multi-planet system GJ 9827 revisited with ESPRESSO. *Astronomy & Astrophysics*, 684:A22, Apr. 2024. doi: 10.1051/0004-6361/202348592.

C. Piaulet-Ghorayeb, B. Benneke, M. Radica, E. Raul, L.-P. Coulombe, E.-M. Ahrer, D. Kubyshkina, W. S. Howard, J. Krissansen-Totton, R. J. MacDonald, P.-A. Roy, A. Louca, D. Christie, M. Fournier-Tondreau, R. Allart, Y. Miguel, H. E. Schlichting, L. Welbanks, C. Cadieux, C. Dorn, T. M. Evans-Soma, J. J. Fortney, R. Pierrehumbert, D. Lafrenière, L. Acuña, T. Komacek, H. Innes, T. G. Beatty, R. Cloutier, R. Doyon, A. Gagnebin, C. Gapp, and H. A. Knutson. JWST/NIRISS Reveals the Water-rich "Steam World" Atmosphere of GJ 9827 d. *Astrophysical Journal, Letters*, 974(1):L10, Oct. 2024. doi: 10.3847/2041-8213/ad6f00.

N. Piskunov and J. A. Valenti. Spectroscopy Made Easy: Evolution. *Astronomy & Astrophysics*, 597:A16, Jan. 2017. doi: 10.1051/0004-6361/201629124.

N. E. Piskunov, F. Kupka, T. A. Ryabchikova, W. W. Weiss, and C. S. Jeffery. VALD: The Vienna Atomic Line Data Base. *Astronomy and Astrophysics, Supplement*, 112:525, Sept. 1995.

B. Plez. Cool star model atmospheres for Gaia : ATLAS, MARCS, and PHOENIX. In

Journal of Physics Conference Series, volume 328 of *Journal of Physics Conference Series*, page 012005. IOP, Dec. 2011. doi: 10.1088/1742-6596/328/1/012005.

B. Plez. Turbospectrum: Code for spectral synthesis. Astrophysics Source Code Library, record ascl:1205.004, May 2012.

M. Plotnykov and D. Valencia. Chemical fingerprints of formation in rocky super-Earths' data. *Monthly Notices of the RAS*, 499(1):932–947, Nov. 2020. doi: 10.1093/mnras/staa2615.

J. B. Pollack, O. Hubickyj, P. Bodenheimer, J. J. Lissauer, M. Podolak, and Y. Greenzweig. Formation of the Giant Planets by Concurrent Accretion of Solids and Gas. *Icarus*, 124(1):62–85, Nov. 1996. doi: 10.1006/icar.1996.0190.

E. M. Price and L. A. Rogers. Tidally Distorted, Iron-enhanced Exoplanets Closely Orbiting Their Stars. *The Astrophysical Journal*, 894(1):8, May 2020. doi: 10.3847/1538-4357/ab7c67.

K. D. Putirka and J. C. Rarick. The composition and mineralogy of rocky exoplanets: A survey of ¿4000 stars from the Hypatia Catalog. *American Mineralogist*, 104(6):817–829, June 2019. doi: 10.2138/am-2019-6787.

I. N. Reid, S. L. Hawley, and J. E. Gizis. The Palomar/MSU Nearby-Star Spectroscopic Survey. I. The Northern M Dwarfs -Bandstrengths and Kinematics. *The Astronomical Journal*, 110:1838, Oct. 1995. doi: 10.1086/117655.

I. N. Reid, J. E. Gizis, J. G. Cohen, M. A. Pahre, D. W. Hogg, L. Cowie, E. Hu, and A. Songaila. Faint M-Dwarfs and the Structure of the Galactic Disk. *Publications of the ASP*, 109:559–565, May 1997. doi: 10.1086/133914.

A. Reiners. Observations of Cool-Star Magnetic Fields. *Living Reviews in Solar Physics*, 9(1):1, Dec. 2012. doi: 10.12942/lrsp-2012-1.

A. Reiners. Magnetic Fields in Low-Mass Stars: An Overview of Observational Biases. In P. Petit, M. Jardine, and H. C. Spruit, editors, *Magnetic Fields throughout Stellar Evolution*, volume 302 of *IAU Symposium*, pages 156–163, Aug. 2014. doi: 10.1017/S1743921314001963.

C. Reylé, K. Jardine, P. Fouqué, J. A. Caballero, R. L. Smart, and A. Sozzetti. The 10 parsec sample in the Gaia era. *Astronomy & Astrophysics*, 650:A201, June 2021. doi: 10.1051/0004-6361/202140985.

G. R. Ricker, J. N. Winn, R. Vanderspek, D. W. Latham, G. Á. Bakos, J. L. Bean, Z. K. Berta-Thompson, T. M. Brown, L. Buchhave, N. R. Butler, R. P. Butler, W. J. Chaplin, D. Charbonneau, J. Christensen-Dalsgaard, M. Clampin, D. Deming, J. Doty, N. De Lee, C. Dressing, E. W. Dunham, M. Endl, F. Fressin, J. Ge, T. Henning, M. J. Holman, A. W. Howard, S. Ida, J. M. Jenkins, G. Jernigan, J. A. Johnson, L. Kaltenegger, N. Kawai, H. Kjeldsen, G. Laughlin, A. M. Levine, D. Lin, J. J. Lissauer, P. MacQueen, G. Marcy, P. R. McCullough, T. D. Morton, N. Narita, M. Paegert, E. Palle, F. Pepe, J. Pepper, A. Quirrenbach, S. A. Rinehart, D. Sasselov, B. Sato, S. Seager, A. Sozzetti, K. G. Stassun, P. Sullivan, A. Szentgyorgyi, G. Torres, S. Udry, and J. Villasenor. Transiting Exoplanet Survey Satellite (TESS). *Journal of Astronomical Telescopes, Instruments, and Systems*, 1:014003, Jan. 2015. doi: 10.1117/1.JATIS.1.1.014003.

L. A. Rogers and S. Seager. A Framework for Quantifying the Degeneracies of Exoplanet Interior Compositions. *The Astrophysical Journal*, 712(2):974–991, Apr.

2010. doi: 10.1088/0004-637X/712/2/974.

B. Rojas-Ayala, K. R. Covey, P. S. Muirhead, and J. P. Lloyd. Metal-rich M-Dwarf Planet Hosts: Metallicities with K-band Spectra. *Astrophysical Journal, Letters*, 720(1):L113–L118, Sept. 2010. doi: 10.1088/2041-8205/720/1/L113.

B. Rojas-Ayala, K. R. Covey, P. S. Muirhead, and J. P. Lloyd. Metallicity and Temperature Indicators in M Dwarf K-band Spectra: Testing New and Updated Calibrations with Observations of 133 Solar Neighborhood M Dwarfs. *The Astrophysical Journal*, 748(2):93, Apr. 2012. doi: 10.1088/0004-637X/748/2/93.

Z. Rustamkulov, D. K. Sing, S. Mukherjee, E. M. May, J. Kirk, E. Schlawin, M. R. Line, C. Piaulet, A. L. Carter, N. E. Batalha, J. M. Goyal, M. López-Morales, J. D. Lothringer, R. J. MacDonald, S. E. Moran, K. B. Stevenson, H. R. Wakeford, N. Espinoza, J. L. Bean, N. M. Batalha, B. Benneke, Z. K. Berta-Thompson, I. J. M. Crossfield, P. Gao, L. Kreidberg, D. K. Powell, P. E. Cubillos, N. P. Gibson, J. Leconte, K. Molaverdikhani, N. K. Nikolov, V. Parmentier, P. Roy, J. Taylor, J. D. Turner, P. J. Wheatley, K. Aggarwal, E. Ahrer, M. K. Alam, L. Alderson, N. H. Allen, A. Banerjee, S. Barat, D. Barrado, J. K. Barstow, T. J. Bell, J. Blecic, J. Brande, S. Casewell, Q. Changeat, K. L. Chubb, N. Crouzet, T. Daylan, L. Decin, J. Désert, T. Mikal-Evans, A. D. Feinstein, L. Flagg, J. J. Fortney, J. Harrington, K. Heng, Y. Hong, R. Hu, N. Iro, T. Kataria, E. M.-R. Kempton, J. Krick, M. Lendl, J. Lillo-Box, A. Louca, J. Lustig-Yaeger, L. Mancini, M. Mansfield, N. J. Mayne, Y. Miguel, G. Morello, K. Ohno, E. Palle, D. J. M. Petit dit de la Roche, B. V. Rackham, M. Radica, L. Ramos-Rosado, S. Redfield, L. K. Rogers, E. L. Shkolnik, J. Southworth, J. Teske, P. Tremblin, G. S. Tucker,

O. Venot, W. C. Waalkes, L. Welbanks, X. Zhang, and S. Zieba. Early release science of the exoplanet wasp-39b with jwst nirspec prism. *Nature*, 614(7949): 659–663, Jan. 2023. ISSN 1476-4687. doi: 10.1038/s41586-022-05677-y. URL `http://dx.doi.org/10.1038/s41586-022-05677-y`.

A. Santerne, B. Brugger, D. J. Armstrong, V. Adibekyan, J. Lillo-Box, H. Gosselin, A. Aguichine, J. M. Almenara, D. Barrado, S. C. C. Barros, D. Bayliss, I. Boisse, A. S. Bonomo, F. Bouchy, D. J. A. Brown, M. Deleuil, E. Delgado Mena, O. Demangeon, R. F. Díaz, A. Doyle, X. Dumusque, F. Faedi, J. P. Faria, P. Figueira, E. Foxell, H. Giles, G. Hébrard, S. Hojjatpanah, M. Hobson, J. Jackman, G. King, J. Kirk, K. W. F. Lam, R. Ligi, C. Lovis, T. Louden, J. McCormac, O. Mousis, J. J. Neal, H. P. Osborn, F. Pepe, D. Pollacco, N. C. Santos, S. G. Sousa, S. Udry, and A. Vigan. An Earth-sized exoplanet with a Mercury-like composition. *Nature Astronomy*, 2:393–400, Mar. 2018. doi: 10.1038/s41550-018-0420-5.

N. C. Santos, M. Mayor, X. Bonfils, X. Dumusque, F. Bouchy, P. Figueira, C. Lovis, C. Melo, F. Pepe, D. Queloz, D. Ségransan, S. G. Sousa, and S. Udry. The HARPS search for southern extrasolar planets. XXV. Results from the metal-poor sample. *Astronomy & Astrophysics*, 526:A112, Feb. 2011. doi: 10.1051/0004-6361/201015494.

N. C. Santos, V. Adibekyan, C. Dorn, C. Mordasini, L. Noack, S. C. C. Barros, E. Delgado-Mena, O. Demangeon, J. P. Faria, G. Israelian, and S. G. Sousa. Constraining planet structure and composition from stellar chemistry: trends in different stellar populations. *Astronomy & Astrophysics*, 608:A94, Dec. 2017a. doi: 10.1051/0004-6361/201731359.

N. C. Santos, V. Adibekyan, C. Dorn, C. Mordasini, L. Noack, S. C. C. Barros, E. Delgado-Mena, O. Demangeon, J. P. Faria, G. Israelian, and S. G. Sousa. Constraining planet structure and composition from stellar chemistry: trends in different stellar populations. *Astronomy & Astrophysics*, 608:A94, Dec. 2017b. doi: 10.1051/0004-6361/201731359.

P. Santos-Peral, A. Recio-Blanco, P. de Laverny, E. Fernández-Alvar, and C. Ordenovic. The AMBRE Project: Spectrum normalisation influence on Mg abundances in the metal-rich Galactic disc. *Astronomy & Astrophysics*, 639:A140, July 2020. doi: 10.1051/0004-6361/202037522.

K. C. Schlaufman and G. Laughlin. A physically-motivated photometric calibration of M dwarf metallicity. *Astronomy & Astrophysics*, 519:A105, Sept. 2010. doi: 10.1051/0004-6361/201015016.

H. E. Schlichting and E. D. Young. Chemical Equilibrium between Cores, Mantles, and Atmospheres of Super-Earths and Sub-Neptunes and Implications for Their Compositions, Interiors, and Evolution. *The Planetary Science Journal*, 3(5):127, May 2022. doi: 10.3847/PSJ/ac68e6.

A. D. Schneider and B. Bitsch. How drifting and evaporating pebbles shape giant planets. I. Heavy element content and atmospheric C/O. *Astronomy & Astrophysics*, 654:A71, Oct. 2021. doi: 10.1051/0004-6361/202039640.

J. G. Schulze, J. Wang, J. A. Johnson, B. S. Gaudi, C. T. Unterborn, and W. R. Panero. On the Probability That a Rocky Planet's Composition Reflects Its Host Star. *The Planetary Science Journal*, 2(3):113, June 2021. doi: 10.3847/PSJ/abcaa8.

S. Seager, M. Kuchner, C. A. Hier-Majumder, and B. Militzer. Mass-Radius Relationships for Solid Exoplanets. *The Astrophysical Journal*, 669(2):1279–1297, Nov. 2007. doi: 10.1086/521346.

A. Sharma, E. Stonkutė, A. Drazdauskas, R. Minkevičiūtė, Š. Mikolaitis, G. Tautvaišienė, and T. Narbuntas. Chemical composition of planetary hosts: C, N, and α-element abundances. *arXiv e-prints*, art. arXiv:2410.07100, Oct. 2024. doi: 10.48550/arXiv.2410.07100.

A. L. Shields, S. Ballard, and J. A. Johnson. The habitability of planets orbiting M-dwarf stars. *Physics Reports*, 663:1, Dec. 2016. doi: 10.1016/j.physrep.2016.10.003.

C. I. Short and P. H. Hauschildt. Atmospheric Models of Red Giants with Massive-Scale Non-Local Thermodynamic Equilibrium. *The Astrophysical Journal*, 596(1): 501–508, Oct. 2003. doi: 10.1086/377602.

P. C. B. Smith, J. A. Sanchez, M. R. Line, E. Rauscher, M. Weiner Mansfield, E. M. R. Kempton, A. Savel, J. P. Wardenier, L. Pino, J. L. Bean, H. Beltz, V. Panwar, M. Brogi, I. Malsky, J. Fortney, J.-M. Desert, S. Pelletier, V. Parmentier, K. Kanumalla, L. Welbanks, M. Meyer, and J. Monnier. The Roasting Marshmallows Program with IGRINS on Gemini South II – WASP-121 b has super-stellar C/O and refractory-to-volatile ratios. *arXiv e-prints*, art. arXiv:2410.19017, Oct. 2024. doi: 10.48550/arXiv.2410.19017.

C. Sneden, J. Bean, I. Ivans, S. Lucatello, and J. Sobeck. MOOG: LTE line analysis and spectrum synthesis. Astrophysics Source Code Library, record ascl:1202.009, Feb. 2012.

C. Sotin, O. Grasset, and A. Mocquet. Mass radius curve for extrasolar Earth-like planets and ocean planets. *Icarus*, 191(1):337–351, Nov. 2007. doi: 10.1016/j.icarus.2007.04.006.

D. Souto, K. Cunha, D. A. García-Hernández, O. Zamora, C. Allende Prieto, V. V. Smith, S. Mahadevan, C. Blake, J. A. Johnson, H. Jönsson, M. Pinsonneault, J. Holtzman, S. R. Majewski, M. Shetrone, J. Teske, D. Nidever, R. Schiavon, J. Sobeck, A. E. García Pérez, Y. Gómez Maqueo Chew, and K. Stassun. Chemical Abundances of M-dwarfs from the APOGEE Survey. I. The Exoplanet Hosting Stars Kepler-138 and Kepler-186. *The Astrophysical Journal*, 835(2):239, Feb. 2017. doi: 10.3847/1538-4357/835/2/239.

D. Souto, K. Cunha, V. V. Smith, C. Allende Prieto, K. Covey, D. A. García-Hernández, J. A. Holtzman, H. Jönsson, S. Mahadevan, S. R. Majewski, T. Masseron, M. Pinsonneault, D. P. Schneider, M. Shetrone, K. G. Stassun, R. Terrien, O. Zamora, G. S. Stringfellow, R. R. Lane, C. Nitschelm, and B. Rojas-Ayala. Detailed Chemical Abundances for a Benchmark Sample of M Dwarfs from the APOGEE Survey. *The Astrophysical Journal*, 927(1):123, Mar. 2022. doi: 10.3847/1538-4357/ac4891.

A. Sozzetti, G. Torres, D. W. Latham, R. P. Stefanik, S. G. Korzennik, A. P. Boss, B. W. Carney, and J. B. Laird. A Keck HIRES Doppler Search for Planets Orbiting Metal-Poor Dwarfs. II. On the Frequency of Giant Planets in the Metal-Poor Regime. *The Astrophysical Journal*, 697(1):544–556, May 2009. doi: 10.1088/0004-637X/697/1/544.

J. C. Tarter, P. R. Backus, R. L. Mancinelli, J. M. Aurnou, D. E. Backman, G. S.

Basri, A. P. Boss, A. Clarke, D. Deming, L. R. Doyle, E. D. Feigelson, F. Freund, D. H. Grinspoon, R. M. Haberle, I. Hauck, Steven A., M. J. Heath, T. J. Henry, J. L. Hollingsworth, M. M. Joshi, S. Kilston, M. C. Liu, E. Meikle, I. N. Reid, L. J. Rothschild, J. Scalo, A. Segura, C. M. Tang, J. M. Tiedje, M. C. Turnbull, L. M. Walkowicz, A. L. Weber, and R. E. Young. A Reappraisal of The Habitability of Planets around M Dwarf Stars. *Astrobiology*, 7(1):30–65, Mar. 2007. doi: 10.1089/ast.2006.0124.

A. Thiabaud, U. Marboeuf, Y. Alibert, I. Leya, and K. Mezger. Elemental ratios in stars vs planets. *Astronomy & Astrophysics*, 580:A30, Aug. 2015. doi: 10.1051/0004-6361/201525963.

B. M. Tinsley. Stellar lifetimes and abundance ratios in chemical evolution. *The Astrophysical Journal*, 229:1046–1056, May 1979. doi: 10.1086/157039.

G. Torres, J. N. Winn, and M. J. Holman. Improved Parameters for Extrasolar Transiting Planets. *The Astrophysical Journal*, 677(2):1324–1342, Apr. 2008. doi: 10.1086/529429.

D. Turrini, E. Schisano, S. Fonte, S. Molinari, R. Politi, D. Fedele, O. Panić, M. Kama, Q. Changeat, and G. Tinetti. Tracing the Formation History of Giant Planets in Protoplanetary Disks with Carbon, Oxygen, Nitrogen, and Sulfur. *The Astrophysical Journal*, 909(1):40, Mar. 2021. doi: 10.3847/1538-4357/abd6e5.

Ł. Tychoniec, J. J. Tobin, A. Karska, C. Chandler, M. M. Dunham, R. J. Harris, K. M. Kratter, Z.-Y. Li, L. W. Looney, C. Melis, L. M. Pérez, S. I. Sadavoy, D. Segura-Cox, and E. F. van Dishoeck. The VLA Nascent Disk and Multiplicity Survey of Perseus Protostars (VANDAM). IV. Free-Free Emission from Protostars: Links to

Infrared Properties, Outflow Tracers, and Protostellar Disk Masses. *Astrophysical Journal, Supplement*, 238(2):19, Oct. 2018. doi: 10.3847/1538-4365/aaceae.

C. T. Unterborn, S. J. Desch, J. Haldemann, A. Lorenzo, J. G. Schulze, N. R. Hinkel, and W. R. Panero. The Nominal Ranges of Rocky Planet Masses, Radii, Surface Gravities, and Bulk Densities. *The Astrophysical Journal*, 944(1):42, Feb. 2023. doi: 10.3847/1538-4357/acaa3b.

J. A. Valenti and N. Piskunov. Spectroscopy made easy: A new tool for fitting observations with synthetic spectra. *Astronomy and Astrophysics, Supplement*, 118:595–603, Sept. 1996.

M. J. Veyette, P. S. Muirhead, A. W. Mann, J. M. Brewer, F. Allard, and D. Homeier. A Physically Motivated and Empirically Calibrated Method to Measure the Effective Temperature, Metallicity, and Ti Abundance of M Dwarfs. *The Astrophysical Journal*, 851(1):26, Dec. 2017. doi: 10.3847/1538-4357/aa96aa.

G. Wallerstein, J. L. Greenstein, R. Parker, H. L. Helfer, and L. H. Aller. Red Giants with Extreme Metal Deficiencies. *The Astrophysical Journal*, 137:280, Jan. 1963. doi: 10.1086/147501.

H. S. Wang, C. H. Lineweaver, and T. R. Ireland. The volatility trend of protosolar and terrestrial elemental abundances. *Icarus*, 328:287–305, Aug. 2019. doi: 10.1016/j.icarus.2019.03.018.

A. A. West, J. J. Bochanski, S. L. Hawley, K. L. Cruz, K. R. Covey, N. M. Silvestri, I. N. Reid, and J. Liebert. Using the Galactic Dynamics of M7 Dwarfs to Infer the Evolution of Their Magnetic Activity. *The Astronomical Journal*, 132(6):2507–2512, Dec. 2006. doi: 10.1086/508652.

O. I. Yakovlev, K. M. Ryazantsev, and S. I. Shornikov. Volatility inversion of silicon and magnesium oxides during the evaporation of HASP glasses on the moon. *Geochemistry International*, 56(1):71–74, Jan. 2018. doi: 10.1134/S001670291801010X.